Université de Montréal

Ultrasound shear wave imaging for diagnosis of nonalcoholic fatty liver disease

Par

Ladan Yazdani

Département de pharmacologie et physiologie/Institut de génie biomédical/Faculté de médecine

Thèse présentée en vue de l'obtention du grade de Philosophie Doctorat (Ph.D.) en génie biomédical

April 2023

Université de Montréal

Institut de Génie Biomédical, Département de Pharmacologie et Physiologie, Faculté de Médecine

---

Cette thèse intitulée

Ultrasound shear wave imaging for diagnosis of nonalcoholic fatty liver disease

Présenté par

Ladan Yazdani

A été évalué(e) par un jury composé des personnes suivantes

Jean Provost
Président-rapporteur

Guy Cloutier
Directeur de recherche

An Tang
Codirecteur

Nicolas Quaegebeur
Membre du jury

Caterina Gallippi
Examinateur externe

Catherine Martel
Représentant du doyen

Résumé

Pour le diagnostic et la stratification de la fibrose hépatique, la rigidité du foie est un biomarqueur quantitatif estimé par des méthodes d'élastographie. L'élastographie par ondes de cisaillement (« shear wave », SW) utilise des ultrasons médicaux non invasifs pour évaluer les propriétés mécaniques du foie sur la base des propriétés de propagation des ondes de cisaillement. La vitesse des ondes de cisaillement (« shear wave speed », SWS) et l'atténuation des ondes de cisaillement (« shear wave attenuation », SWA) peuvent fournir une estimation de la viscoélasticité des tissus. Les tissus biologiques sont intrinsèquement viscoélastiques et un modèle mathématique complexe est généralement nécessaire pour calculer la viscoélasticité en imagerie SW. Le calcul précis de l'atténuation est essentiel, en particulier pour une estimation précise du module de perte et de la viscosité. Des études récentes ont tenté d'augmenter la précision de l'estimation du SWA, mais elles présentent encore certaines limites.

Comme premier objectif de cette thèse, une méthode de décalage de fréquence revisitée a été développée pour améliorer les estimations fournies par la méthode originale de décalage en fréquence [Bernard et al 2017]. Dans la nouvelle méthode, l'hypothèse d'un paramètre de forme décrivant les caractéristiques spectrales des ondes de cisaillement, et assumé initialement constant pour tous les emplacements latéraux, a été abandonnée permettant un meilleur ajustement de la fonction gamma du spectre d'amplitude. En second lieu, un algorithme de consensus d'échantillons aléatoires adaptatifs (« adaptive random sample consensus », A-RANSAC) a été mis en œuvre pour estimer la pente du paramètre de taux variable de la distribution gamma afin d'améliorer la précision de la méthode. Pour valider ces changements algorithmiques, la méthode proposée a été comparée à trois méthodes récentes permettant d'estimer également l'atténuation des ondes de cisaillements (méthodes de décalage en fréquence, de décalage en fréquence en deux points et une méthode ayant comme acronyme anglophone AMUSE) à l'aide de données de simulations ou fantômes numériques. Également, des fantômes de gels homogènes *in vitro* et des données *in vivo* acquises sur le foie de canards ont été traités.

Comme deuxième objectif, cette thèse porte également sur le diagnostic précoce de la stéatose hépatique non alcoolique (NAFLD) qui est nécessaire pour prévenir sa progression et réduire la mortalité globale. À cet effet, la méthode de décalage en fréquence revisitée a été testée

sur des foies humains *in vivo*. La performance diagnostique de la nouvelle méthode a été étudiée sur des foies humains sains et atteints de la maladie du foie gras non alcoolique. Pour minimiser les sources de variabilité, une méthode d'analyse automatisée faisant la moyenne des mesures prises sous plusieurs angles a été mise au point. Les résultats de cette méthode ont été comparés à la fraction de graisse à densité de protons obtenue de l'imagerie par résonance magnétique (« magnetic resonance imaging proton density fat fraction », MRI-PDFF) et à la biopsie du foie. En outre, l'imagerie SWA a été utilisée pour classer la stéatose et des seuils de décision ont été établis pour la dichotomisation des différents grades de stéatose.

Finalement, le dernier objectif de la thèse consiste en une étude de reproductibilité de six paramètres basés sur la technologie SW (vitesse, atténuation, dispersion, module de Young, viscosité et module de cisaillement). Cette étude a été réalisée chez des volontaires sains et des patients atteints de NAFLD à partir de données acquises lors de deux visites distinctes. En conclusion, une méthode robuste de calcul du SWA du foie a été développée et validée pour fournir une méthode de diagnostic de la NAFLD.

Mots-clés : Échographie, élastographie par ondes de cisaillement, atténuation d'ondes de cisaillement, stéatose hépatique non alcoolique, stéatose hépatique, dispersion des vitesses de cisaillement, fraction graisseuse de la densité de protons en IRM, biopsie, reproductibilité, viscoélasticité.

Abstract

For diagnosis and staging of liver fibrosis, liver stiffness is a quantitative biomarker estimated by elastography methods. Ultrasound shear wave (SW) elastography utilizes noninvasive medical ultrasound to assess the mechanical properties of the liver based on the monitoring of the SW propagation. SW speed (SWS) and SW attenuation (SWA) can provide an estimation of tissue viscoelasticity. Biological tissues are inherently viscoelastic in nature and a complex mathematical model is usually required to compute viscoelasticity in SW imaging. Accurate computation of attenuation is critical, especially for accurate loss modulus and viscosity estimation. Recent studies have made attempts to increase the precision of SWA estimation, but they still face some limitations.

As a first objective of this thesis, a revisited frequency-shift method was developed to improve the estimates provided by the original implementation of the frequency-shift method [Bernard et al 2017]. In the new method, the assumption of a constant shape parameter of the gamma function describing the SW magnitude spectrum has been dropped for all lateral locations, allowing a better gamma fitting. Secondly, an adaptive random sample consensus algorithm (A-RANSAC) was implemented to estimate the slope of the varying rate parameter of the gamma distribution to improve the accuracy of the method. For the validation of these algorithmic changes, the proposed method was compared with three recent methods proposed to estimate SWA (frequency-shift, two-point frequency-shift and AMUSE methods) using simulation data or numerical phantoms. In addition, *in vitro* homogenous gel phantoms and *in vivo* animal (duck) liver data were processed.

As a second objective, this thesis also aimed at improving the early diagnosis of nonalcoholic fatty liver disease (NAFLD), which is necessary to prevent its progression and decrease the overall mortality. For this purpose, the revisited frequency-shift method was tested on *in vivo* human livers. The new method's diagnosis performance was investigated with healthy and NAFLD human livers. To minimize sources of variability, an automated analysis method averaging measurements from several angles has been developed. The results of this method were compared to the magnetic resonance imaging proton density fat fraction (MRI-PDFF) and to liver biopsy.

SWA imaging was used for grading steatosis and cut-off decision thresholds were established for dichotomization of different steatosis grades.

As a third objective, this thesis is proposing a reproducibility study of six SW-based parameters (speed, attenuation, dispersion, Young's modulus, viscosity and shear modulus). The assessment was performed in healthy volunteers and NAFLD patients using data acquired at two separate visits. In conclusion, a robust method for computing the liver's SWA was developed and validated to provide a diagnostic method for NAFLD.

Keywords: Ultrasound, shear wave elastography, shear wave attenuation, nonalcoholic fatty liver disease (NAFLD), liver steatosis, shear wave speed dispersion, MRI proton density fat fraction, biopsy, reproducibility, viscoelasticity.

Table of contents

List of tables

List of figures

List of symbols

E: Young's modulus

ρ: Density

c_s: Shear wave speed

σ: Stress

Γ: Elastic modulus

ε: Strain

G: Shear modulus

K: Bulk modulus

v: Poisson's ratio

G': Storage modulus

$G"$: Loss modulus

$u(r,t)$: Transverse displacement vector

r: Radial direction

ω: Angular frequency

$a(\omega)$: Amplitude term

H_0^1: Hankel function of the first kind of order zero

$\hat{k}$: Complex wavenumber

$U(r,\omega)$: Displacement amplitude

$\theta(U(r,\omega))$: Phase angle of the displacement amplitude

$U_0(r\ \omega)$: Initial displacement

α: Attenuation coefficient

$R(f)$: Amplitude spectrum

$G(f, x_1)$: Geometrical diffraction effects

$H(f, \Delta x)$: Viscous attenuation of the shear wave amplitude

$S(f)$: Shear wave amplitude spectrum

α_0: Linear attenuation

f: Frequency

A: Amplitude parameter of the gamma distribution

k: Shape parameter

β: Rate parameter

N: Number of all points

Th_{new}: Initial threshold

$u(x, t)$: Shear wave displacement field

$U(k, f)$: Fourier transform of the shear wave displacement field in the k-space domain

R^2: Coefficient of determination

∇^2: Laplacian operator in cylindrical coordinates

u_z: Displacement of the shear wave in the z-direction of cylindrical coordinates

F_z: Distribution of the applied body force in the z-direction

$g(t)$: Temporal application of the force

r: Cylindrical radius

A_0: Force intensity

σ^2: Half the variance of the pulse shape

$U_z(r,\omega)$: Temporal Fourier transforms of $u_z(r,t)$

$G(\omega)$: Temporal Fourier transforms of $g(t)$

$\hat{c}(\omega)$: Shear wave velocity in the viscoelastic medium

$\mu_s(\omega)$: Shear storage

$\mu_l(\omega)$: Loss moduli

$\widehat{U}_z(\varepsilon,\omega)$: Hankel transform of $U_z(\varepsilon,\omega)$

ε: Spatial frequency

$\hat{k}$: Complex wave number

J_o: Zero-order Bessel function

$H_0^{(2)}$: Hankel function of the second kind

α_1: The first order Taylor approximation of the attenuation

a: Beamwidth parameter

μ: The mean displacement value at a specific axial location

MSE: The mean square error

d_e: The estimated displacement value

d_g: The "predicted" ground truth value

$\Delta\varphi$: Phase difference

η: viscosity

List of abbreviations

AFLD: Alcoholic fatty liver disease

ALARA: As low as reasonably achievable

ALT: Alanine aminotransferase

AMUSE: Attenuation measuring ultrasound shear wave elastography

A-RANSAC: Adaptive random sample consensus

ARF: Acoustic radiation force

ARFI: Acoustic radiation force impulse

AST: Aspartate aminotransferase

AUC: Area under curve

B: Ballooning grade

BASH: Both alcoholic and nonalcoholic fatty liver diseases

BMI: Body mass index

CAP: Controlled attenuation parameter

CI: Confidence interval

CLD: Chronic liver disease

CRN: clinical research network

CT: Computed tomography

CV: Coefficient of variation

F: Fibrosis stage

FDA: Food and drug administration

FS: Frequency shift

FWHM: Full width at half maximum

HBV: Hepatitis b virus

HCC: Hepatocellular carcinoma

HCV: Hepatitis c virus

H/R: Hepatic/renal ratio

I: Lobular inflammation grade

ICC: Intraclass correlation coefficient

ISPPA: Intensity spatial peak pulse averaged

ISPTA: Intensity special peak temporal averaged

LOA: Limits of agreement

LSM: Liver stiffness measurement

MI: Mechanical index

MLR: Multiple linear regression

MRE: Magnetic resonance elastography

MRI: Magnetic resonance imaging

NASH: Nonalcoholic steatohepatitis

NAFLD: Nonalcoholic fatty liver disease

NFS: Nonalcoholic fatty liver disease fibrosis score

NPV: Negative predictive value

PDFF: Proton density fat fraction

PPV: Positive predictive value

PRF: Pulse repetition frequency

pSWE: Point shear wave elastography

QIBA: Quantitative imaging biomarker alliance

QUS: Quantitative ultrasound

RDC: Reproducibility coefficient

RF: Radiofrequency

R-FS: Revisited frequency shift

ROC: Receiver operating characteristic

ROI: Region of interest

S: Steatosis grade

SD: Standard deviation

SDUV: Shear wave dispersion ultrasound vibrometry

SNR: Signal-to-noise ratio

SSI: Supersonic shear wave imaging

SW: Shear wave

SWA: Shear wave attenuation

SWE: Shear wave elastography

SWD: Shear wave dispersion

SWS: Shear wave speed

TE: Transient elastography

THE: Time harmonic elastography

2P-FS: Two-point frequency shift

VTIQ: Virtual touch tissue imaging and quantification

VTQ: Virtual touch quantification

US: Ultrasound

Dedication

To my lovely mom and dad …

Acknowledgements

I would like to express my deepest gratitude to my advisors, Professor Guy Cloutier and Professor An Tang, for their valuable guidance, support, and encouragement throughout my doctoral studies. Their expertise and insights have been indispensable in shaping my research and intellectual development.

I would also like to thank the members of my dissertation committee, Professor Jean Provost, Professor Nicolas Quaegebeur, Professor Caterina Gallippi, and Professor Catherine Martel, for kindly accepting as my defense committee members.

In addition, special thanks to Dr. Louise Allard for her support and advice during my PhD. I am grateful to all my colleagues in LBUM lab for their support and camaraderie during my time at Université de Montréal. Also, thanks to all coauthors of my papers, for their collaborations and contributions. Their stimulating discussions, shared insights, and encouragement have been instrumental in my academic progress.

Finally, I would like to express my heartfelt appreciation to my family and friends for their unwavering love, support, and patience throughout this journey. Their encouragement and belief in me have sustained me through the challenges and struggles of graduate school.

I am honored and privileged to have had the opportunity to pursue my doctoral studies at Université de Montréal, and I am grateful for the support and guidance of all those who have contributed to my academic and personal growth.

Thank you to all of you.

Chapter 1 – Introduction

1.1 General introduction

The prevalence of nonalcoholic fatty liver disease (NAFLD) is on the rise and is becoming a widespread health concern. It is estimated that about 25% of the global population is affected by this common form of liver disease, which has become the most prevalent chronic liver condition, affecting 20% of people in Canada [1, 2]. NAFLD is strongly associated with obesity, and the prevalence of NAFLD increases with increasing body mass index (BMI) [3]. It is estimated that around 57% to 98% of people with obesity have NAFLD [4]. NAFLD is also commonly seen in people with type 2 diabetes, and the prevalence of NAFLD is estimated to be around 22% [5]. These figures highlight the growing burden of NAFLD and the need for improved screening, diagnosis, and treatment of this disease.

NAFLD is characterized by the accumulation of fat in the liver in individuals who drink little to no alcohol. The accumulation of fat can cause inflammation and injury to hepatocytes, leading to nonalcoholic steatohepatitis (NASH), which can progress to cirrhosis and liver failure [6]. Thus, the early diagnosis of NAFLD is necessary to prevent its progression and decrease the overall mortality. It is important to remember that NAFLD can be asymptomatic in its early stages and may not cause noticeable symptoms until it has progressed to a more advanced stage [7].

The diagnosis of NAFLD usually starts with a medical history and physical examination. The following tests may also be performed to confirm the diagnosis and assess the severity of the condition [8]:

Blood tests: Blood tests are used to verify the liver function and assess the extent of liver damage. Some of the blood tests used include liver function tests (alanine aminotransferase (AST) and aspartate aminotransferase (ALT)), bilirubin levels, alkaline phosphatase levels, and blood glucose levels.

Liver biopsy: In some cases, a liver biopsy may be necessary to confirm the diagnosis and determine the severity of NAFLD. A liver biopsy involves removing a small sample of the liver tissue for examination under a microscope.

Computed tomography (CT) scan and magnetic resonance imaging (MRI): These imaging tests can also be used to diagnose NAFLD and assess the severity of the disease.

Ultrasound: Ultrasound is a noninvasive exam that uses compression sound waves in the MHz range to produce images of the liver and other internal organs. This exam can show the presence of fat deposits in the liver.

Liver stiffness measurement (LSM): LSM is a noninvasive test that measures the stiffness of the liver using elastography methods, such as transient elastography or shear wave (SW) elastography (SWE), which is directly related to the stages of fibrosis. A stiff liver can indicate the presence of liver fibrosis or scarring, which is a common complication of NAFLD.

Nowadays, each of these diagnostic tools used to diagnose NAFLD has its own limitations, and some of these limitations are:

Blood tests: Blood tests can be limited by the fact that liver function tests (AST and ALT) can be elevated for many other reasons, such as hepatitis, alcohol abuse, and certain medications. In addition, these tests only provide an indirect measurement of the liver function, so a liver biopsy may still be necessary for a definitive diagnosis [8].

Liver biopsy: Liver biopsy is considered the historical reference (gold) standard for diagnosing NAFLD, but it is an invasive procedure and is not without risk, such as bleeding, pain, and infection. There is also a risk of sampling error, as the biopsy only provides information about a small area, so the results may not reflect the overall condition of the liver. It can also cause pain and discomfort, and patients may need to take pain medication to manage symptoms. In addition, it can be a more expensive diagnostic tool compared to other methods, such as ultrasound or MRI [9].

CT scan: A CT scan exam can be limited by the fact that it involves exposure to ionizing radiation, which can increase the risk of developing cancer over time, especially in patients who have multiple scans. It often requires the use of a contrast agent, which can cause an adverse reaction in some patients, such as an allergic reaction or kidney problems. It can be a more expensive diagnostic tool compared to other imaging methods, such as ultrasound. Also, it can take longer time to perform the exam compared to ultrasound, and may not be readily available in

all hospital locations. Other limitations include the difficulty in distinguishing between fat and fibrosis, which can be an important factor in determining the stage of NAFLD [8].

MRI: MRI can be a more expensive diagnostic tool compared to other imaging methods, such as ultrasound. MRI does not use ionizing radiation, making it a safer option for patients who may have had multiple X-rays or CT scans in the past. MRI is a more time-consuming procedure compared to ultrasound, and may not be available in all hospitals. Some patients, such as those with pacemakers or other metallic implanted medical devices, may not be suitable for MRI. Additionally, patients with a fear of enclosed spaces or claustrophobia may find the procedure uncomfortable. Similar to CT scans, although MRI can be effective in detecting the presence of fat in the liver, it can be more difficult to differentiate between fat and fibrosis [10-12].

Ultrasound: Ultrasound can be limited in its ability to differentiate between simple fatty liver and more advanced stages of NAFLD, such as non-alcoholic steatohepatitis (NASH). The accuracy of ultrasound can be dependent on the operator's skill and experience, which can lead to variability in results. Obesity can limit the accuracy of ultrasound, as excess fat in the abdomen attenuates the transmitted sound wave magnitude, and renders the liver more difficult to visualize [13].

In conclusion, no single test is perfect for diagnosing NAFLD, and a combination of tests is usually necessary to make an accurate diagnosis. The limitations of each test should be considered when making the medical decision, and the results of each test should be interpreted in the context of the patient's overall clinical picture. Thus, there is a need to develop a noninvasive, fast and low-cost imaging technique to better characterize NAFLD in its early stage [5].

1.2 Motivation

Ultrasound is often a preferred diagnostic tool for NAFLD due to its noninvasive nature, cost-effectiveness, wide availability, real-time imaging capability, ability to be easily repeated, and the possibility to evaluate the liver blood flow. Some of ultrasound-based techniques for diagnosis of NAFLD are described in summary in what follows.

- **Conventional ultrasound** (combining B-mode and Doppler flow imaging) is a commonly used diagnostic tool for NAFLD that provides real-time imaging of the liver.

This technique can be used to assess the liver size and shape, as well as to detect the presence of fat deposits. It can be challenging to distinguish between fat and other tissues with conventional ultrasound, as it is not highly specific for liver fat [14].

- **Doppler ultrasound** is a diagnostic tool used to evaluate blood flow in various organs, including the liver. In the liver, Doppler ultrasound can be used to assess the direction and velocity of the blood flow in the hepatic artery, portal vein, and hepatic veins. This technique can provide information about liver perfusion, the presence of liver tumors, portal hypertension, and liver fibrosis. Doppler ultrasound can also be used in combination with other imaging modalities, such as contrast-enhanced ultrasound or CT-scan, to improve the diagnostic accuracy. However, it should be noted that Doppler ultrasound may not be as specific for liver fat assessment as other ultrasound-based diagnostic methods [15].
- **Controlled Attenuation Parameter (CAP)** is an ultrasound technique that measures the amount of compression wave ultrasound energy absorbed by the liver tissue. This measurement can provide an estimation of the liver's fat content and is highly correlated with the amount of fat found in liver biopsy. However, this technique is highly influenced by the presence of fluid in the liver, and can provide false positive results in patients with fluid accumulation [16].
- **Acoustic Radiation Force Impulse (ARFI)** imaging is another ultrasound-based technique that measures the mechanical properties of the liver tissue. It uses compression waves to induce tissue displacements produced by propagating shear waves [17, 18]. This technique has been shown to be highly accurate for the diagnosis of liver fibrosis and may have potential for the diagnosis of NAFLD. However, the attenuation of compression waves with obesity can attenuate induced SWs and affect the accuracy of the method. In addition, this technique may not be as widely available as other ultrasound-based diagnostic methods [19].
- **Shear wave elastography (SWE)** is a technique similar to ARFI, which can measure the mechanical properties of the liver tissue. This technique can be used to differentiate between normal and fibrotic liver tissues, and has shown promise for the diagnosis of NAFLD and liver fibrosis. However, as in the case of ARFI, it may be affected by obesity due to compression wave attenuation, thus impacting the accuracy [20]. SWE

is also limited by its operator dependency and can be influenced by the quality of the ultrasound equipment used [21, 22].

ARFI and SWE have shown promising results for liver fibrosis assessments [17, 20, 23]. The main clinical application of liver ultrasound elastography is the diagnosis and staging of liver fibrosis in chronic liver disease cases. However, the World Federation for Ultrasound in Medicine and Biology (WFUMB) guidelines only confirmed the utility of ultrasound elastography in distinguishing fibrosis stages more than 2 from stages less than 2 [24]. Also, the Society of Radiologists in Ultrasound Consensus Conference Statement suggests using ultrasound elastography for distinguishing patients with liver fibrosis stages less than 2 from severe fibrosis or cirrhosis cases (stages above 2) [24]. Therefore, future works including increasing the accuracy in the differentiation of fibrosis stages and standardization of elastography methods are required in order to enabling comparisons between study results.

Ultrasound ARFI and SWE can also assess mechanical parameters of liver in order to achieve liver steatosis diagnosis and staging [21, 22, 25]. These methods use motion-tracking algorithms to assess the SW propagation for further analysis [17]. The SW speed in tissues can provide information on stiffness [26]. Mechanical parameters such as SW attenuation (which is different than compression wave attenuation) can provide viscoelasticity estimation of the liver for use in diagnosis [27]. The stiffness of an elastic medium is often computed using the Young's modulus (E) given as $E \approx 3\rho c^2$, where ρ is the density of the medium and c is the SW speed. However, biological tissues are inherently viscoelastic in nature and a complex mathematical model is required to compute viscoelasticity accurately [28]. State-of-the-art methods for viscoelasticity estimation require computation of SW attenuation, which has been a challenge mainly due to the variability of measurements, and the presence of noise on displacement images [28]. More details on ARFI, SWE, and other ultrasound based techniques are described in Chapter 2.

1.3 Thesis objectives

The general objective was to improve a SW attenuation imaging method and combine it to SWE for providing viscoelasticity biomarkers to assess liver steatosis. Three specific objectives are summarized next in line with the realization of this project.

Objective 1: An accurate computation of SW attenuation is critical for assessing the loss modulus and a viscosity estimation. The frequency-shift method proposed by our group [28] made a few assumptions about the SW frequency distribution that may not be valid in all conditions. With this method, the frequency spectrum is fitted to a gamma distribution from which descriptive parameters are used to determine the attenuation. More specifically, the shape parameter of the gamma distribution is assumed constant for all lateral locations from radiation pressure pushes, and as a consequence, the gamma fit may not match well the amplitude spectrum. Two important advancements were proposed in this thesis to improve the frequency-shift method for SW attenuation estimation. First, the assumption of a constant shape parameter for all lateral locations has been dropped, allowing a better gamma fitting [29]. Second, an adaptive version of the random sample consensus (A-RANSAC) algorithm [30] was implemented to estimate the slope of the varying rate parameter of the gamma distribution, improving the algorithm's accuracy. By using ground truth solutions of numerical phantoms developed in COMSOL, we could assess the revisited frequency shift method (R-FS) and compare SW attenuation results with other existing methods from the literature. The new implementation was compared with the original frequency shift (FS) method [28], the two- point frequency shift (2P-FS) [29], and the attenuation measuring ultrasound SW elastography (AMUSE) [31] methods using ten noisy numerical phantoms, two *in vitro* homogenous phantoms, and further validations were done using six *in vivo* healthy and fatty duck livers (including three healthy and three fatty livers).

Objective 2: Approximately 12%–40% of patients with NAFLD develop NASH, leading to a progression from fibrosis to cirrhosis and hepatocellular carcinoma, which has a high incidence of liver-related death. Thus, diagnosing NAFLD is necessary, and SWE is a potential technique for diagnosing NAFLD. We proposed here adding complementary SWE measures, such as SW attenuation and SW dispersion. Therefore, we performed a clinical study for steatosis diagnosis using the R-FS for SW attenuation, and a new implementation of SW dispersion based on a new linear model of the SW frequency dependency (based on A-RANSAC).

For this objective, gold standards for liver steatosis characterization were liver biopsy (or histopathological assessment including steatosis, lobular inflammation and ballooning grades, and fibrosis stage [32, 33]), and the MRI proton density fat fraction (MRI-PDFF – as a continuous variable (%) and an ordinal variable matching the corresponding steatosis grade: 0, 1, 2, 3) [10].

The proposed framework (the R-FS method) was utilized to identify liver steatosis using SW attenuation, and results were compared with SW dispersion [34].

The most challenging part of this objective was applying the previously developed tools to characterize *in vivo* human livers in both healthy and steatosis situations. All materials needed for SW radiation pressure generation, SW motion acquisition, and data processing were similar as in objective 1.

Objective 3: Previous state-of-the-art research has shown the clinical value of SWE to assess liver fibrosis staging [35, 36]. Other SWE measures might also be valuable to assess liver steatosis. Recently, six biomarkers based on SW viscoelasticity were investigated on *in vivo* fatty duck livers [37]. These six viscoelastic parameters are the SW speed, SW attenuation, SW dispersion, the Young's modulus, the shear modulus, and the viscosity.

In order to establish US-based SW viscoelastography as a reliable tool for NAFLD and NASH diagnosis, we evaluated the reproducibility of measured biomarkers, which refers to the ability to obtain consistent results despite changes in conditions [38]. The assessment of the reproducibility is crucial for determining whether changes observed between measurements are due to actual biological changes or variability in analysis. To reduce sources of variability, an automated analysis averaging measurements from multiple radiation pressure angles and using the R-FS method developed in objective 1 was performed.

Consequently, the third objective of this thesis was to evaluate the reproducibility of the six US-based SW viscoelastography parameters used in objective 2 for assessing mechanical properties of the liver in individuals with biopsy-proven NAFLD and healthy volunteers.

1.4 Thesis plan

This thesis investigates the potential of ultrasound SW attenuation imaging for diagnosing NAFLD, and assesses the accuracy and reliability of this technique in characterizing NAFLD, as well as its advantages and limitations compared to other diagnostic methods. Therefore, findings of this study will contribute to a better understanding of the role of ultrasound SW attenuation imaging in the diagnosis and management of this pathology, and may lead to improved diagnostic tools and patient outcomes.

There are seven chapters in this thesis. **Chapter 1** provides the general introduction, the motivation, and the objectives of this work. **Chapter 2** presents the pathophysiology of NAFLD, including its progression, and introduces diagnosis tools to detect it. **Chapter 3** summarizes basic principles of ultrasound SWE, and undertakes a literature review on ultrasound SW attenuation computation techniques. It also presents viscoelastic parameter reconstructions and applications to liver imaging. **Chapter 4** consists in the first article of this thesis on the development and validation of the revisited frequency shift (R-FS) method for SW attenuation computation. **Chapter 5** is the second article of this thesis, which is a clinical study that is based on the R-FS method for *in vivo* human liver diagnosis of NAFLD. **Chapter 6** is the third article of this thesis, which aims to fulfill our third objective on the reproducibility assessment of six viscoelastic parameters in healthy volunteers and biopsy proven NAFLD patients between two visits. Finally, **Chapter 7** discusses originalities and limitations of this thesis, concludes the three articles, and provides future perspectives.

Chapter 2 – Background

2.1 Nonalcoholic fatty liver disease (NAFLD)

The liver can become diseased when it absorbs excessive amounts of toxins, bacteria, and nutrients from the digestive tract due to its venous drainage [39]. It can also be targeted by viruses that affect the liver or experience genetic mutations, autoimmunity, or metabolic issues [40]. The liver faces internal challenges, such as metabolic disturbances and autophagy function, and external stimuli, such as viral infections and exposure to xenobiotics. These disturbances can cause stress to the subcellular organelles in the hepatocytes and lead to apoptosis [41]. Hepatocyte apoptosis and necrosis are often caused by mitochondrial dysfunction [40]. The liver injury occurs when hepatocyte death is triggered by extracellular and intracellular conditions, which are present in all acute and chronic liver conditions.

The most common chronic liver disease in both adults and children is NAFLD [1]. NAFLD encompasses different stages, including nonalcoholic fatty liver (NAFL), which involves fat accumulation in the liver, and NASH, which includes inflammation as well [42]. The prevalence of NAFLD has increased globally due to the rise in obesity and diabetes, affecting 25% of the world's population [1]. The prevalence of this disease and its progression are illustrated in **Figure 2.1**, based on [43-45]. A significant percentage of diabetic and obese individuals, 60% and 90%, respectively, have a form of NAFLD [46]. The Canadian population is affected by NAFLD at a rate of at least 20%, linked to sedentary lifestyles and diets high in calories [2]. Patients with NAFLD are at an increased risk of liver-related and cardiovascular mortality, and it is quickly becoming the leading cause of liver transplantation [47].

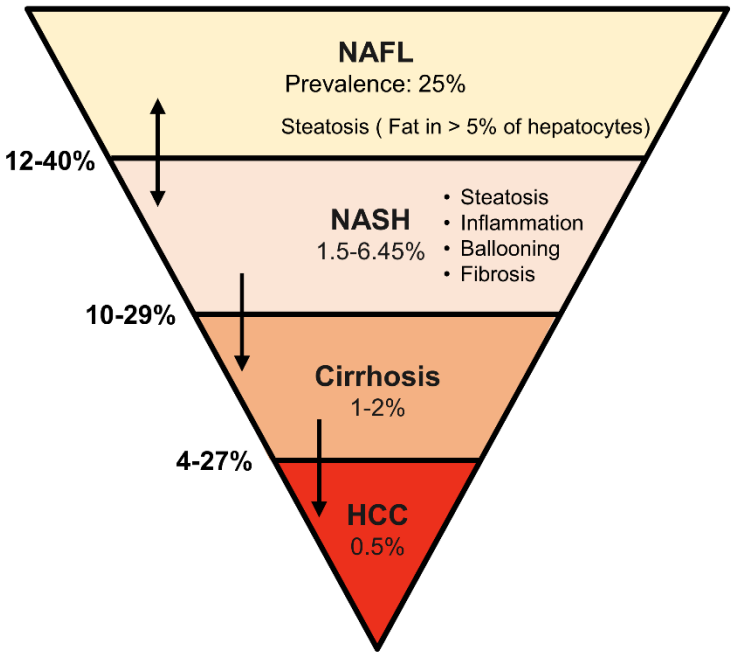

Figure 2.1 The prevalence of nonalcoholic fatty liver disease (NAFLD) and its progression [5, 48, 49]. HCC = hepatocellular carcinoma, NAFL = nonacoholic fatty liver, and NASH = nonalcoholic steatohepatitis.

Between 2004 and 2013, the number of NASH cases on the transplant list in the United States increased by 170% [50]. According to [51], it is anticipated that between 2019 and 2030, the number of NAFLD cases will increase by 20% and the number of deaths due to NAFLD will be doubled. Alcoholic liver disease (ALD) and both alcoholic and nonalcoholic steatohepatitis (BASH) are also becoming prevalent causes of chronic liver diseases, partly due to a rise in global alcohol consumption [1, 52]. It can be challenging to differentiate between NAFLD and ALD in a clinical setting because they share similar clinicopathological signs, such as inflammation, fibrosis, cirrhosis, and steatosis [42]. NAFLD, ALD, and BASH all have overlapping clinical and pathological features [42]. These diseases typically progress through several stages, including steatosis, steatohepatitis, fibrosis, cirrhosis, and hepatocellular carcinoma. Detailed descriptions of these stages of liver disease, which are relevant to both NAFLD and ALD, are presented in the following sections [53]. The progress of NAFLD to NASH and cirrhosis is shown in **Figure 2.2**. According to this figure, simple steatosis or NAFL has the potential to develop into NASH and

eventually cirrhosis, and it is believed that both NAFL and NASH can be reversed with proper treatment or diet.

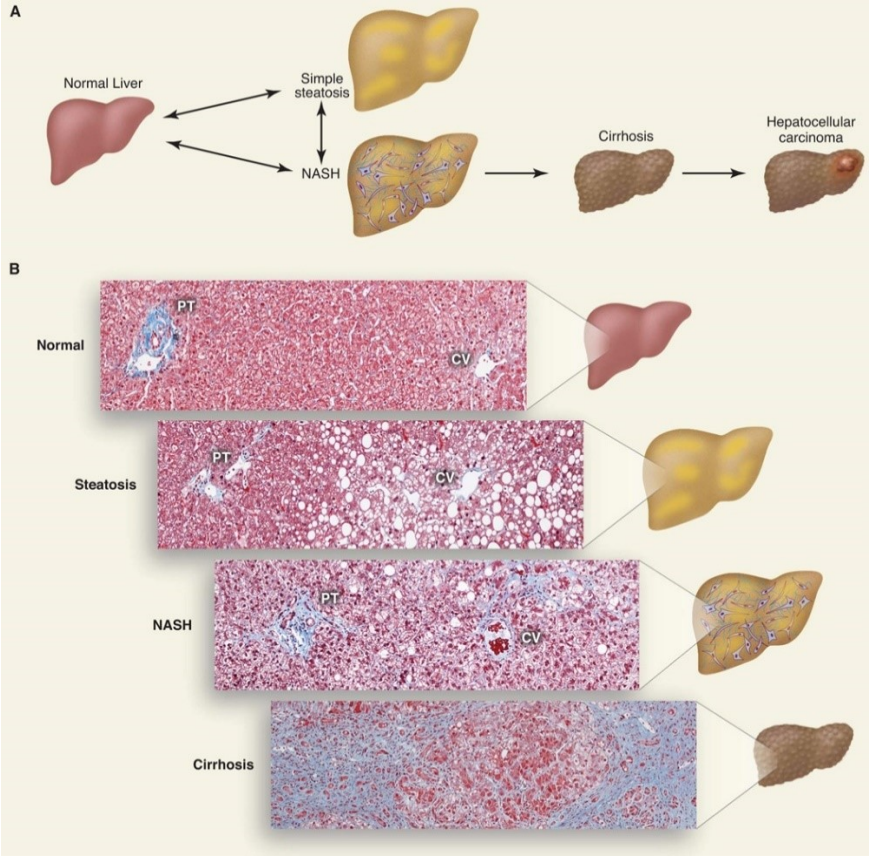

Figure 2.2 The progression of nonalcoholic fatty liver disease (NAFLD). Adopted from [45].

The first stage of NAFLD is steatosis, where the liver stores excess macrovesicular fat. This is characterized by the accumulation of triglycerides and free fatty acids in more than 5% of the hepatocytes. Simple steatosis is the most common type of NAFLD and does not show any clinical symptoms. Risk factors such as metabolic syndrome, older age, diabetes, and alcohol use increase the chances of developing steatosis [1]. Its global prevalence ranges from 23% to 32% in Europe, the Middle East, South America, Asia, and North America [54]. Steatosis can appear either as large lipid droplets that push the nucleus aside or small droplets that come in varying sizes [47]. The severity of steatosis is assessed using a three-tiered system based on the percentage of affected liver parenchyma: 5% - 33% is considered mild or S1, 34% - 66% is designated as moderate or S2, and >66% is classified as severe or S3 [47]. **Figure 2.3** illustrates these different histologic

manifestations of steatosis. While steatosis may not present any clinical symptom, it is metabolic stress that can lead to more severe liver diseases [55]. The accumulation of excess fat not only promotes inflammation but can also contribute to fibrosis, even with little to no apparent inflammation [56]. Research indicates that the buildup of fatty acids in liver cells can also trigger apoptotic cell death [46, 53].

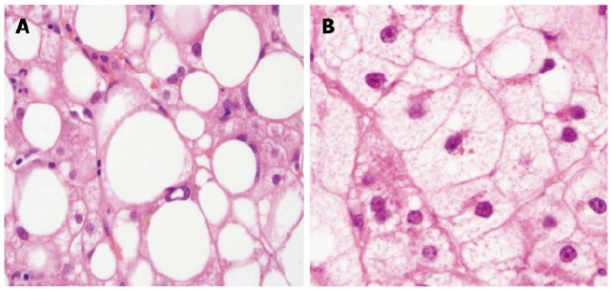

Figure 2.3 Histological features of simple steatosis; A: mixed large and small droplet steatosis B: micro vesicular steatosis. Adopted from [57].

2.1.1 Inflammation and ballooning

Liver inflammation is referred to as hepatitis in medical terms. It is often caused by viral infections such as hepatitis B (HBV) and hepatitis C (HCV), and excessive consumption of alcohol. In addition, some patients with simple steatosis or NAFL may develop inflammation in the liver, known as non-alcoholic steatohepatitis (NASH), the more severe form of NAFLD. NASH is caused by metabolic homeostasis disorder that leads to dysregulation of lipids, glucose, and bile acid metabolism [58]. About 35% of patients with steatosis progress to steatohepatitis, but the exact prevalence of NASH is unclear [59]. NASH and its alcoholic equivalent, ASH, are diagnosed based on steatosis combined with inflammation (lobular and portal), hepatocyte ballooning, and degeneration. The pathophysiological pathways from simple steatosis to NASH are not well understood [57, 60]. Ballooned hepatocytes are often observed in NASH and appear as enlarged hepatocytes with irregular cytoplasmic borders [53, 57].

NASH is usually linked to fibrosis, but ductular reactions can also be observed in the disease [47]. Cell death can occur as NASH develops, eventually resulting in advanced fibrosis [61]. Over an extended period, NASH can silently progress to liver cirrhosis, which can be life-

threatening and necessitate liver transplantation. Currently, there are no FDA-approved drugs for treating NASH, but various drug candidates are undergoing clinical trials, and they may be available soon [53, 58].

2.1.2 Fibrosis

Liver fibrosis is a well-known result of liver injury, and it is less common for patients with NAFL to have direct fibrosis progression than for patients with NASH [40, 60]. Fibrosis, which is the formation and accumulation of scar tissues, reduces liver elasticity, and causes stiffness [62]. Fibrosis can be caused by various factors such as alcohol, viral hepatitis, vascular pathologies, cryptogenic infection, and metabolic disorders [63]. Fibrosis refers to the excessive buildup of scar tissues that form in an area, leading to a decrease in flexibility corresponding to an increase in stiffness [64]. The risk of liver-related mortality is significantly increased in the presence of NASH fibrosis [1]. The most important and reliable predictors of liver-related mortality are the presence and stage of fibrosis [47, 56]. The stages of fibrosis are usually assessed using the Metavir scale, ranging from F1 (mild fibrosis) to F4 (cirrhosis). Fibrosis can progress from collagen bands to bridging fibrosis and ultimately to cirrhosis [65]. The initial stages of NASH fibrosis, including F1, F2, and F3, are reversible, mostly through lifestyle intervention [66]. Liver regeneration is possible when mild fibrosis is present. Once the liver progresses to end-stage cirrhosis, it cannot be reversed and results in a short lifespan and the requirement for a liver transplant [66]. **Figure 2.4** shows an example of biopsy samples for different stages of fibrosis. Patients often do not exhibit symptoms until decompensation sets in, and at this point, the liver can no longer recover spontaneously [47]. Patients with cirrhosis often experience portal hypertension, which leads to other clinical issues such as ascites, renal failure, hepatic encephalopathy, and variceal bleeding [46, 53, 66].

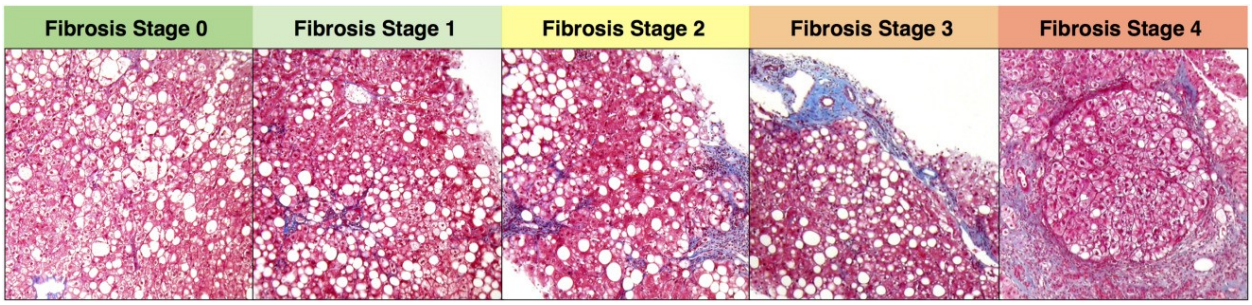

Figure 2.4 Biopsy samples for different fibrosis stages. Adopted from [67].

The classification of diffuse liver diseases includes inflammatory, vascular, and storage diseases. The most common type of liver steatosis is diffuse fatty liver, and microvesicular steatosis is generally distributed throughout the liver, although it may appear in isolated lobes in some cases of NAFLD [68]. However, 10% of NAFLD cases have reported a patchy distribution of microvesicular steatosis [47].

The liver can regenerate itself after moderate damage or tissue removal [69]. Liver regeneration is a well-organized process that involves interactions between the epithelial cell department, matrix proteins, and non-epithelial cells [42]. In cases of moderate liver injury or partial hepatectomy, serum factors can stimulate rapid liver regeneration. Macrophages, hepatic stellate cells, and liver sinusoidal endothelial cells send signals to hepatocytes, causing them to enter mitosis [69].

Although the liver can regenerate quickly after moderate damage, this process becomes much more complicated in diseased livers, such as those affected by HBV, HCV, NAFLD (including NAFL and NASH), in which hepatocytic damage in the form of steatosis and fibrosis occurs, ultimately leading to the depletion of hepatocytes [42]. In these cases, the remaining hepatocytes initiate the regeneration process but are unable to divide efficiently, and the proliferative capability of hepatocytes decreases significantly when there is more than 50% loss of them [42]. In such cases, the liver progenitor cells become activated and proliferate intensely, contributing to further disease progression [42]. Liver regeneration is impaired in advanced NAFLD due to the presence of excessive scar tissue and cellular debris [69]. Thus, early diagnosis

and treatment of liver disease are critical to maintaining its regenerative capabilities and avoiding the need for transplantation [53].

2.2 Diagnostic methods of nonalcoholic fatty liver disease (NAFLD)

Early diagnosis of NAFLD is crucial due to its asymptomatic nature and progression to irreversible cirrhosis. The current diagnostic pathways involve incidental findings and specialist care with transient elastography or diagnostic imaging by trained radiologists. However, the sensitivity of conventional imaging techniques to detect mild hepatic steatosis is limited [70, 71]. Advanced diagnostic methods consist of biopsy, magnetic resonance imaging proton density fat fraction (MRI-PDFF), and CAP [53, 70, 71]. These methods have limitations that are discussed in the following sections.

2.2.1 Blood tests

Blood-based biomarkers are a cost-effective and appealing approach for detecting NAFLD patients, but their ability to accurately diagnose the condition is limited. Several biochemical biomarkers are utilized to predict NAFLD, including aminotransferases, bilirubin, and ferritin. Alanine aminotransferase (ALT) and aspartate aminotransferase (AST) are indicators of fibrosis and steatosis, but their elevated levels have low specificity for NAFLD and are not closely related to histological necroinflammation [64, 72]. In a study of 561 patients with type II diabetes (T2D), 70% and 21% had steatosis and fibrosis, respectively, as determined by transient elastography (TE). In contrast, only 6-7% of the same patient population exhibited increased ALT and AST levels [62]. The combination of different biomarkers can enhance the accuracy of NAFLD diagnosis. Various algorithms have been developed to combine blood biomarkers and elastography but still need further validation [73]. These algorithms are commercial online tools, including NAFLD Fibrosis Score (NFS), BARD, FIB-4, ELF, FibroTest, and FibroMeter [47]. The accuracy of these tests can vary based on factors such as ethnicity and diabetes [73]. While NFS and FIB-4 scores can detect advanced fibrosis with high positive predictive values, they are ineffective in detecting early-stage NAFLD, including steatosis [70]. Recently, new serum biomarkers, such as Pro-C3, have been identified to improve diagnostic accuracy, but they are costly, and their availability is limited. These biomarkers have yet to be used routinely in clinical blood tests [53, 73].

2.2.2 Liver biopsy

Liver biopsy is currently considered the most reliable way to assess liver steatosis, NASH, and fibrosis [47, 62, 70]. It is the only trustworthy method for diagnosing of NASH, a more severe liver condition that requires immediate medical attention and lifestyle changes [74]. However, liver biopsies have limitations and potential interpretation challenges. They are susceptible to sampling errors and intra and inter-observer variation, especially when small biopsy areas are analyzed [66]. Furthermore, pathologists tend to overestimate the proportion of hepatocytes affected by steatosis [47]. Additionally, liver biopsies are highly invasive and impractical as a screening method, requiring a needle at least 20 mm long with a diameter of around 2 mm to collect a specimen that varies between 1 and 3 cm in length [53, 75, 76]. When diagnosing alcoholic or non-alcoholic fatty liver disease, the following distinct histopathological features are examined: (1) accumulation of hepatocellular triglycerides, (2) centrilobular hepatocellular injury that is most severe in the acinar zone, (3) damage to the cytoskeleton which is indicated by hepatocellular ballooning, with or without Mallory-Denk bodies, (4) inflammation in the parenchyma, where lymphocytes and macrophages are most common, but neutrophils may be present in severe cases, and (5) perisinusoidal fibrosis which is characterized by the deposition of collagen in the space of Disse [77]. The National Institutes of Health's NASH Committee (NIH NASH CRN) created a grading system known as the NAFLD Activity Score (NAS) in order to assist in the characterization of liver lesions and to permit statistical analysis in clinical trials (**Table 2.1)**. NAS is based on the assessment of three features: hepatocellular ballooning, lobular inflammation, and steatosis, each of which is assigned a score from 0 to 3. The total score ranges from 0 to 8, with higher scores indicating more severe disease activity [77].

Table 2.1 NAFLD activity score and staging system devised by the Pathology Committee of the NASH Clinical Research Network, adopted from [77].

Feature	Definition	Score
Steatosis grade	Low to medium power evaluation of parenchymal involvement by steatosis)	
	<5%	0
	5%-33%	1
	33%-66%	2
	>66%	3
Lobular inflammation	Overall assessment of all inflammatory foci per 200 × field	
	No foci	0
	<2 foci per 200 field	1
	2-4 foci per 200 field	2
	>4 foci per 200 field	3
Ballooning	None	0
	Few (or borderline) balloon cells	1
	Many cells/prominent ballooning	2
NAS	Sum of Steatosis + Lobular Inflammation + Ballooning	0-8
Fibrosis stage	None	0
	Perisinusoidal or periportal	1
	Mild, zone 3, perisinusoidal	1A
	Moderate, zone 3, perisinusoidal	1B
	Portal/periportal	1C
	Perisinusoidal and portal/periportal	2
	Bridging fibrosis	3
	Cirrhosis	4

Note. NAFLD = nonalcoholic fatty liver disease, NASH = nonalcoholic steatohepatitis.

Liver biopsy is not routinely performed unless in cases where NASH is strongly suspected, as it is usually used as a last resort for diagnosis. However, without biopsy, it is impossible to

accurately determine the degree of steatosis or stage of fibrosis without conducting an ultrasound transient elastography exam. Despite being considered the gold standard for NASH diagnosis, liver biopsies have numerous potential complications that discourage patients and doctors from pursuing the procedure. These complications include hemorrhage, pulmonary complications, peritonitis, and septicemia [78]. Pain is also a common issue, occurring in about 84% of patients who undergo liver biopsies. The risk of bleeding is a grave concern, and it further adds to the reluctance of patients and physicians to undergo liver biopsies [65]. Additionally, liver biopsies are expensive and require trained physicians, and scheduled hospitalization, which makes them an unsuitable screening option for NAFLD [53].

2.2.3 Computed tomography (CT) scan

CT is a method of creating 3D images using X-rays. Different CT imaging protocols can be used to diagnose liver disease, including unenhanced, single-phase, dual-phase, and triphasic contrast-enhanced imaging [68]. Triphasic contrast-enhanced CT is used to detect benign and malignant liver lesions, particularly in patients with cirrhosis who are at risk of developing hepatocellular carcinoma (HCC) [79]. Single-phase contrast-enhanced CT is the standard method for diagnosing diffuse liver pathologies such as liver fibrosis, cirrhosis, and hypovascular metastatic liver disease. However, non-contrast CT of the abdomen is the best method for diagnosing liver steatosis. Fatty liver changes in CT scans appear as bright, diffuse areas compared to the spleen and renal cortex [68]. Radiologists analyze the CT scans and provide detailed descriptions of fatty changes. However, due to the need for radiologist analysis, exposure to radiation, and the high costs associated with CT, it is not often used as the primary diagnostic method for NAFLD [53, 70, 80].

2.2.4 Magnetic Resonance Imaging (MRI)

MRI is a noninvasive medical imaging technique that uses a strong magnetic field and radiofrequency waves to generate images of the body's internal structures. In the context of NAFLD diagnosis, MRI can assess the liver's fat content and detect fibrosis [81].

Several MRI techniques can diagnose NAFLD, including the proton density fat fraction (PDFF) and magnetic resonance elastography (MRE). PDFF is a method that measures the

percentage of fat in the liver and can provide a quantitative assessment of the degree of liver steatosis [81]. MRE uses MRI detection to measure the stiffness of tissues, which can help assess liver fibrosis [82]. MRE typically utilizes an external vibration emitter to evaluate the viscoelasticity of tissues, which is analogous to the technique employed by TE [83]. Shear waves produced by the vibration are imaged at the micron level [73]. MRE is more accurate than transient elastography (TE) in diagnosing the stages of steatosis and fibrosis [84, 85].

MRI has several advantages over other imaging modalities, such as CT and ultrasound. It is noninvasive as ultrasound, does not use ionizing radiation as in CT, and has high sensitivity and specificity for detecting liver steatosis and fibrosis [86]. Additionally, it can provide detailed information about the liver and surrounding structures in 3D without requiring contrast agents [86, 87].

However, MRI has some limitations. It is more expensive than other imaging modalities, and the availability of MRI scanners may be limited in some areas. Additionally, MRI can be affected by motion artifacts and metal implants in the body, limiting its use in certain patient populations [10, 12].

Although MRI-PDFF has high accuracy for diagnosing NAFLD, particularly for patients with suspected advanced fibrosis or those for whom liver biopsy is contraindicated or not feasible, it is not the optimal screening method because it relies on MRI, which is an expensive and not widely available technology [88]. MRI scanning is a more time-consuming process and necessitates patient cooperation through various imaging sequences and breath holding, and may induce claustrophobia-related discomfort [88].

2.2.5 Ultrasound elastography techniques

Ultrasound elastography techniques may be classified based on their source, which can be static and quasi-static (strain imaging) or dynamic (SW imaging). Due to the limited use of strain imaging for NAFLD diagnosis, it is not discussed further in this thesis. Liver elastography is a noninvasive procedure that utilizes low-frequency elastic waves to measure liver stiffness. The technique applies controlled vibrations or pulses to the liver, while sound waves (for TE) or radiofrequency waves (for MRI) are utilized to determine liver elasticity. The primary purpose of this approach is to diagnose fibrosis and steatosis. Fibrosis, in particular, can be detected as an

increase in overall liver stiffness. The available elastography techniques are further explained below. Although they are considered the most accessible noninvasive diagnostic tools, these elastography techniques are typically available only in specialized healthcare settings such as Hepatology and Endocrinology clinics [53]. **Figure 2.5** illustrates the classification of the ultrasound elastography techniques for liver applications.

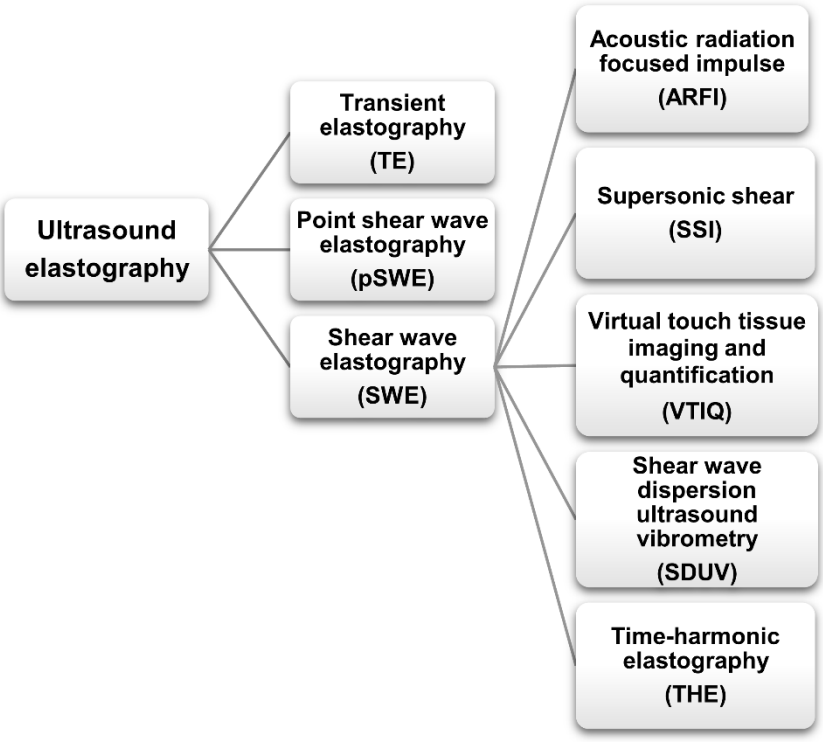

Figure 2.5 Classification of ultrasound elastography techniques for NAFLD diagnosis.

2.2.5.1 Transient elastography (TE)

TE is a fast, repeatable, and safe way for liver stiffness measurement (LSM), which can be done next to the patient and provides instant results [89]. This technique is widely used and has been validated in numerous clinical trials for the assessment of liver fibrosis. In addition, TE generates a compression wave attenuation measurement (CAP) for steatosis, which approximates the attenuation in dB/m at the transient elastography's central frequency [64]. This technique utilizes a single-element ultrasound transducer to produce a short-time transient vibration with

frequency ranges between 50 and 1000 Hz [40]. The first system based on this method was Echosens FibroScan® for assessing liver fibrosis [90]. The acquired data by this technique can provide the SW speed and associated Young's modulus [40]. Although TE is increasingly used in clinical settings, it has some limitations for patients with ascites, narrow intercostal spaces, a body mass index (BMI) greater than 30, or a skin capsular distance greater than 25 mm [73, 91]. Additionally, other limitations include variability between users and within users, and limited sensitivity in patients with NAFLD [73].

CAP is a newly introduced measurable characteristic that depends on the attributes of the ultrasonic signals obtained through the use of the FibroScan® [92]. Although FibroScan® is currently considered the standard for assessing fibrosis and cirrhosis in clinical settings, it is not advisable to use LSM and CAP scores to distinguish between patients with NASH and simple steatosis because they do not assess the degree of inflammation [74]. Research has revealed that NASH's presence can lead to incorrect fibrosis diagnoses through TE. Additional investigations are necessary to determine if the same holds for interpreting CAP results [64]. The overlap between S2 and S3 steatosis-related CAP thresholds is affected by metabolic factors such as BMI and type II diabetes mellitus [73]. **Figure 2.6** shows the measurement technique and an example of a TE exam.

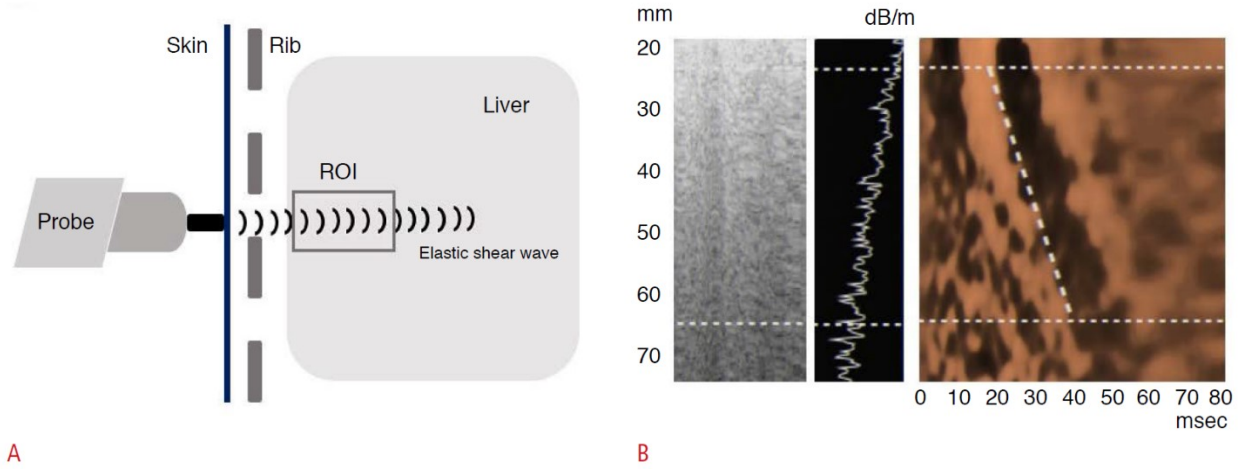

Figure 2.6 The measurement technique of transient elastography (TE). A) TE sends elastic longitudinal waves converted to shear waves for liver stiffness measurement. B. The diagram displays images of the TM-mode, A-mode, and elastogram (TM= time motion, A=amplitude). The TM-mode displays the ultrasonic amplitude in a logarithmic scale as a function of depth and time

and A-mode displays the real-time ultrasonic line amplitude in a logarithmic scale as it varies with depth. The elastogram is a graphical representation of strain rate over time and depth, presented in a two-dimensional format. The area of interest is referred to as the ROI in A. Adopted from [93].

2.2.5.2 Point shear wave elastography (pSWE) and its derivatives

Point shear wave elastography (pSWE) involves using acoustic radiation force impulse (ARFI) to cause tissue displacement in a specific location in a normal direction to the tissue, similar to how ARFI strain imaging works. Both methods are commercialized by Siemens Healthcare. Unlike ARFI strain imaging, the amount of tissue displacement is not measured in pSWE mode. Instead, a portion of the longitudinal waves produced by ARFI is converted to SWs through the absorption of acoustic energy [17]. The speed of SWs perpendicular to the excitation plane is then measured and either reported directly or converted to a Young's modulus to give a quantitative measurement of tissue elasticity [23].

In contrast to TE, pSWE can be performed using a standard ultrasound probe on a conventional ultrasound system [94]. When using pSWE for liver applications, there are several benefits compared to using TE. Firstly, the operator can use B-mode ultrasound to directly visualize the liver and select a uniform area of tissue that does not contain large vessels or dilated bile ducts. Additionally, pSWE produces SWs that originate locally within the liver, unlike TE, where SWs are generated by the excitation at the body surface. pSWE is less susceptible to being influenced by ascites and obesity [21, 23, 24].

Point quantification elastography (PQE) enters into the category of pSWE measurements. Although there is not much published information regarding the effectiveness of ElastPQ in assessing liver fibrosis in patients with CVH and NAFLD, the preliminary studies conducted to evaluate the performance of this method have shown positive results [95]. This technique is similar to supersonic SW imaging (SSI) but uses a different compression pulse to generate SWs. It also uses a different algorithm to analyze the resulting wave data and to calculate tissue stiffness. ElastPQ®, a technology of Philips Healthcare, is a one-dimensional technique that can be integrated into a standard ultrasound system. It can be performed using the same device used for conventional ultrasound scans. An ROI (region of interest) can be placed anywhere in the

visualized liver parenchyma. The system displays the result in kPa, and provides mean, median, and deviations of valid measurements immediately after the image-guided acquisition.

ElastPQ was superior to TE for diagnosing significant fibrosis in a pilot study [96]. Also, in a retrospective study [97], the diagnostic performance of ElastPQ was assessed. It had good to excellent performance for staging fibrosis in patients with chronic liver diseases. More expertise is necessary for using ElastPQ or pSWE compared to TE. Typically, a radiologist or a sonographer is required, and both techniques are not as suitable as TE for use at the point of care. There are today enough published studies for meta-analysis of the effectiveness of pSWE in diagnosing liver fibrosis [98].

2.2.5.3 Two-dimensional shear wave elastography (2D-SWE)

The 2D-SWE is an ultrasound-based technique to assess tissue stiffness or elasticity. It uses ultrasound compression waves to generate and measure the speed of SWs created by mechanical vibrations or pressure to the tissue [20, 24, 73]. The ultrasound probe generates a focused energy (radiation pressure) that creates SWs in the targeted tissue. These waves travel from the focal point to create a wavefront on both sides of the focal point. Multiple focal points are created in a line perpendicular to the skin surface (**Figure 2.7**) [23]. Common approaches for producing SWs in a specific tissue include using acoustic radiation force impulse (ARFI) imaging [17, 99] and supersonic shear imaging (SSI) [100, 101] techniques. These methods involve using a remote ultrasound probe to create a tissue motion through acoustic radiation force, and then tracking this motion with motion-tracking algorithms applied on ultrasound echoes. The ultimate goal is to measure the tissue stiffness indirectly by observing the movement of SWs within the tissue. The idea behind SWE is that the stiffness or elasticity of a tissue is related to its pathological state. SWs move faster in more rigid tissues and slower in softer tissues. For example, fibrosis and cirrhosis can cause the liver to become stiff, and SWE can be used to quantify this stiffness. SWE can be a valuable tool for diagnosing liver diseases and monitoring their progression, as it can detect changes in tissue viscoelasticity over time [20]. SWE is similar to other elastography techniques, such as TE and MRE, which use noninvasive methods to measure tissue elasticity. However, SWE is less expensive and more widely available than MRE. It also provides SWE maps superimposed on anatomic B-mode images, which is not possible with TE.

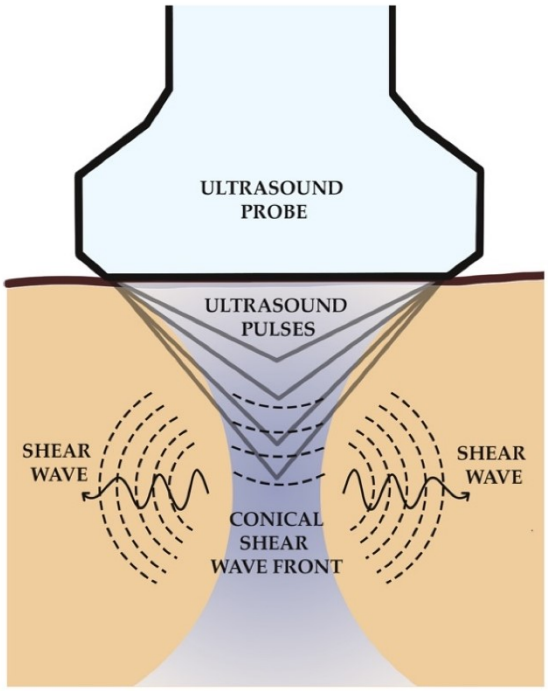

Figure 2.7 The technical concept of shear wave elastography, adopted from [102].

Additionally, SWE has the advantage of providing real-time imaging of the tissue being examined, which can help guide medical procedures, such as biopsies [103]. This method shares comparable advantages with pSWE. It enables the production of quantitative elastography through rapid imaging. Advantageously, placing multiple ROIs on elastograms can decrease the sampling variability that may arise with 1D TE and pSWE [104]. SWE has many advantages over traditional methods assessing the liver condition, such as liver biopsy that is an invasive procedure associated with several risks. SWE is noninvasive, fast, and can be repeated as often as needed to monitor disease progression. However, SWE still has some limitations, such as the lack of standardization across different manufacturers, and the need for more studies to determine optimal parameter thresholds for using SWE in clinical practice. Nonetheless, SWE has shown promise as a valuable tool for diagnosing liver diseases and other conditions that affect tissue stiffness [101, 103, 105]. In what follows, some approaches which fall under the umbrella of SWE are described. They are described sequentially as in **Figure 2.5**.

2.2.5.3.1 Acoustic radiation force impulse (ARFI) shear wave elastography and its derivatives

Sarvazyan et al. [106] suggested a technique that utilized a focused beam of acoustic radiation force to produce SWs in a localized area. The propagation of these SWs away from the push location of the radiation force was then monitored using ultrasound imaging. As the same transducer was used to generate the SWs and track their propagation, it was feasible to use B-mode image guidance during the measurement [107-109].

The work of Sarvazyan et al. [106] inspired research and commercialized developments of the technique. ARFI uses high-intensity ultrasound beams (acoustic radiation force (ARF)) to create mechanical vibrations in the tissue. The speed of the resulting SWs is then measured to determine tissue stiffness. ARF can be used at a single focal location or using a configuration of multiple focal zones. When using multiple focal zones, each zone is rapidly interrogated one after another, allowing the real-time formation of SW images [17]. Various ARFI-based techniques produce local maps of SW speed or Young's modulus, and 2D images of these properties. These modalities can provide a few frames per second [109].

Alternatively, vibroacoustography, proposed by Fatemi and Greenleaf [110], vibrates tissues in the kHz range using ARF generated by two slightly different ultrasound frequency overlapping beams. The tissue's mechanical response depends on its local acoustic mechanical properties, measured using a hydrophone. Vibroacoustography could visualize microcalcification with a high contrast resolution [107, 110]. McAleavey and Menon's technique [111] labeled SMURF generates a SW of known spatial frequency and measures the temporal frequency response of the vibrating tissue as the wave propagates through a point. Elegbe and McAleavey's "single tracking location ARF" approach [112] follows induced SWs and is less sensitive to speckle-induced phase errors. Song et al. [113, 114] applied multiple unfocused and focused ultrasound beams in a comb pattern to generate SWs, and used a directional filter to isolate left-to-right and right-to-left propagating waves to obtain smoother 2D SW speed maps.

Countless clinical studies have been published using ARFI imaging and SWE on various ultrasound systems. These studies have led to the development of general guidelines for these methods, and specific guidelines for certain organs [101, 109, 115-120]. However, these guidelines are subject to changes as the technology advances and more knowledge is gained [19]. Measuring the SW speed in the liver could provide valuable information about liver fibrosis, as fibrosis causes

the liver to become stiffer [101, 119]. Since the liver is viscoelastic like most soft tissues, SW velocity dispersion methods have been implemented [121-123]. Measuring deep organs such as parts of the liver or liver in obese patients may require specialized focusing or specific transducers to obtain accurate measurements. Using longer ARF push pulses may also be necessary to induce sufficient motion for measurement [19].

Several radiology companies have incorporated ARF-based methods to enable measurements in different organs for clinical purposes. In addition, Verasonics [124] and S-Sharp, both manufacturers of research devices, are noted for their ability to generate ARF and to develop novel measurement techniques [19]. The use of ARF is expected to persist and progress, with new emerging applications evolving and becoming more sophisticated. Future research and developments should aim to utilize this versatile tool for noninvasive and noncontact tissue displacement assessment [19].

2.2.5.3.2 Supersonic shear imaging (SSI)

Supersonic shear imaging (SSI) is considered an established method for ultrasound SWE [125]. Bercoff et al. [100] developed an ultrasound scanner with an ultra-high frame rate of up to 15,000 frames per second that can track SWs generated by an ARF impulse in the tissue resulting in high temporal resolution. This approach, known as SSI, involves firing at different depths multiple ARF impulses at a rapid rate compared to the relatively slow SW propagation speed. The Aixplorer's SSI system employs a cone-shaped quasiplanar wavefront and an ultrafast imaging method to monitor the displacement of SWs across an entire imaging plane. The speed of these SWs is then measured to calculate tissue stiffness [126]. SSI has been used to study the viscoelastic properties of breast lesions [127], muscles [128], and livers [101], to name a few examples. The ability to position multiple regions of interest (ROIs) on elastograms helps to reduce sampling variability that can arise with TE and pSWE [104].

2.2.5.3.3 Virtual touch tissue imaging and quantification (VTIQ)

This technique also uses ultrasound to create SWs in the tissue. However, it employs a different method for measuring tissue stiffness, using a virtual touchpad that allows the operator to apply a pressure and measure the resulting tissue deformation. Virtual touch quantification (VTQ) liver elastography gauges the velocity of SWs produced by a brief acoustic force impulse.

The outcome is conveyed in meters per second velocity units (m/s) [99]. Several reports suggest that VTQ may serve as a predictive factor for post-hepatectomy liver failure or be beneficial in assessing liver fibrosis [99, 129-131].

2.2.5.3.4 Shear wave dispersion ultrasound vibrometry (SDUV)

This technique uses multiple ultrasound beams to create a spatially varying vibration field in the tissue, and measures the resulting SW dispersion to calculate tissue stiffness. This method was proposed by Chen et al. [132] using amplitude modulated ultrasound to generate a monochromatic SW and to measure its phase velocity. This technique hypothesizes that the SW velocity is frequency dependent and dispersive in viscoelastic media [132]. Compared with TE, pSWE, ARFI or SSI, this approach has the advantage of being able to estimate viscoelastic properties of tissues. Nevertheless, a drawback is that it requires several measurements with varied ultrasound modulation frequencies. However, using a single sequence with significant energy over multiple frequency components makes it possible to obtain data and assess SW velocity dispersion in one measurement [133]. Another advantage is that this method is simple to implement on clinical ultrasound scanners since pulses have a constant amplitude and only need to be turned on and off. Some applications involved external mechanical actuation to generate SWs instead of using an ultrasound radiation force, providing more flexibility in experiments [134-136]. SDUV has been shown to be effective in making measurements in the liver [137].

2.2.5.3.5 Time-harmonic elastography (THE)

Another form of ultrasound-based elastography technique, known as two-dimensional time-harmonic elastography (THE), has been created. This technique uses a series of low-frequency vibrations to induce SWs in the tissue, which can be measured using ultrasound. The resulting wave dataset is analyzed to calculate tissue stiffness. It differs from conventional methods that employ short stimulation [138]. Instead, THE employs a constant multifrequency range of SWs generated by an external vibration device integrated into the patient bed. This enables THE to generate elastograms that cover the entire field of view of the ultrasound image, reaching depths of up to 13 cm below the body surface, much like MRE [139]. A study by Moga et al. [140] assessed the diagnosis performance of THE for assessing liver fibrosis, considering vibration-controlled transient elastography as a reference method. The findings suggested that THE is a

viable and consistent method for elastography, which can effectively determine the presence or absence of severe liver diseases [140].

2.2.6 Diagnostic B-mode ultrasound

A meta-analysis found that B-mode ultrasound has an 85% sensitivity and 94% specificity for detecting moderate to severe fatty liver compared to biopsy [13]. However, dichotomization into various stages of steatosis is more difficult with B-mode ultrasound alone [13, 141-143]. Ultrasound images can reveal fibro-fatty tissues as bright spots in the liver. The portal triad, a group of blood vessels, appears less distinct on B-mode ultrasound images in the case of non-alcoholic fatty liver disease [64]. This is illustrated in **Figure 2.8** as fat accumulation in the liver increases. The decreased visualization of the portal triad is due to higher signal attenuation, which is more pronounced in patients with steatosis.

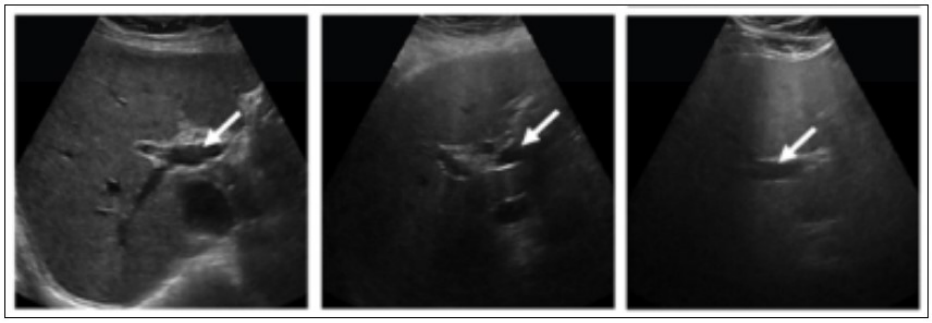

Figure 2.8 A collection of liver ultrasound images featuring the portal vein can be seen from left to right, showing increasing fat accumulation (7%, 19%, 39%), adopted from [144].

Skilled radiologists can detect fatty liver disease by comparing the liver's echogenicity to that of the spleen and renal cortex [145]. Quantitative methods, such as the hepatic/renal ratio (H/R) and hepatic attenuation rate, can also be used to assess fatty liver disease severity using B-mode ultrasound [146]. However, there are several drawbacks to using ultrasound for liver diagnosis, such as the need for an experienced operator, the possibility of motion artifacts that can affect the accuracy of the H/R index, and the requirement for interpretation by a trained radiologist [73]. A skilled sonographer must capture clear images of the liver and right kidney in a single

plane [147]. Both sonographers and radiologists require years of training and experience to conduct thorough and systematic evaluations [148].

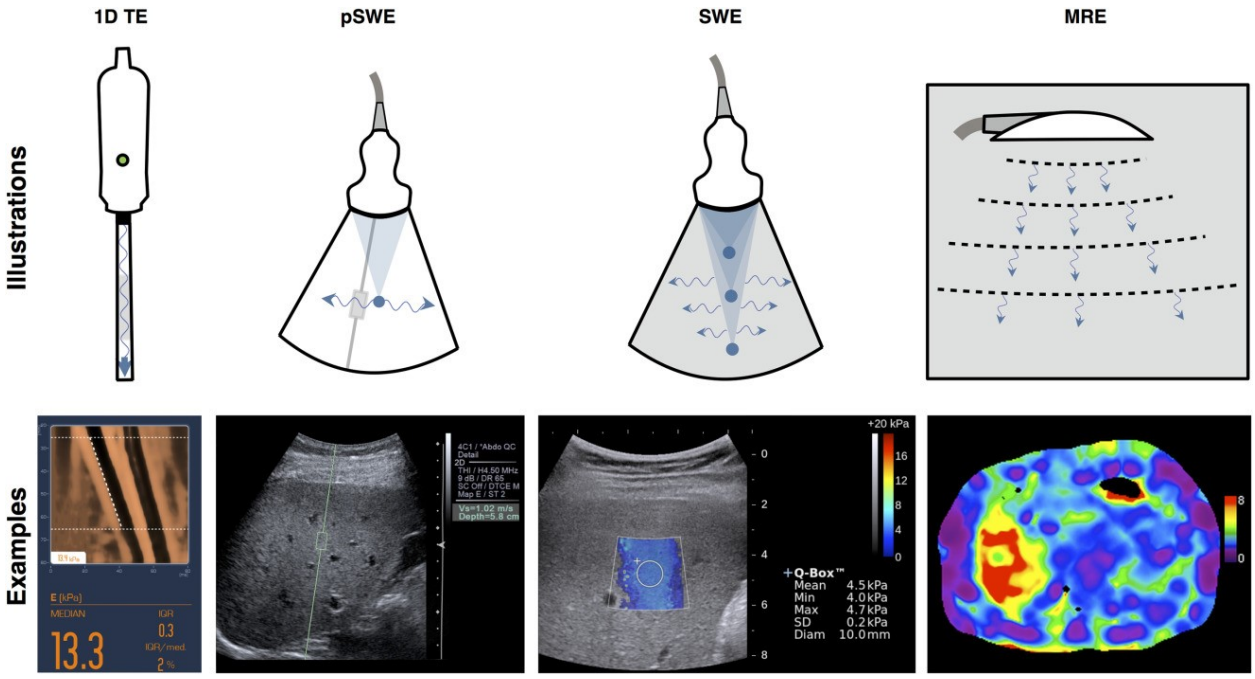

Figure 2.9 The overview of liver elastography techniques and companion images, adopted from [65].

Figure 2.9 showed a graphical summary of liver elastography techniques and their examinations' examples.

To conclude this section, based on advantages and limitations of current techniques for NAFLD diagnosis (**Table 2.2)**, liver elastography using SWE is considered in the remaining of this thesis for NAFLD diagnosis. The following chapter presents basic principles of SWE and a literature review on ultrasound SW attenuation imaging.

Table 2.2 Summary of advantages and limitations of available elastography techniques.

Elastography techniques	Advantages	Limitations
MRE	✓ High diagnostic accuracy in staging steatosis ✓ Increasing the size of liver images may lead to a decrease in sampling variability, which could be beneficial for monitoring changes over time ✓ Incremental cost of hardware and software lower than cost of a new 1D transient elastography device ✓ Low energy absorption by tissues	• Large ROIs not always obtainable because of SW attenuation in normal livers • Limited availability • Expensive • Acquisition with different breath-holds • Requires postprocessing and offline analysis • Acquisition time is too long, which is an issue for claustrophobia • Non compatible with implants
TE	✓ Widely available, portable, cost effective ✓ Low SW frequency (50 Hz) ✓ Low energy absorption by tissues ✓ Clinically available for point of care scans ✓ Validated with good accuracy ✓ Diagnose liver fibrosis using liver stiffness measurement (LSM) ✓ Diagnose liver steatosis using controlled attenuation parameter (CAP)	• Failure and unreliable results due to obesity, narrow intercostal space, ascites • Does not provide a B-mode image and does not record exact measurement location • Inter-user and intra-user variability, and inadequate sensitivity in NAFLD • Presence of NASH increases the false-positive diagnosis of fibrosis • Metabolic factors including BMI and type II diabetes mellitus cause overlaps between S2 and S3 steatosis associated CAP thresholds • requires a trained medical professional
pSWE	✓ Widely available, portable, cost effective ✓ ROI selection ability based on B-mode images ✓ More robust than TE ✓ Superior to TE to diagnosis fibrosis	• More expertise required than TE (requires a radiologist or sonographer) • Less validated than TE • Higher energy absorption than TE • Not suitable for point of care diagnosis
SWE	✓ Widely available, portable, cost effective ✓ Same advantages as pSWE ✓ Several ROIs can be positioned on elastograms ✓ Lower sampling variability that can occur with TE and pSWE ✓ Generation of quantitative elastograms ✓ Fast in acquisitions	• Same limitations as pSWE • Fewer studies on its diagnostic performance for staging liver steatosis and fibrosis than TE and pSWE

NAFLD = nonalcoholic fatty liver disease, NASH = nonalcoholic steatohepatitis, pSWE = point shear wave elastography, SW=shear wave, SWE = shear wave elastography, TE = transient elastography.

Chapter 3 – Technical description of the ultrasound shear wave elastography method

3.1 Basic physics of ultrasound shear wave elastography

The methods used in the early stages of elastography imaging considered the tissue as isotropic and purely elastic. These approaches have been well-documented, and the main constitutive relations necessary for understanding SWE are summarized here. Elastography is a technique that evaluates the elasticity of tissues, which refers to their ability to resist deformation when subjected to an external force and return to their original shape when the force is removed [20].

The relationship between the stress applied to the tissue and its strain response is described by Hook's law:

$$\sigma = \Gamma . \varepsilon \qquad (3.1.1)$$

In the above equation, σ and ε refer to the stress (force per unit area in kilopascals, where 1 kPa = 1000 N/m^2) and the strain (expansion per unit length which is dimensionless) tensors, respectively, and Γ represents the elastic modulus. The method of deformation defines three categories of elastic moduli Γ, namely the Young's modulus (E), the shear modulus (G), and the bulk modulus (K). Increased stiffness can be attributed to a material's greater resistance to deformation, which is directly related to a higher elastic modulus Γ. The shear modulus G is used to define SWs, which exhibit particle motion perpendicular to their direction of propagation.

$$c_s = \sqrt{\frac{G}{\rho}} \qquad (3.1.2)$$

In the equation above, ρ represents the density of the material in units of kilograms per cubic meter. The SW speed (c_s) ranges from approximately 1-10 m/s in soft tissues, which facilitates high contrasts in G between tissues and makes them suitable for elastography measurements.

There is a relationship between deformation and elastic modulus, as a solid tries to maintain its original volume. This relationship is described by the Poisson's ratio (v). Although its proof is

not discussed in this thesis, the relationship between the Young's modulus (E) and the shear modulus (G) can be expressed as follows [109].

$$E = 2\,(v + 1)\,G \qquad (3.1.3)$$

Using Equation 3.1.3 and taking into account the fact that soft tissues have a high-water content, which results in a Poisson's ratio close to 0.5 (similar to that of an incompressible medium), then, we can arrive at the following result:

$$E = 3G = 3\rho c_s^2 \qquad (3.1.4)$$

The measurement of c_s enables to estimate the values of E and G. In most applications, G refers to the magnitude of the storage modulus because purely elastic solids are considered. For viscoelastic media, G is a complex number ($G = G' + iG"$), where G' is the storage modulus, $G"$ the loss modulus, and i the imaginary number. The units of E and G are in kg/m.s^2 or N/m^2 or kilopascals (kPa). Understanding the relations between the Young's modulus (E), the shear modulus (G), and the SW speed (c_s) is crucial because different elastography techniques and vendors report various parameters. In MRE, the magnitude of the complex shear modulus (G) is reported, which consists of both elastic and viscous components, and is calculated from phase-contrast multiphase pulse sequence data [21]. On the other hand, ultrasound SW imaging directly measures the SW speed (c_s), which is either reported or converted to a Young's modulus (E). Although Equation 3.1.4 does not describe dependent variables, both E and G depend on the frequency of the excitation used, making it difficult to compare E reported in ultrasound SW imaging and G reported in MRE [23]. **Figure 3.1** shows a summary of SWE in three steps.

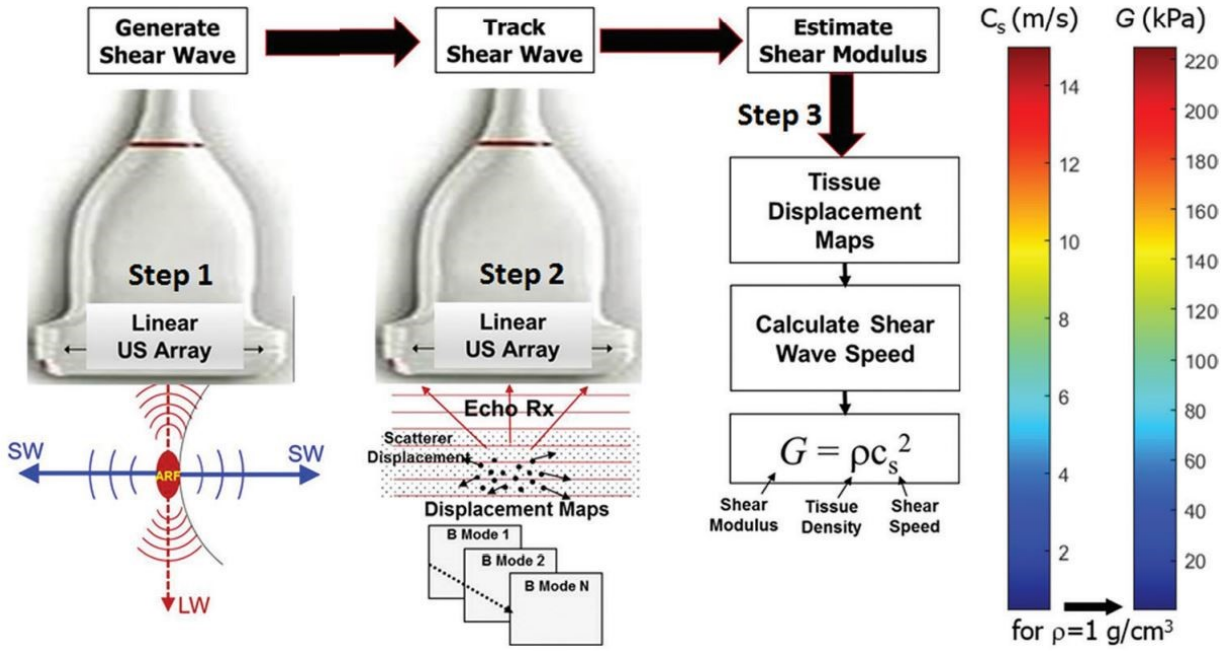

Figure 3.1 A summary of shear wave elastography physics. Step 1 involves the use of an acoustic radiation force to generate shear waves, which propagate perpendicular to the primary ultrasound source at a lower velocity than the transmitted compression waves in the MHz range. In Step 2, fast plane wave excitation is utilized to monitor the displacement and speed as the shear waves propagate, and tissue displacement is computed using a speckle tracking algorithm. In Step 3, the tissue displacements are used to estimate the shear wave speed (c_s) and shear modulus (G), displayed using color maps. Adopted from [149].

3.2 Ultrasound shear wave propagation in a viscoelastic medium

Due to the viscoelastic nature of soft tissues, determining their elasticity and viscosity involves solving a complex model. There are proposed methods to reconstruct tissue viscoelastic properties, but these typically only reconstruct elasticity and estimate viscosity based on assumptions of tissue rheology models such as the Kelvin-Voigt model [101, 121, 132]. Amador et al. [150] proposed a local quantification of the complex shear modulus obtained by measuring the acoustic radiation force-induced creep, which requires recordings at multiple tissue locations. Orescanin et al. [151] proposed using numerical solutions of Navier's wave equation to compute the complex shear modulus. SW dispersion has also been explored to compute viscoelastic

properties in liver tissues [34, 122, 152, 153]. Analytical inverse problem solutions of SW scattering from a mechanical inclusion were also proposed to compute viscoelastic properties. However, these studies required a simplified experimental geometry to be known beforehand [154-156]. A recent study incorporated mechanical inclusion's geometry into the inverse problem solution, resulting in the ability to obtain viscosity measures. However, only a single measurement representing the mean inclusion viscosity as a function of frequency could be obtained [157]. Shear loss modulus (G'') properties can provide additional information for tissue characterization by allowing the estimation of a viscosity map of the tissue [27].

Some methods assume that SWs created using an acoustic radiation force sequence propagate with cylindrical wavefronts. The cylindrical wavefront model assumes that the propagation medium is macroscopically homogeneous and isotropic to obtain a quantitative estimation of the mean viscoelasticity. Kazemirad et al. [158] presented a model-independent method for quantitatively measuring viscoelastic parameters based on this assumption. However, this assumption may not be valid when considering inhomogeneous media such as tissue with a tumor. Also, Budelli et al. [159] and others [160, 161] used these assumptions to provide methods for quantitative viscoelastic measurements. A recent method proposed by another study estimated tissue viscosity without making assumptions about the wave front geometry, using SW speed and attenuation computed by the frequency shift method [27, 28]. In the next sections, a summary of the physics behind these assumptions are presented.

3.2.1 Cylindrical wave assumption

The wave motion in an infinite, homogeneous, and isotropic viscoelastic material is governed by the Navier's equation. When assuming that there is a pure SW propagation inside a soft tissue, the simplified wave equation can be written as [162]:

$$\rho \frac{\partial^2 u(r,t)}{\partial t^2} = G\Delta^2 u(r,t) \qquad (3.2.1)$$

In the above equation, ρ is the density, G is the complex shear modulus, and $u(r,t)$ is the transverse displacement vector in space–time [27]. When considering a cylindrical SW propagation, the solution to the wave equation in the frequency domain can be expressed as [158]:

$$U(r,\omega) = a(\omega)\frac{i}{4}H_0^1(\hat{k}(\omega)r) \qquad (3.2.2)$$

In this equation, r, ω, $a(\omega)$, H_0^1, and $\hat{k}$ represent the radial direction of the assumed cylindrical coordinate system, the angular frequency, the amplitude term, the Hankel function of the first kind of order zero, and the complex wavenumber, respectively. It is possible to express the propagation of SWs using the displacement amplitude and the phase angle, which is also stated in reference [158]:

$$U(r,\omega) = \big||U(r,\omega)|\big|e^{-i\theta(U(r,\omega))} \qquad (3.2.3)$$

where $U(r,\omega)$ and $\theta(U(r,\omega))$ are the displacement amplitude and the phase angle.

Kazemirad et al. [158] and Budelli et al. [159] introduced an equation that takes into account the diffraction correction by assuming a cylindrical shear wavefront:

$$\log_e\big(\big||U(r,\omega)|\big|\big) = \log_e(||U_0(r,\omega)||) - r\alpha - \frac{\log_e(r)}{2} \qquad (3.2.4)$$

Here, $U_0(r,\omega)$ is the initial displacement and by least square fitting of this equation, the attenuation coefficient (α) can be computed. Readers are referred to [158, 159] for more details. Despite its usefulness, this approach has certain limitations. One of the main limitations is that it assumes that acoustic pushes occur simultaneously in a uniform medium, creating cylindrical wavefronts that extend infinitely. However, linear US probes generate a radiation force that is not infinitely long in the depth direction, and the shear wavefronts they generate are not perfectly cylindrical either. These waves decrease in amplitude slower than cylindrical waves, as noted in [161]. Additionally, many biological tissues are either anisotropic or heterogeneous. In such cases, using the cylindrical wavefront assumption may lead to a tissue-specific bias in calculating the attenuation coefficient [27].

3.2.2 Frequency shift method theory

Our research group recently introduced a new method for characterizing SW propagation in soft tissues, specifically for use in dynamic SWE. This is called the frequency-shift (FS) method that considers the amplitude spectral distribution for attenuation computation. Unlike other methods, this one does not rely on the assumption of a cylindrical wavefront and is not restricted by geometric factors [28]. The theory of this method is described in **4.4.1** in chapter 4.

3.3 Viscoelasticity reconstruction and its application in liver

3.3.1 Shear wave viscoelastic parameters considered in this thesis

Table 3.1 Shear wave viscoelastic parameter definitions.

Viscoelastic parameter (unit)	Definitions
Shear wave speed (m/s)	Velocity of shear waves that move through a tissue when it is mechanically stimulated
Shear wave attenuation (Np/m/Hz)	Waves' energy and amplitude reduction while moving through a tissue
Shear wave dispersion (m/s/kHz)	The slope of the wave velocity vs. frequency.
Young's modulus (kPa)	The stiffness or elasticity of a tissue in response to an applied force.
Shear modulus (kPa)	The elastic shear stiffness of a material (the ratio of shear stress to the shear strain).
Viscosity (Pa.s)	The hysteretic effect between stress and strain applied on a tissue.

The SW viscoelastic parameters are defined in **Table 3.1**. The SW speed was measured using the phase velocity [163]. The SW attenuation was assessed using different implementations of the FS method, and comparisons were made with the AMUSE algorithm [28, 29, 31, 164]. These attenuation measurements methods are described in Chapter 4 (**section 4.4**). The change in SW speed with frequency is known as SW dispersion, which occurs in a viscoelastic medium [132]. Specific techniques have utilized SW dispersion to assess tissue viscoelastic properties [132, 163]. Notice that SW dispersion measurements can be affected by the finite thickness of a tissue due to reflections during propagation, potentially leading to wave mode conversion [165-167] [168, 169]. The Young's modulus and shear modulus were computed based on **section 3.1**. The viscosity was calculated based on the loss moduli of shear modulus. More details on the viscoelastic parameters' computations are provided in Chapter 6 (**section 6.4**).

3.3.2 The application of viscoelastic parameters in NAFLD diagnosis

Liver elastography is a valuable tool for assessing fibrosis in the NAFLD. However, its effectiveness in detecting steatosis (fat accumulation in the liver) in the early stages of liver disease is not well-established [24, 115, 170]. There are differing opinions on how steatosis affects SW speed in the liver, which has been the primary focus of elastography studies. Among US techniques for liver fat quantification, SW dispersion (SWD) correlates with steatosis grades [34, 37, 171, 172]. However, some studies have explored the SWs attenuation in tissues as a parameter related to tissue viscoelastic loss [160, 173, 174]. Recently, researchers proposed a theoretical examination of the rheology of steatosis, which predicted that the SWs attenuation should increase as the amount of fat in the liver increases [175]. This theory is based on the classic treatment of composite media with spherical inclusions, where the fat vacuoles provide a predominantly viscous contribution.

Additionally, recent theoretical work has produced analytical models for SWs generated by radiation force push pulses from scanning transducers and estimators for SW speed and SW attenuation [168]. Then, these estimators were assessed in a clinical study of 20 subjects who had undergone liver biopsy. It was concluded that higher grades of steatosis were associated with greater SW attenuation [176]. According to experiments conducted on fatty duck livers in preclinical studies, as this thesis's first objective, SW attenuation changed according to the amount of fat present [164]. However, there have been limited investigations into whether SWA is practical and effective in diagnosing NAFLD [164, 176, 177].

This thesis mainly focused on SWE to compute SWA and utilize it for diagnosing NAFLD and staging steatosis. In the following chapters, the articles following the objectives of this thesis are provided.

Chapter 4 – The revisited frequency-shift (R-FS) method for shear wave attenuation computation and imaging

4.1 Introduction to manuscript

This chapter reproduces the content of a published article 'The revisited frequency-shift (R-FS) method for shear wave attenuation computation and imaging' in the journal "IEEE Transactions on Ultrasonics, Ferroelectrics, and Frequency Control (Vol. 69, p. 2061-2074, 2022) by Ladan Yazdani, Manish Bhatt, Iman Rafati, An Tang, and Guy Cloutier after evaluation by a peer review committee.

The following is the order of authors for this published article and corresponding affiliations:

Ladan Yazdani[1,2], Manish Bhatt[1,3], Iman Rafati[1,2], An Tang[4,5], and Guy Cloutier[1,2,5,*]

[1] Laboratory of Biorheology and Medical Ultrasonics, University of Montreal Hospital Research Center (CRCHUM), Montréal, QC, Canada;

[2] Institute of Biomedical Engineering, University of Montreal, Montréal, QC, Canada;

[3] Department of Electronics and Electrical Engineering, Indian Institute of Technology, Guwahati, India;

[4] Laboratory of Clinical Image Processing, CRCHUM, Montréal, Québec, Canada;

[5] Department of Radiology, Radio-Oncology and Nuclear Medicine, University of Montreal, Montréal, QC, Canada.

[*] Corresponding author

The contributions of all authors of the published article are detailed below:

Ladan Yazdani: developed and implemented the corresponding improvements in the algorithm of FS method for shear wave attenuation estimation, A-RANSAC line fitting method, finite element model for making simulation or numerical phantoms in COMSOL, and *in vitro* homogenous phantoms and performed the post-processing of the data, drafted the manuscript and responded to the reviewer's comments of the article.

Manish Bhatt: performed *in vivo* data acquisitions, suggested improvements of non varying shape parameter and RANSAC line fitting in shear wave attenuation estimation algorithms, helped in making *in vitro* phantoms, and contributed to the drafting and revision of the manuscript.

Iman Rafati: contributed to the computation procedure and the revision of the manuscript.

An Tang: contributed to the interpretation of the clinical validation of the proposed method, results, and revision of the manuscript.

Guy Cloutier: supervised this work as the research director, contributed to the interpretation of results as the project director, corrected, and finalized the manuscript for submission and revision.

4.2 Abstract

Ultrasound shear wave (SW) elastography has been widely studied and implemented on clinical systems to assess elasticity of living organs. Imaging of SW attenuation reflecting viscous properties of tissues has received less attention. A revisited frequency shift method (R-FS) is proposed to improve robustness of SW attenuation imaging. Performances are compared with the frequency-shift (FS) method that we originally proposed, and to the two-point frequency shift (2P-FS) and attenuation measuring ultrasound SW elastography (AMUSE) methods. In the proposed R-FS method, the shape parameter of the gamma distribution fitting SW spectra is assumed to vary with distance, in contrast to FS. Secondly, an adaptive random sample consensus (A-RANSAC) line fitting method is used to prevent outlier attenuation values in the presence of noise. Validation was made on ten simulated phantoms with two viscosities (0.5 and 2 Pa.s) and different noise levels (15 to -5 dB), two experimental homogeneous gel phantoms, and six *in vivo* liver acquisitions on awake ducks (including three normal and three fatty duck livers). According to conducted experiments, R-FS revealed mean reductions in coefficients of variation (CV) of 62.6% on simulations, 62.5% with phantoms, and 62.3% *in vivo* compared with FS. Corresponding reductions compared with 2P-FS were 45.4%, 77.1%, and 62.0%, respectively. Reductions in normalized root-mean-square errors for simulations were 63.9% and 48.7% with respect to FS and 2P-FS, respectively.

Keywords: Attenuation measuring ultrasound shear wave elastography, fatty liver, frequency shift, shear wave attenuation, shear wave elastography, two-point frequency shift, ultrasonography.

4.3 Introduction

Ultrasound (US) SW elastography is an established technology that utilizes a clinical US system to noninvasively assess mechanical properties of soft tissues [178]. This technique is based on the monitoring of SW propagation in biological tissues. Shear waves can be generated within the target tissue by focusing US push beams using a remote US probe [22, 25]. The US probe first generates an acoustic radiation force that induces transient SWs in the tissue, and then detecting the SW motion is done via tracking algorithms [17]. Faster propagation of SWs in stiffer tissues than softer ones has been used to characterize the severity of diffuse liver disease and focal lesions [26, 101, 128]. In recent years, SW attenuation is receiving attention to characterize biological tissues [31, 157, 176]. Shear wave speed and attenuation are basic properties of viscoelastic tissues that can be used for pathological organ diagnosis [101, 128].

The stiffness of a purely elastic medium is often quantified in terms of its Young's modulus (E) given as $E = 3\rho c^2$ (here, ρ is the medium density assumed constant, and c is the SW speed). However, biological tissues are inherently viscoelastic in nature as they behave both as solid-like and fluid-like materials [148]. Past studies have utilized the SW speed frequency dispersion to estimate viscoelasticity through the assumption of a rheological model (often Kelvin-Voigt) [34, 132, 163, 179]. Kazemirad et al. [28] proposed a rheological model-free method for quantifying the frequency-dependent shear modulus, under the assumption of a homogeneous and isotropic medium, and a cylindrical SW propagation front to correct for wave diffraction. A similar diffraction correction method was proposed by Budelli et al. [159] using similar hypotheses. There are also some other estimators of tissue viscoelastic properties, such as group SW speed (gSWS) [180], fractional derivative gSWS [181], and reverberant SW [182].

State-of-the-art alternative methods for viscoelasticity estimation rely on SW attenuation computation [31, 123, 157, 176], which has been a challenge due to variance under noisy conditions [29]. The attenuation measuring US shear-wave elastography (AMUSE) method improved robustness to noise by using a two-dimensional k-space frequency analysis within a

region-of-interest (ROI) [31]. However, this approach does not provide imaging capability due to the requirement of analyzing the whole ROI to provide an estimate. As other SW attenuation methods [29, 157], it does not assume any rheological model, and the hypothesis of a linear, homogeneous, and isotropic viscoelastic medium remains a requirement for AMUSE.

The frequency-shift (FS) method proposed by Bernard et al. [157] to image SW attenuation was built on the hypothesis that geometrical diffraction spreading effects are independent of the SW frequency, and that attenuation depends linearly on frequency. Consequently, the FS method does not require the acoustic radiation force source to be planar (i.e., infinitely long) or cylindrical. The main novelty of this work was to hypothesize that the frequency domain amplitude spectrum of SWs follows a gamma distribution, and that the rate parameter of this gamma fit is related to SW attenuation by a linear relation. However, in its current form, retrieving the rate parameter by a linear frequency fitting can be challenging under noisy conditions. Kijanka et al. [29] proposed a modification to the FS method (named two-point frequency shift method - 2P-FS), in which data from only two spatial locations are utilized to estimate attenuation. However, limitations exist in terms of optimum selection of these two points, which is a concern for achieving accuracy in SW attenuation computation.

In the current study, we implemented state-of-the-art SW attenuation methods (FS, 2P-FS, and AMUSE), and revisited our original implementation of FS (named R-FS) by making the following contributions [37]: first, the assumption of a constant shape parameter for all lateral locations was dropped, as also proposed in [29]; and second, an adaptive random sample consensus (A-RANSAC) algorithm [183] was developed to estimate the slope of the varying rate parameter with distance of the gamma distribution. The advantage of these modifications is that instead of selecting only two spatial points in an ROI as for the 2P-FS method, the proposed approach can consider multiple spatial locations to award more accuracy.

4.4 Methods

4.4.1 Frequency shift (FS) algorithm

The FS method [157] is briefly reviewed here. Assuming that the SW field amplitude spectrum at location x_0 is $S(f)$, then after a distance Δx away from this location, i.e. at $x_1 = x_0 + \Delta x$, the amplitude spectrum can be written as:

$$|R(f)| = G(f, x_1) \times H(f, \Delta x) \times |S(f)|, \qquad (4.1)$$

where $G(f, x_1)$ represents geometrical diffraction effects, and $H(f, \Delta x)$ viscous attenuation of the SW amplitude. The geometrical spreading can be nullified by assuming that $G(f, x_1)$ is independent of the SW frequency. By considering a linear relation with frequency of the SW attenuation, $H(f, \Delta x)$ becomes:

$$H(f, \Delta x) = \exp(-\alpha_0 \times f \times \Delta x), \qquad (4.2)$$

where α_0 , is the linear attenuation coefficient. In Equation 4.1, the SW amplitude spectrum is described by a gamma distribution, as validated in [27]. It can be expressed as:

$$|S(f)| \propto A f^{k_0 - 1} e^{-f\beta_0}, \qquad (4.3)$$

where A is the amplitude parameter of the gamma distribution, k_0 is the shape parameter that controls the symmetry of the distribution, and β_0 is the rate parameter. From Equations (4.1)-(4.3), the SW amplitude spectrum at location x_1 becomes:

$$|R(f)| \propto A f^{k_0 - 1} e^{-f(\beta_0 + \alpha_0 \Delta x)}. \qquad (4.4)$$

Here, the linear relation $\beta(x) = (\beta_0 + \alpha_0 \Delta x)$ corresponds to the rate parameter computed on a distance Δx. The parameter α_0 is the slope of the varying rate parameter. As described next, a three parameter nonlinear least-square optimization was performed at each lateral location in the x direction to estimate the amplitude, shape, and rate parameters of the gamma distribution in Equation 4.4:

$$[A, k_0, \beta(\Delta x)] = arg \min_{A, k_0, \beta} \left|\left|R(f, x_1) - R(f, x_0)\right|\right|_2^2. \qquad (4.5)$$

After estimating $\beta(\Delta x) = (\beta_0 + \alpha_0 \Delta x)$ for each location between x_0 and $x_0 + \Delta x$, a linear fit was performed between the rate parameter and spatial locations. The slope of this line is the SW attenuation coefficient (α_0).

4.4.2 Two-point frequency shift (2P-FS) algorithm

This method [29] corresponds to an improved version of FS [157], for which only two spatial locations were utilized to compute SW attenuation instead of multiple lateral points over a selected lateral length. Kijanka and Urban [29] also proposed using varying shape parameters of the gamma distribution for each pair of first and second signal positions, to consider the difficulty of keeping that parameter equal for both source and attenuated amplitude spectra in all lateral positions. The main advantage of considering only two points is that it reduces the computational burden. Another advantage is that it may help avoiding noisy outliers that may exist between these two points. Computations can be performed for various first signal positions and distances between two lateral positions.

However, one weakness of the 2P-FS method is the ambiguity on how to select the two points along distance. Selection of two optimum positions can be extremely challenging in anisotropic and heterogeneous biological tissues (even if the assumption of a homogeneous isotropic tissue is considered for frequency shift methods). If the two points are not selected properly, estimated parameters of the gamma distribution (Equation 4.5) might be biased. Another concern is that selecting only two points in a lateral direction may correspond to a small sample size for performing a linear fitting and may consequently result in a lower accuracy. In the proposed study, the selection of the two points was done based on the map obtained by selecting various pairs of points laterally, and by averaging them at the focal depth.

4.4.3 Revisited frequency shift (R-FS) algorithm

In this study, we propose two modifications to the original FS method [157]. These improvements deal with the inverse problem of Equation 4.5, and aim at improving the estimation of the rate (β_0) and slope (α_0) parameters with respect to lateral distance. Firstly, a non-linear least-squares algorithm (Levenberg-Marquardt) was used to solve Equation 4.5. In Bernard et al. [157], the shape parameter (k_0) was assumed to be constant for each lateral location. However, we

have dropped this assumption, as also suggested in [29]. Once amplitude, shape and rate parameters were computed for each lateral location using Equation 4.5, linear fits were performed to estimate slopes (α) with respect to lateral distances (i.e., β versus x). Unlike the 2P-FS method where only two lateral locations were considered, the proposed modification performed computations at multiple points along the lateral direction.

Secondly, an adaptive random sample consensus algorithm was used to avoid noisy/false outliers in the estimation of the linear slope of rate parameters (β) versus lateral distance. The random sample consensus (RANSAC) algorithm is an iterative line fitting method with improved robustness to large numbers of outliers [183]. It has been previously utilized in processing ultrasound image [31, 184, 185]. For more details on the classical RANSAC implementation, readers are referred to [183].

The algorithm for the proposed method is summarized in **Figure 4.1**. We made two modifications in the implementation of RANSAC for linear fitting of rate parameters with distances of the gamma distribution model. The original RANSAC algorithm selects two points randomly and uses a preset threshold. Here, instead of selecting the two points randomly, all combinations of two points are chosen, which is convenient due to the limited number of computed rate parameters (less than 20 points based on the selected size of the ROI). Second, instead of assuming a fixed preset threshold, the threshold was automatically set based on the algorithm provided in **Figure 4.1**.

According to this algorithm, all possible pairs of points among inliers were considered. An initial threshold (Th_{new}) was obtained in the case that half of other points (excluding the pair of points selected) were within the threshold. Therefore, with this procedure, more than half of all points were considered as inliers ($N/2 + 1$, $2N$: number of points). This threshold was updated at each iteration aimed at selecting two new points, until the minimum threshold included more than half of points. Then, the line corresponding to this threshold corresponded to the searched line fitting of the adaptive RANSAC (A-RANSAC) algorithm.

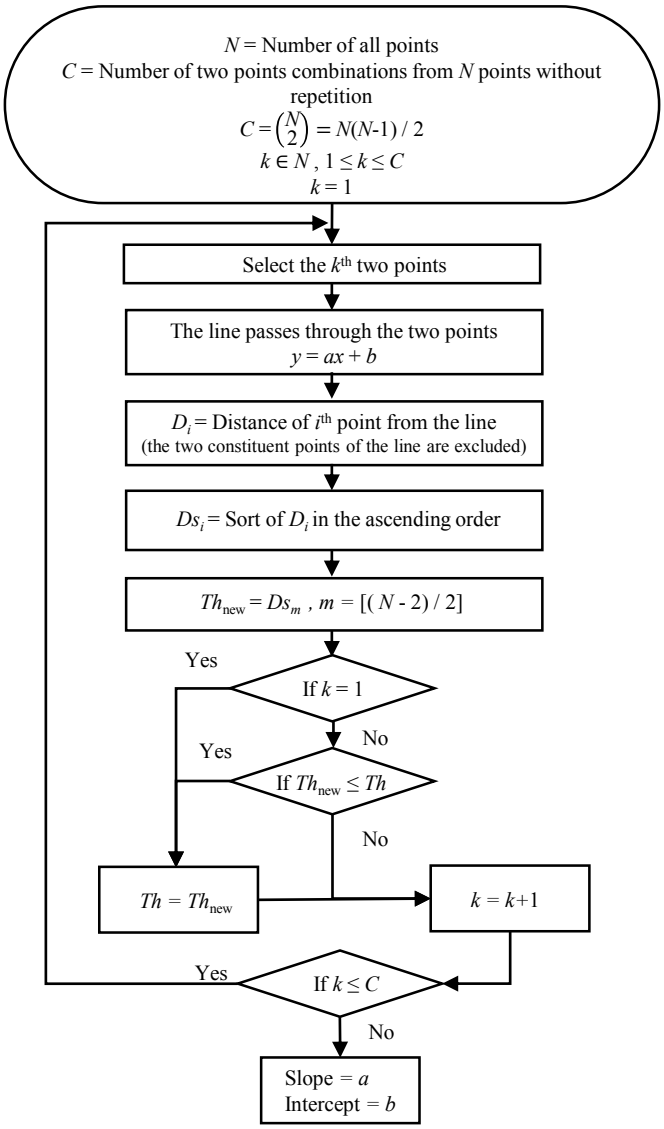

Figure 4.1 Adaptive RANSAC flowchart.

4.4.4 Attenuation measuring ultrasound shear wave elastography (AMUSE) algorithm

For comparative purpose, the AMUSE method was implemented according to [31]. As mentioned earlier, it uses a *k*-space based approach to assess the frequency dispersion of SWs. In summary, a two-dimensional Fourier transform of the SW displacement field ($u(x,t)$) is computed, where x is the distance and t is time. It is written in the *k*-space domain as $U(k,f)$, where k is the wave number and f is the frequency. For a propagating wave with a frequency

f_0 the magnitude of $U(k,f)$ has a peak at $f_0/c, f_0$ [31]. For computing the SW attenuation, the full-width-at-half-maximum (*FWHM*) is computed, and the SW attenuation (α) evaluated over a range of frequency (based on the *k*-space magnitude maxima) becomes [31]:

$$\alpha = \frac{FWHM \times \pi}{\sqrt{3}}. \qquad (4.6)$$

Thus, AMUSE offers a state-of-the-art analytical model to compute SW attenuation without much computational complexity. It provides a viscoelasticity measure but no images associated to it. This method is computationally very fast and efficient, and it was adopted as a reference method for comparative purpose [29]. However, only a mean value of the SW attenuation in an ROI can be computed using this approach.

4.4.5 Simulation model

The SW propagation in two tissue mimicking materials was simulated based on the Kelvin-Voigt (KV) rheological model using COMSOL software (version 3.5a, structural mechanics module, Palo Alto, CA, USA), as in [186]. For both media, the density was assigned to 1055 kg/m3, the shear modulus (*G*) to 3.24 kPa, and Poisson's ratio to 0.499. In the first simulation, the viscosity was set to 0.5 Pa.s and in the second it was fixed to 2 Pa.s. The total mesh size contained 16,463 domain elements, and 795 boundary elements. The SW was generated by a Gaussian force, as depicted in **Figure 4.2**, according to [187]. To mimic experimentally collected data, Gaussian random noise (MATLAB function awgn) was added to the SW velocity field at signal-to-noise ratios (SNR) of 15 dB to -5 dB. Therefore, ten noisy simulations were obtained for assessing attenuation measurement methods. Interested readers may see **supplementary material (section 4.12.1)** for numerical shear wave particle velocity motion with added noise. Even though SNR values were imposed in simulated datasets, a SNR approximation method described in **Appendix B (4.10)** was used to validate simulated and experimental conditions reported in this work.

Because the KV model was utilized in the FEM simulations, it was thus considered as the gold standard for comparison of simulations. Calculations were done based on [186] and for each frequency, an attenuation was evaluated and the slope of that attenuation was considered as the attenuation coefficient of the KV model , as it was also performed in [29].

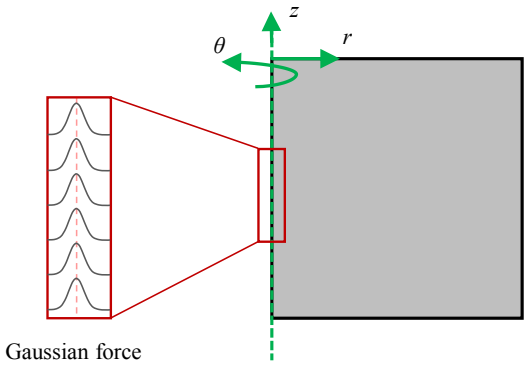

Figure 4.2 Schematic of the finite element model in COMSOL. The model is cylindrical and axisymmetric along the z-axis (green dashed line).

4.4.6 Attenuation map reconstruction

Shear wave attenuation maps were reconstructed for the three methods described in the previous section: R-FS, 2P-FS, and FS. A constant rectangular ROI was considered for all three methods (**Figure 4.3-(a)**). This ROI was selected 4 mm away from push locations, as in [27, 157]. Within this rectangular ROI, a computing window is moving in axial and lateral directions with a pre-defined overlap to construct the attenuation map. The length and width of the computing windows were 4.06 mm (13 pulse lengths) and 3.98 mm (56 depth lines), respectively. The overlaps of computing windows in both axial and lateral directions were 92%. All these parameters were set the same for all methods providing maps. In each computing window, the velocity fields were averaged in the axial direction to obtain the attenuation using R-FS, 2P-FS and FS methods. Finally, a cubic interpolation was used to increase the spatial sampling of the reconstructed map. For FS and R-FS, the attenuation was obtained based on all data points along the lateral distance in each computing window. However, 2P-FS uses only two points laterally; the distance between these two signal positions was equal to the lateral segment length of FS and R-FS. Additionally, another kind of maps was constructed on a linear ROI for simulations. The ROI was selected on the averaged velocity field along the lateral distance at the focal depth (**Figure 4.3-(b)**). In this map, the computing windows had different lengths, which could be in different positions. These maps were obtained based on combination of different lateral positions with various lengths of the computing window (**Figure 4.3-(b)**); they were made to be able to compare our results with [29].

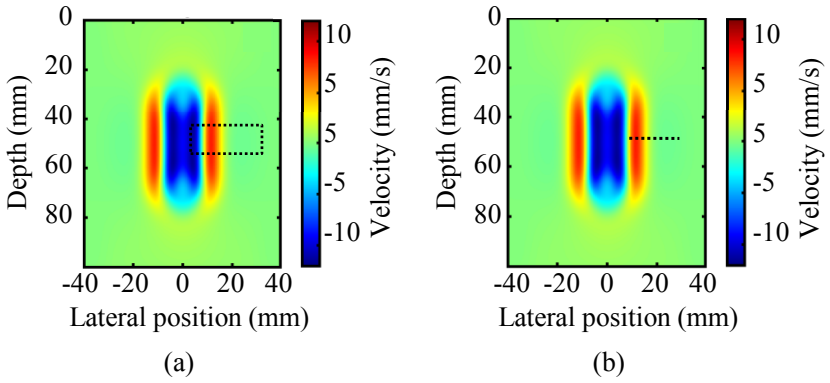

Figure 4.3 The two types of ROIs used to construct maps in this study. **(a)** A rectangular ROI is used to compute the SW attenuation over depth and lateral directions. **(b)** The second type of map is obtained by selecting various segment lengths laterally at the focal depth.

4.5 Materials

4.5.1 *In vitro* phantoms

Two homogeneous tissue mimicking viscoelastic phantoms were prepared using gelatin (type A, #G2500, Carolina Biological Supply, Burlington, NC, USA), dietary xanthan gum, and cellulose particles with a nominal diameter of 50 μm (Sigmacell type 50, #S5504, Sigma-Aldrich Chemical, St Louis, Mo, USA). The stiffness was driven by the gelatin concentration, xanthan gum was responsible for viscous loss properties, and cellulose particles produced acoustic scattering. The procedure to prepare tissue-mimicking phantoms is briefly summarized [27], all proportions are in weight by weight (w/w). For the first phantom, 5% gelatin and 0.1% xanthan gum were first mixed thoroughly in a dry powder form, and then added into distilled water at room temperature. For the second phantom, the xanthan gum proportion was 0.5%. Next, this solution was heated up to 90 °C while continuously stirring so that gelatin and xanthan gum were dissolved completely. The solution was naturally cooled down to 40 °C and at this temperature, 1.5% of cellulose powder was added to act as scatterers. The solution was then allowed to return to room temperature, and then cast into a rectangular box kept in an ice-water bath for fast and uniform gelation. Phantoms were kept in a refrigerator overnight for 16 hours at a temperature of 4 °C to

continue the gelation. The next day, samples were subsequently allowed to naturally return to room temperature (20 °C) prior to measurements.

Readers are referred to **Appendix B (4.10)** for SNR conditions of *in vitro* phantom experiments. Values reported in this appendix allowed comparing simulation, *in vitro* and *in vivo* conditions.

4.5.2 *In vivo* duck liver data

Six *in vivo* duck liver acquisitions were used for comparing the performance of FS, 2P-FS, R-FS and AMUSE methods. The protocol was approved by the animal ethical care committee of the University of Montreal Hospital Research Center. Three different ducks had undergone a force-feeding process to induce fatty liver [188]. Acquisitions were performed as part of the study conducted by Bhatt et al. [37] (12 days of force-feeding). Radiofrequency (RF) data after radiation pressure pushes were acquired before and after the force-feeding process for each animal to provide both normal and fatty duck liver datasets. See **Appendix B** for SNRs of *in vivo* data.

4.5.3 Ultrasound measurements

4.5.3.1 Data acquisition procedure

Acoustic radiation force beam sequences were implemented on research US systems (models V1 and Vantage, Verasonics Inc., Redmond, WA, USA). A linear array probe (ATL L7-4, Philips, Bothell, WA, USA) was used at a central frequency of 5 MHz to remotely generate SWs inside samples. For phantom acquisitions (V1 scanner), each sequence generated three focused pushes spaced 5 mm apart inside the sample; the first push was at a depth of 1.5 cm. The three acoustic pushes lasted 185 µs each. For *in vivo* duck liver acquisitions (Vantage scanner), five focused pushes spaced 2.5 mm apart were used, with the first push at 1 cm depth. Each push lasted 198 µs. Immediately after generating the radiation pressure, the same US transducer was used to record plane-wave compounded RF data for post-processing (100 frames at a frame-rate of 4,000 Hz for phantoms and 3,623 Hz for ducks).

4.5.3.2 Post processing

For all measurements, RF data were beamformed using a f-k migration algorithm [189]. The particle velocity field was estimated from recorded RF data using a 2D auto-correlation algorithm [190]. Apodization was done on time domain signals via a Tukey window [27], and a low pass filter (cutoff frequency of 650 Hz) was utilized to reduce noise outliers. A directional filter was applied to the computed velocity field to suppress SW reflections from sample boundaries/interfaces [191].

4.6 Results

4.6.1 Simulations

Figure 4.4 (a)-(b) presents estimated shape and rate parameters at varying lateral positions for simulations at a SNR of -5 dB, and viscosities of 0.5 and 2 Pa.s, respectively. This figure also presents, in (c) and (d), two examples of gamma distributions fitted on these simulated datasets, for two lateral distances A and B. The goodness of the gamma fits is perused by the *R*-squared (R^2) value. At both viscosities for positions A and B, R^2 varied between 0.92 and 0.99.

From estimated gamma fits, the attenuation coefficient could be retrieved as the slope of rate parameters versus lateral positions. To show the performance of the proposed A-RANSAC method for linear fitting (as discussed in **Section 4.4.3**), comparisons were made with the iterative reweighted least squares regression (robustfit, MATLAB), and linear least squares (LLSQ) regression, for a SNR of -5 dB. As displayed in **Figure 4.5**, the A-RANSAC method provided superior line fittings at both viscosities.

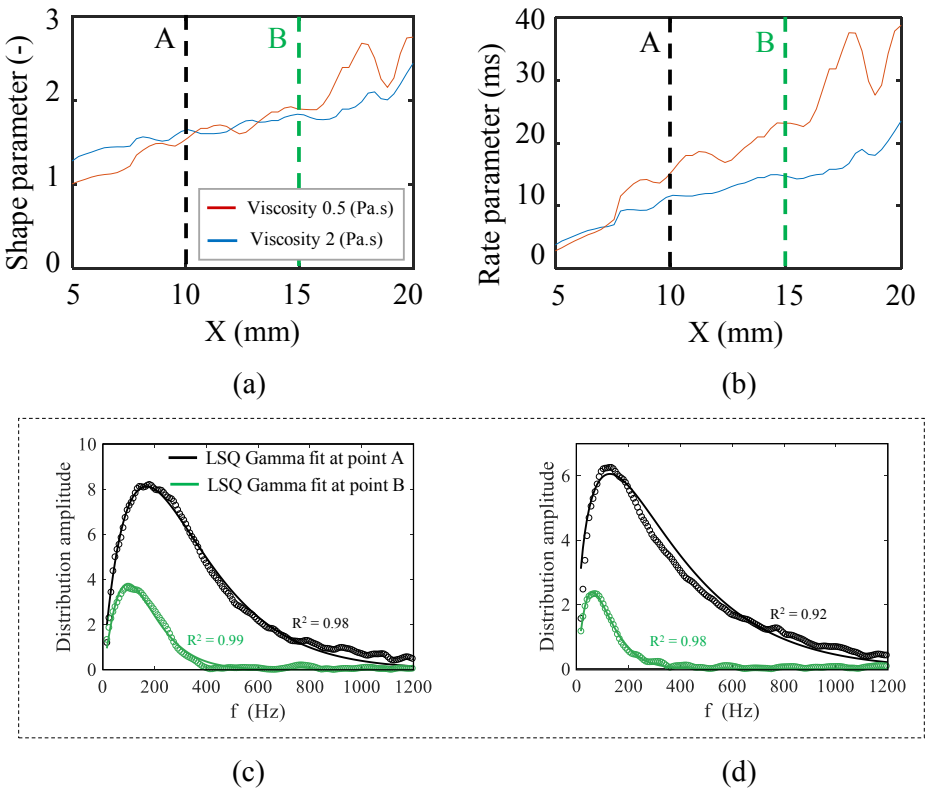

Figure 4.4 Shape (no unit) and rate (ms) parameters of the gamma distribution averaged at the focal depth, and estimated using least squares (LSQ) regressions in the case of noisy simulations (SNR = -5 dB) with viscosities of 0.5 and 2 Pa.s. In c and d, the circles and the continuous line presents simulation data spectrum and gamma fit spectrum, respectively.

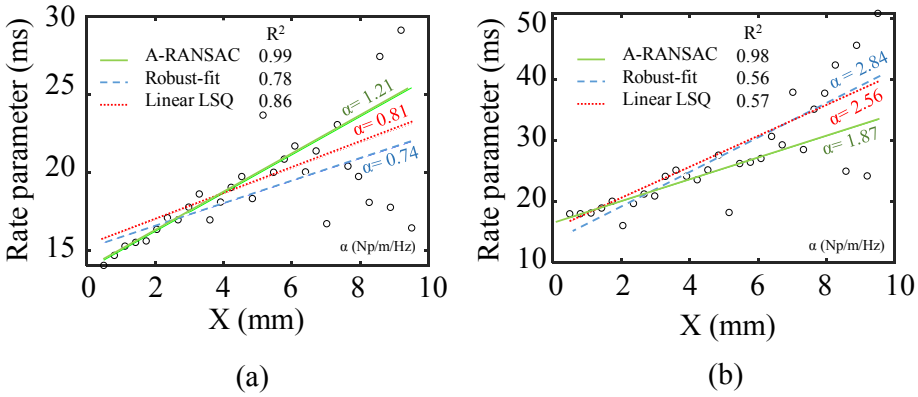

Figure 4.5 Comparison of regression performance of A-RANSAC versus robust-fit (iterative reweighted least squares regression) and linear least squares (LLSQ) regression, for simulations with viscosities of 0.5 and 2 Pa.s, and added Gaussian noise at a SNR of -5 dB.

To investigate the performance of R-FS, 2P-FS, and FS methods for attenuation estimation, Gaussian noise with SNRs from 15 dB to -5 dB was studied with numerical simulations. Reconstructed attenuation maps computed within the ROI of **Figure 4.3(a)** are presented in **Figure 4.6** and **Figure 4.7** for both viscous conditions, respectively. Boxplots of attenuation maps are compared with AMUSE in **Figure 4.8** and **Figure 4.9** for both viscosities at different SNRs. Tabulated values of mean, standard deviation, coefficient of variation (CV), and normalized root mean square error (NRMSE) with respect to ground truth (KV model) are given in **Table 4.1** for FS, 2P-FS, R-FS and AMUSE methods. Based on the statistical analysis (*i.e.*, *p*-value) of the values obtained by R-FS at different SNR levels, there were no significant differences observed between them. R-FS remained robust with the addition of noise compared with FS and 2P-FS. Negative biases are also noticed for FS. Expected homogeneous attenuation maps are preserved when adding noise for R-FS at both viscosities, whereas good performance is seen for 2P-FS at SNR > -5 dB. Quantitatively, AMUSE performed well and gave attenuation values close to the ground truth. Among image reconstruction methods, the proposed R-FS gave lowest biases, CVs, and NRMSEs compared with the KV model.

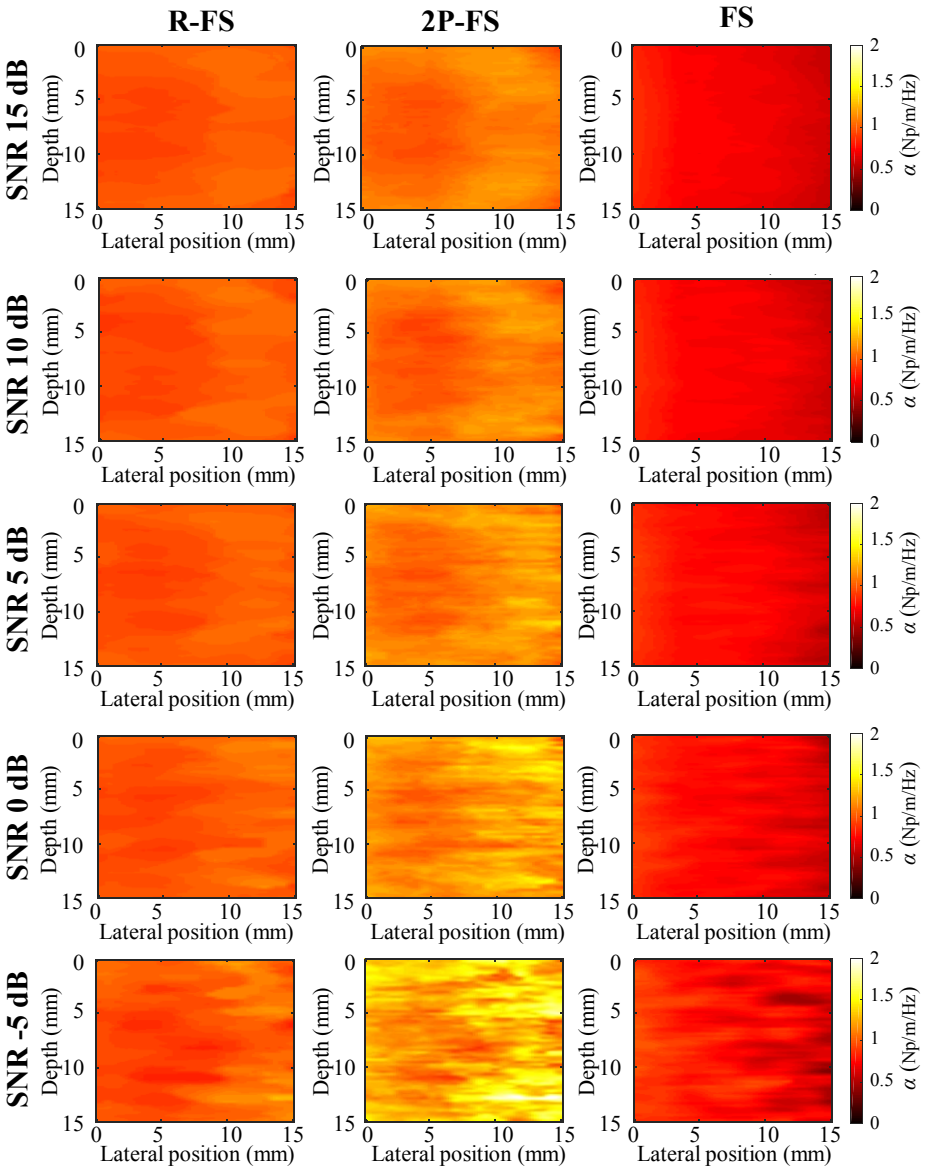

Figure 4.6 Attenuation maps reconstructed for numerically simulated data with added noise (SNR of 15 to -5 dB) at a viscosity of 0.5 Pa.s for R-FS, 2P-FS, and FS imaging methods.

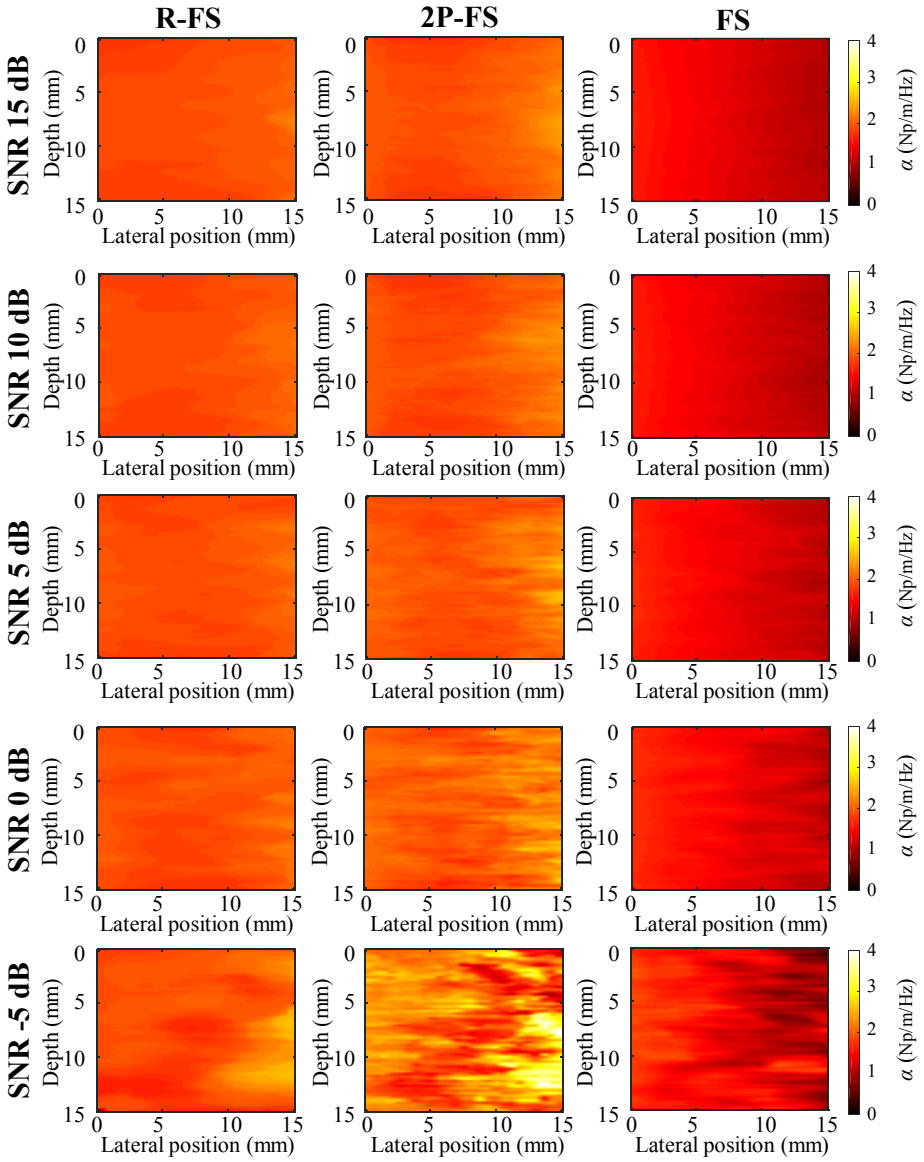

Figure 4.7 Attenuation maps reconstructed for numerically simulated data with added noise (SNR of 15 to -5 dB) at a viscosity of 2 Pa.s for R-FS, 2P-FS, and FS imaging methods.

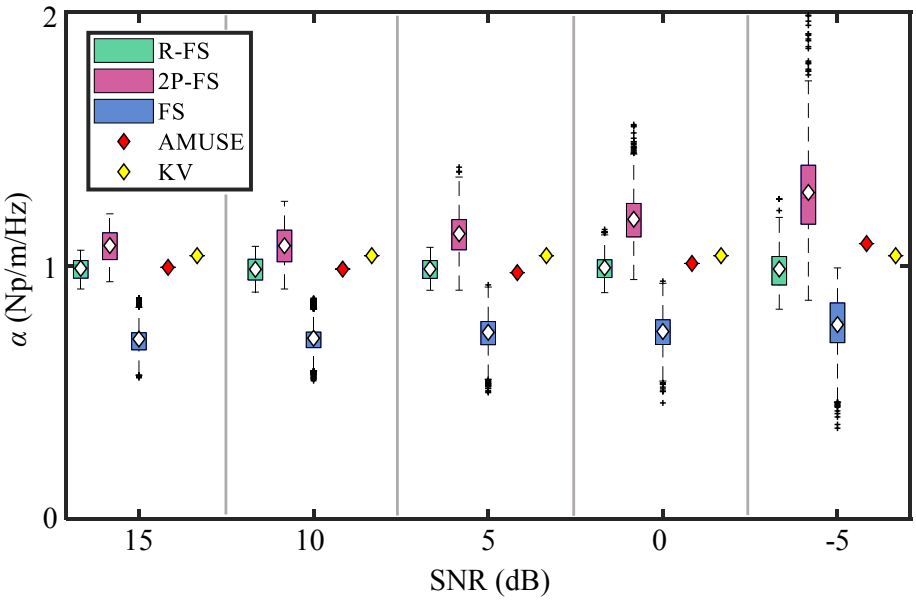

Figure 4.8 Attenuation coefficients computed with R-FS, 2P-FS, FS, AMUSE, and KV ground truth methods for noisy simulations (SNR of 15 to -5 dB) at a viscosity of 0.5 Pa.s.

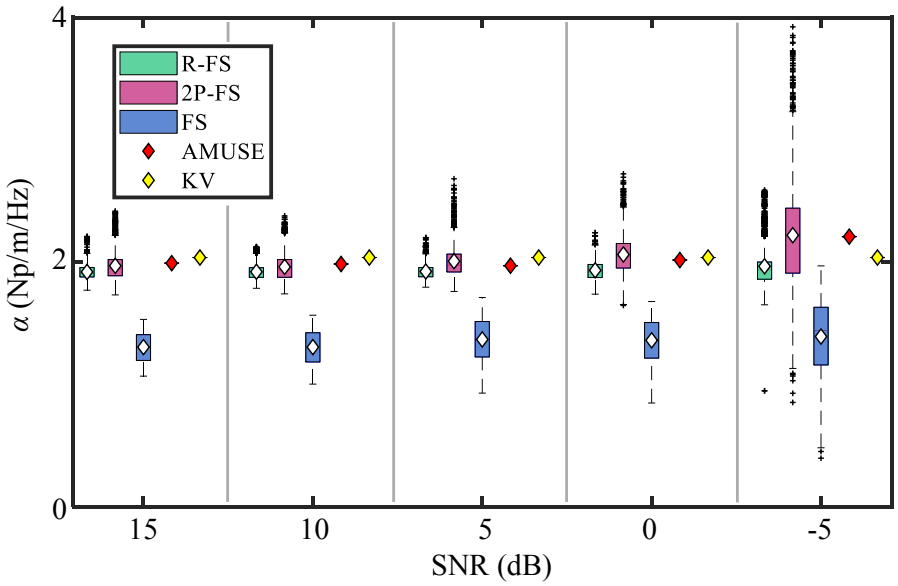

Figure 4.9 Attenuation coefficients computed with R-FS, 2P-FS, FS, AMUSE, and KV ground truth methods for noisy simulations (SNR of 15 to -5 dB) at a viscosity of 2 Pa.s.

Table 4.1 Mean (Np/m/Hz), standard deviation (SD), coefficient of variation (CV), and normalized root mean square error (NRMSE) of computed attenuation coefficients on numerically simulated data with two viscosities and different signal-to-noise ratios (SNR).

			SNR (dB)				
			15	**10**	**5**	**0**	**-5**
Viscosity: 0.5 Pa.s	Mean ± SD (CV, NRMSE (%))	**R-FS**	0.99 ± 0.04 (0.04,5.53)	0.99 ± 0.04 (0.04,6.16)	0.99 ± 0.04 (0.04,5.75)	0.99 ± 0.05 (0.05,6.19)	0.99 ± 0.08 (0.08,8.62)
		2P-FS	1.08 ± 0.06 (0.06,7.90)	1.08 ± 0.08 (0.07,8.69)	1.13 ± 0.08 (0.07,11.96)	1.18 ± 0.10 (0.09,17.82)	1.29 ± 0.17 (0.13,30.21)
		FS	0.71 ± 0.07 (0.1,31.71)	0.71 ± 0.07 (0.09,31.35)	0.74 ± 0.08 (0.11,29.48)	0.74 ± 0.08 (0.11,29.19)	0.77 ± 0.11 (0.15,27.70)
		AMUSE	0.99	0.98	0.97	1.01	1.09
		KV	1.03	1.03	1.03	1.03	1.03
Viscosity: 2 Pa.s	Mean ± SD (CV, NRMSE (%))	**R-FS**	1.92 ± 0.06 (0.03,6.59)	1.92 ± 0.07 (0.03,6.58)	1.93 ± 0.06 (0.03,6.45)	1.94 ± 0.08 (0.04,6.46)	1.97 ± 0.19 (0.10 ,10.09)
		2P-FS	1.97 ± 0.12 (0.06,6.78)	1.96 ± 0.12 (0.06,7.05)	2.01 ± 0.13 (0.06,6.54)	2.06 ± 0.16 (0.08,8.05)	2.22 ± 0.47 (0.21,24.67)
		FS	1.31 ± 0.12 (0.1,36.44)	1.31 ± 0.14 (0.11,36.61)	1.37 ± 0.18 (0.13,34.02)	1.36 ± 0.18 (0.13,34.33)	1.39 ± 0.31 (0.23,35.24)
		AMUSE	1.99	1.98	1.97	2.02	2.21
		KV	2.04	2.04	2.04	2.04	2.04

Another performance assessment was done by considering the ROI of **Figure 4.3(b)** to be in line with the evaluation strategy of the 2P-FS method in [29]. Numerical simulations with same viscosities as above and a SNR of -5 dB were used for results in **Figure 4.10**. As mentioned earlier, 2P-FS considers only two spatial points in the lateral direction, whereas FS and R-FS can consider multiple spatial locations to improve accuracy. The relation between attenuation and frequency obtained with AMUSE at both viscosities is displayed in **Figure 4.11**. The slope of solid lines corresponds to attenuation coefficients given by this method at the focal depth of the radiation pressure push (1.10 Np/m/Hz at 0.5 Pa.s, and 2.13 Np/m/Hz at 2 Pa.s). **Figure 4.12** illustrates comparative boxplots of attenuation coefficients averaged laterally at the focal depth. For other noisy simulations results with SNR of 0, 5, 10 and 15 dB, see **supplementary material (section 4.12.2)**. AMUSE provided results very close to the ground truth, and the proposed R-FS method provided the best performance in term of bias and variability.

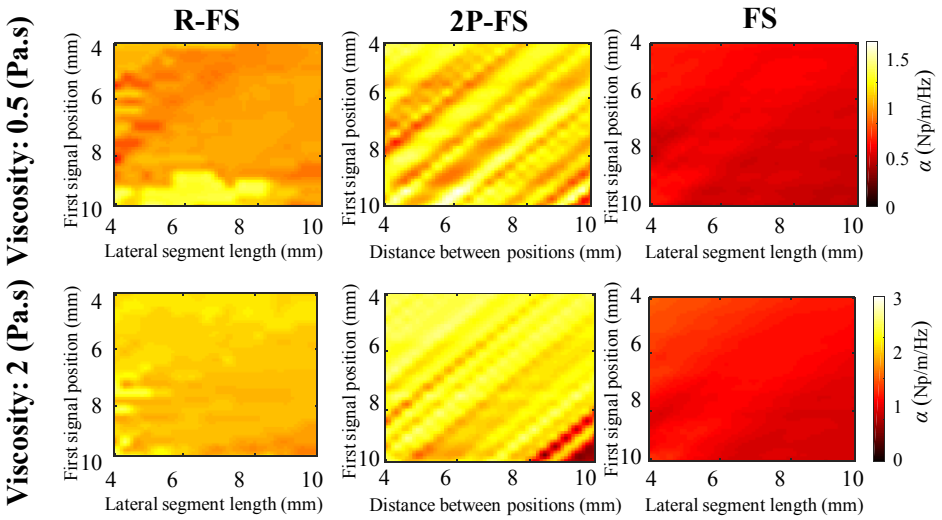

Figure 4.10 Attenuation measurements for the numerically simulated data at a SNR of -5 dB and viscosities of 0.5 and 2 Pa.s, using R-FS, 2P-FS, and FS methods for different lateral positions at the focal depth.

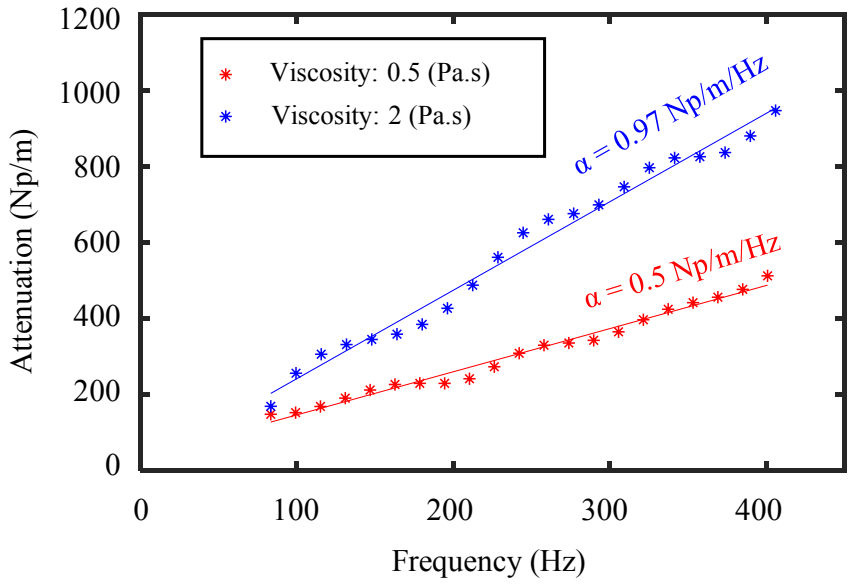

Figure 4.11 Attenuation coefficients computation for the numerically simulated data by AMUSE at a SNR of -5 dB and viscosities of 0.5 and 2 Pa.s, for lateral measurements at the focal depth.

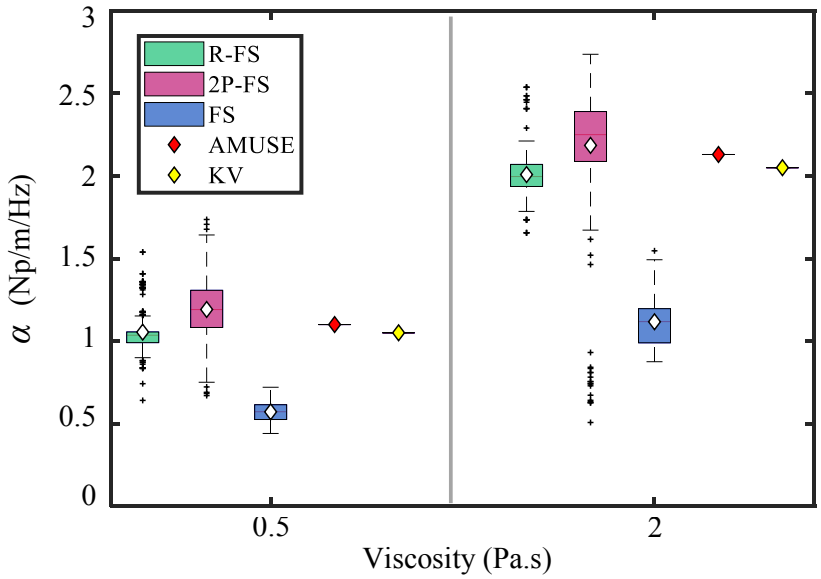

Figure 4.12 Attenuation coefficients computed with R-FS, 2P-FS, FS, AMUSE, and KV ground truth methods for the numerically simulated data at a SNR of -5 dB, and viscosities of 0.5 and 2 Pa.s.

4.6.2 *In vitro* phantoms

Figure 4.13 presents reconstructed attenuation maps for two homogeneous phantoms in a rectangular ROI, as defined in **Figure 4.3 (a)**. The phantom I was made with less xanthan gum than phantom II to have two levels of viscosity. Attenuation versus frequency plots estimated with the AMUSE method are presented in **Figure 4.14** along with their linear regressions. **Figure 4.15** presents boxplots of attenuation coefficients computed by R-FS, 2P-FS, FS, and AMUSE methods. Tabulated metrics are given in **Table 4.2**.

As observed with simulations, FS and R-FS provided quite uniform attenuation maps, as expected for these homogeneous phantoms. Quantitatively, the proposed R-FS method gave closest results to AMUSE and minimum variability.

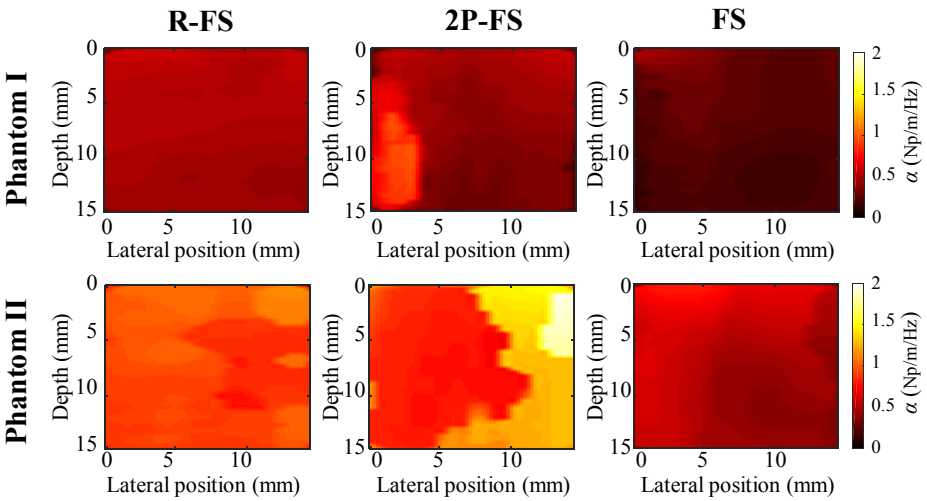

Figure 4.13 Attenuation maps of homogeneous *in vitro* viscoelastic phantoms reconstructed with R-FS, 2P-FS, and FS methods.

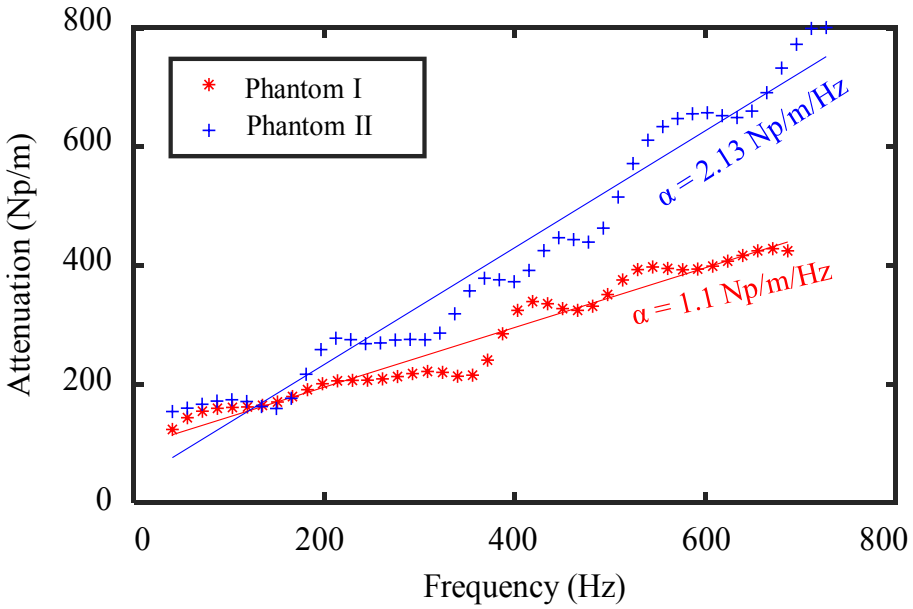

Figure 4.14 Attenuation coefficients computation with AMUSE for both homogeneous *in vitro* viscoelastic phantoms.

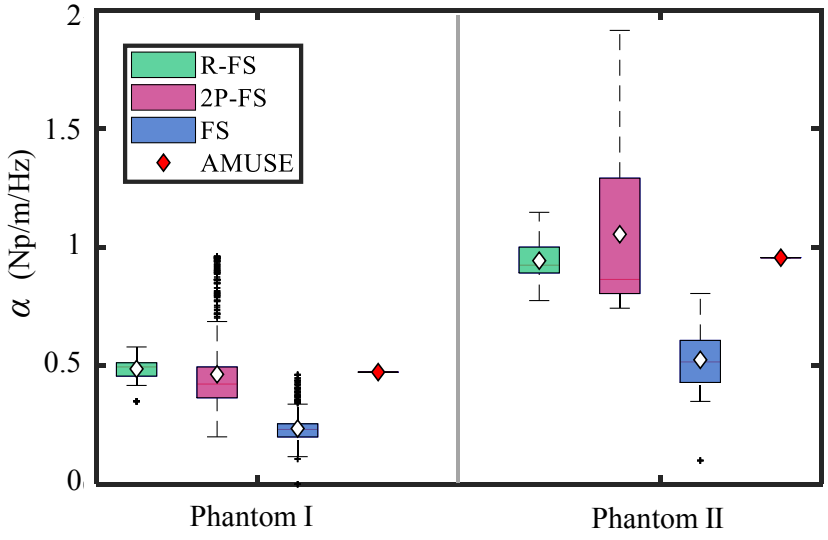

Figure 4.15 Attenuation coefficients of homogeneous *in vitro* viscoelastic phantoms computed with R-FS, 2P-FS, FS, and AMUSE methods.

Table 4.2 Mean (Np/m/Hz), standard deviation (SD), and coefficient of variation (CV) of attenuation coefficients within the ROI for both homogeneous *in vitro* viscoelastic phantoms.

		Homogeneous *in vitro* phantoms	
		I	**II**
Mean ± SD (CV)	**R-FS**	0.49 ± 0.04 (0.08)	0.94 ± 0.07 (0.07)
	2P-FS	0.46 ± 0.17 (0.37)	1.06 ± 0.31 (0.29)
	FS	0.24 ± 0.05 (0.21)	0.53 ± 0.1 (0.19)
	AMUSE	0.50	0.97

4.6.3 *In vivo* duck livers

The liver region in three ducks scanned twice was manually selected by a veterinarian. After force feeding, histology analyses in all animals revealed a steatosis grade 3, no ballooning, inflammation grade 2, and fibrosis grade 1A [37].

Figure 4.16 shows B-mode images and SW attenuation maps of duck livers before force feeding (i.e., reference state) reconstructed with R-FS, 2P-FS, and FS methods. Results after force feeding are given in **Figure 4.17**. Higher SW attenuations are observed after force feeding, and non-homogeneous displays are noticed (R-FS has lower variability). Attenuation versus frequency for AMUSE is presented in **Figure 4.18**.

Boxplots comparison of methods are given in **Figure 4.19**, and tabulated values are summarized in **Table 4.3**. Truncated ROIs displayed in

Figure 4.16 and **Figure 4.17** (dashed line rectangles) were considered to evaluate the impact of distance with respect to push locations. For both truncated and full ROIs, the proposed R-FS imaging method provided closest results to the non-imaging AMUSE method. The SDs and CVs of R-FS were less than other methods for both ROIs (full and truncated). Based on **Table 4.3**, SDs and CVs of all three methods providing attenuation maps were lower in truncated ROIs versus full ROIs.

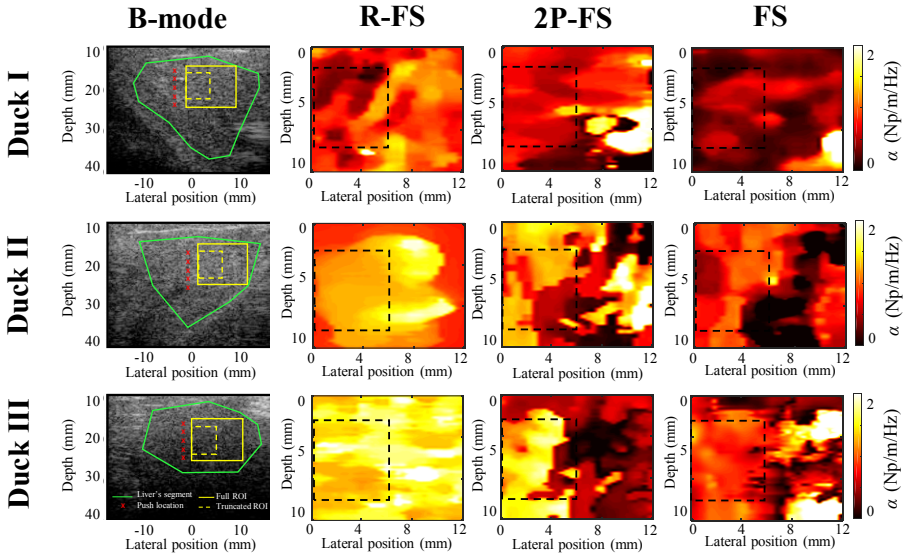

Figure 4.16 B-mode images and attenuation maps of three *in vivo* duck livers before force feeding (reference state) assessed by R-FS, 2P-FS, and FS methods. Dashed line rectangles present the truncated ROI.

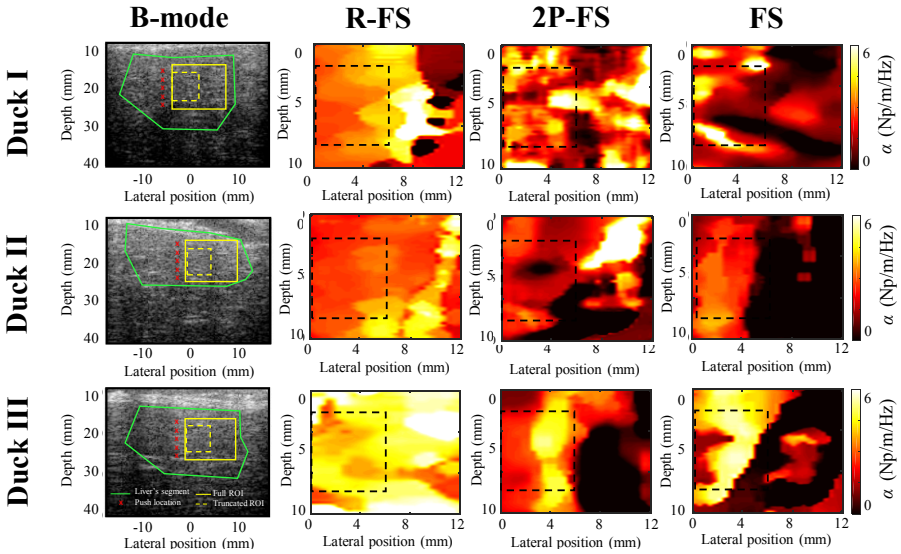

Figure 4.17 B-mode images and attenuation maps of three *in vivo* duck livers after force feeding assessed by R-FS, 2P-FS, and FS methods. Dashed line rectangles present the truncated ROI.

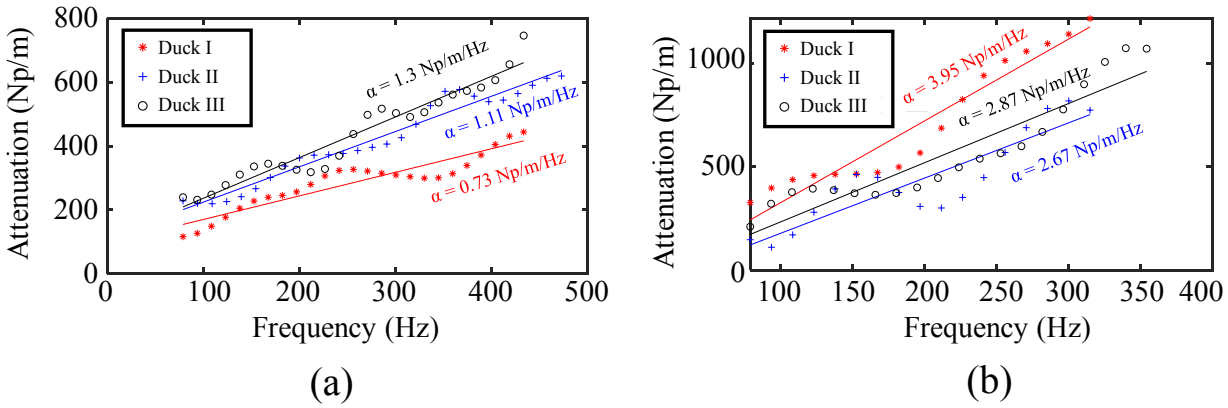

Figure 4.18 (a) Attenuation computation with AMUSE for three *in vivo* duck livers before force feeding. **(b)** Same display for three *in vivo* duck livers after force feeding.

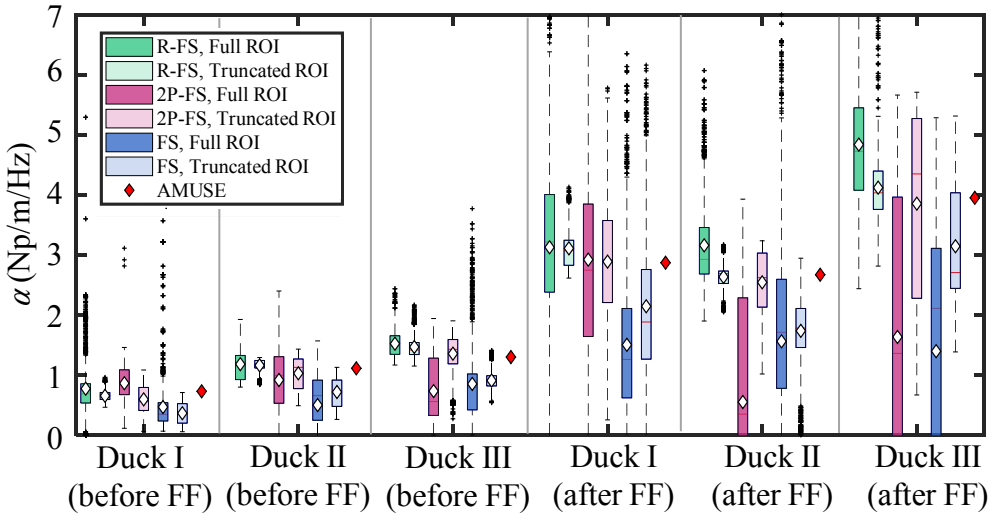

Figure 4.19 Attenuation coefficients for *in vivo* duck livers computed with R-FS, 2P-FS, FS, and AMUSE methods. Two ROIs are considered here. FF on x-axes signifies force feeding.

Table 4.3 Mean (Np/m/Hz), standard deviation (SD), and coefficient of variation (CV) of attenuation coefficients within two ROIs for three duck livers before and after force feeding (FF).

		Duck I		Duck II		Duck III	
		Full ROI	Truncated ROI	Full ROI	Truncated ROI	Full ROI	Truncated ROI
Before FF Mean ± SD (CV)	**R-FS**	0.77 ± 0.51 (0.66)	0.66 ± 0.09 (0.14)	1.18 ± 0.26 (0.22)	1.16 ± 0.11 (0.09)	1.52 ± 0.22 (0.14)	1.47 ± 0.19 (0.13)
	2P-FS	0.86 ± 0.30 (0.35)	0.60 ± 0.21 (0.35)	0.92 ± 0.55 (0.60)	1.03 ± 0.27 (0.26)	0.73 ± 0.54 (0.74)	1.36 ± 0.32 (0.24)
	FS	0.47 ± 0.48 (1.02)	0.37 ± 0.17 (0.46)	0.50 ± 0.53 (1.06)	0.72 ± 0.22 (0.31)	0.85 ± 0.61 (0.72)	0.91 ± 0.14 (0.15)
	AMUSE	0.73		1.11		1.3	
After FF Mean ± SD (CV)	**R-FS**	3.13 ± 1.73 (0.55)	3.11 ± 0.31 (0.10)	3.16 ± 0.76 (0.24)	2.63 ± 0.19 (0.07)	4.84 ± 1.13 (0.23)	4.12 ± 0.62 (0.15)
	2P-FS	2.92 ± 1.74 (0.60)	2.89 ± 1.05 (0.36)	0.55 ± 1.86 (3.38)	2.54 ± 0.51 (0.20)	1.63 ± 2.45 (1.50)	3.85 ± 1.59 (0.41)
	FS	1.50 ± 1.55 (1.03)	2.15 ± 1.35 (0.63)	1.56 ± 3.18 (2.04)	1.74 ± 0.71 (0.41)	1.40 ± 2.55 (1.82)	3.14 ± 1.02 (0.32)
	AMUSE	2.87		2.67		3.95	

4.7 Discussion

This study aimed to propose improvements to FS (and 2P-FS) method for SW attenuation computation, and to provide robust attenuation maps that could be utilized for medical diagnosis of steatotic livers. The R-FS, 2P-FS and FS are based on fitting a gamma distribution to the amplitude spectrum. This is justified by the fact that the acoustic radiation pressure field excitation might not necessarily be in the form of a symmetric Gaussian shape in lossy *in vivo* media [17]. So, the Gaussian assumption is not necessarily valid and cannot be generalized. Interested readers may consult Bernard et al. [157] for a detailed justification for choosing a gamma fit for SW data acquired in lossy media. In the current work, a Gaussian shaped force was considered to produce SWs in the simulations. See **Appendix A (section 4.9)** for a description of the relation between the Gaussian source and the approximation of the SW field with a gamma distribution.

Two main improvements were applied to the FS method; first, the shape parameter of the gamma frequency fit on the SW attenuation spectrum was not assumed constant and equal to the shape parameter of the source spectrum. This assumption is supported by **Figure 4.4**, where it can be noticed that the shape parameter varies with lateral distance. This modification of a non-constant shape parameter yielded high R-squared values of gamma fits, increasing the confidence in this model. The second modification was to use an A-RANSAC line fitting approach to further improve robustness in the presence of outliers. Outliers may appear due to tissue heterogeneity related to boundary effects, air pockets when performing gel phantom experiments, or from the measurement noise. The A-RANSAC method is able to automatically define a threshold based on each data set (according to its inliers) to reject corrupted measures. This novelty allowed superior results with the proposed method when compared with the FS or 2P-FS method. Other line fitting techniques (e.g., LLSQ and Robust-fit) are assuming that the maximum deviation of a data-point is a function of the size of the dataset; and that there is always a large enough number of good values to smooth out any outliers. The A-RANSAC algorithm was capable of rejecting such outliers; and thus, could be used in the context of this study for smoothing data that could contain a significant percentage of outliers (e.g., in the case of highly attenuating steatotic duck livers).

One of the main objectives of this work was to reconstruct an attenuation map of a ROI inside a medium for diagnostic applications. This is specifically important for investigating tissue texture that may arise due to fat deposition [27]. Most studies in elastography consider the

assumption of a homogeneous medium to compute SW parameters. The proposed study reported a comprehensive comparative analysis of R-FS, 2P-FS, and FS methods for SW attenuation map reconstructions in homogeneous but also heterogeneous (*in vivo*) situations, while considering the model's ability to produce low biases and low variances in the case of R-FS, thanks to the outlier rejection strategy adopted in this work. Clearly, R-FS was successful in obtaining attenuation maps with less biases and variances than other imaging methods. Furthermore, two additional quantitative methods, AMUSE and the KV model in the case of simulations (ground truth), were utilized to validate observed findings. Numerical phantoms are ideal for a comprehensive analysis as they can provide ground truth estimates, and simulations of noisy conditions. In the case of *in vitro* and *in vivo* datasets where ground truths were not available, the AMUSE model was considered as the reference method.

Simulation results of **Figure 4.8** and **Figure 4.9** revealed that FS and R-FS attenuation maps were smoother than 2P-FS maps in the presence of noise (especially at the SNR of -5 dB). This is because several spatial data points (compared with two points for 2P-FS) were considered in the lateral direction [29]. However, FS underestimated attenuation coefficients due to its assumption of a constant shape parameter at any location [157]. The proposed R-FS model overcame limitations of other imaging methods, and thus provided robust estimation of the attenuation coefficient. This was validated by comparing results to KV and AMUSE estimates. The ROI selection was consistent among methods in this study to obtain comparative results. In our previous study with the FS model, one had to select the ROI location at different positions to minimize the impact of noisy wave fields [37, 157]. Consequently, SW attenuation values may differ at the end of the force-feeding process between studies.

Figure 4.10 and **Figure 4.11** reported a sensitivity analysis of attenuation computations over a line at the focal depth. Different first signal positions and varying lateral segments were considered for numerically simulated data at a SNR of -5 dB. These maps were provided to compare our results with similar maps reported for the 2P-FS method [29]. Our results are in line with previous statements, as R-FS had less variation and closer mean values to the ground truth, especially in the case of noisy datasets.

In vitro phantom and *in vivo* duck liver datasets confirmed predictions made using simulations. Indeed, the R-FS method outperformed other imaging methods, and provided

estimates closer to AMUSE. As displayed with fatty duck liver datasets, selecting a ROI closer to the radiation pressure source improved SW attenuation estimates because of a higher signal-to-noise ratio attributed to the enhanced attenuation with distance [157]. For both truncated and full ROIs, the proposed R-FS algorithm again provided the best performance. The use of a varying shape parameter and the A-RANSAC line fitting allowed such improvements over FS and 2P-FS methods.

Limitations of the proposed model are that all frequency shift methods are inherently based on the assumption of locally isotropic and homogeneous media. Furthermore, it is also assumed that attenuation depends linearly on SW frequency, which may not hold for some biological tissues [59, 191-193]. Indeed, non-linear frequency dispersion behaviors have been reported for bovine *ex vivo* muscles [137], mammalian soft tissues [194], human breasts [59], and livers [195, 196]. Moreover, for fatty liver tissues at high frequencies (≥1000 Hz), SW attenuation has also been shown to display a non-linear relationship with frequency [195, 197].

Future studies should aim validating this model with *in vivo* human data, which may be more challenging especially in obese patients. The hypothesis of locally isotropic and homogeneous tissues may reveal an enhanced variability in the case of mechanical heterogeneities, such as cancer tumors within the liver parenchyma. Notice that AMUSE is also limited by the assumption of an isotropic and homogeneous tissue, and it does not provide images of SW attenuation. Future validations should thus be done to better appreciate limitations of the R-FS imaging method in the case of anisotropy and/or tissue heterogeneity. Results on *in vivo* fatty duck livers nevertheless allowed appreciating the robustness of R-FS for displaying SW attenuation heterogeneities attributed to the presence of fatty vacuoles.

4.8 Conclusion

The R-FS method for SW attenuation coefficient computation was developed based on varying gamma fitting shape and rate parameters, and by using an adaptive RANSAC line-fitting method. The proposed imaging method was tested on noisy simulation data, homogeneous phantoms, and *in vivo* duck livers without or with fat depositions. A comprehensive comparison with FS and 2P-FS methods suggested that the proposed R-FS algorithm is offering a robust approach to compute the attenuation coefficient. This imaging method also compared favorably

with the numerically simulated ground truth SW attenuation measures, and to the AMUSE algorithm. We envision that R-FS improvements may lead to accurate imaging of viscoelasticity in biological tissues, which may provide robust biomarkers of human fatty livers for diagnosis or of other liver or organ pathologies.

4.9 Appendix A

Here, the theory supporting the relation between the Gaussian source and the approximation of the SW field with a gamma distribution is presented. Using the notation from [179] in cylindrical coordinates and equation 1 of [187], the governing equation of the SW motion produced by a body force excitation can be written as:

$$\nabla^2 u_z - \frac{1}{c^2}\frac{\partial^2 u_z}{\partial t^2} = -\frac{1}{c^2} F_z g(t) , \qquad (4.A.1)$$

where ∇^2 is the Laplacian operator in cylindrical coordinates, u_z is the displacement of the SW in the *z*-direction of cylindrical coordinates (u_z is a function of both location (*r, θ, z*) and time (*t*)), *c* is the velocity of the wave, F_z is the distribution of the applied body force in the *z*-direction, and $g(t)$ is the temporal application of the force.

In the case of our simulations, we selected F_z with a Gaussian shape:

$$F_z(r) = A_0 \left(\frac{1}{2\sigma^2}\right) e^{-\left(\frac{r}{2\sigma}\right)^2}, \qquad (4.A.2)$$

where *r* is the cylindrical radius, A_0 is the force intensity, and σ^2 is half the variance of the pulse shape. Applying the constraint of initial conditions to be zero velocity and zero displacement, Equation 4.A.1 can be rewritten as:

$$\nabla^2 u_z(r,t) - \frac{1}{c^2}\frac{\partial^2 u_z(r,t)}{\partial t^2} = -\frac{1}{c^2} F_z(r) g(t). \qquad (4.A.3)$$

Assuming a viscoelastic medium according to [187] and taking the temporal Fourier transform of Equation 4.A.3 yields:

$$\nabla^2 U_z(r,\omega) - \frac{\omega^2}{\hat{c}(\omega)^2} U_z(r,\omega) = -\frac{1}{\hat{c}(\omega)^2} F_z(r) G(\omega), \qquad (4.A.4)$$

where $U_z(r,\omega)$ and $G(\omega)$ are temporal Fourier transforms of $u_z(r,t)$ and $g(t)$, respectively, ω is the angular frequency with respect to time, $\hat{c}(\omega)$ represents the SW velocity in the viscoelastic medium with shear storage $\mu_s(\omega)$ and loss $\mu_l(\omega)$ moduli, and mass density ρ. With above definitions, $\hat{c}(\omega) = \sqrt{\hat{\mu}/\rho}$ where $\hat{\mu} = \mu_s(\omega) + i\,\mu_l(\omega)$.

According to [187] and by applying the zeroth order Hankel transform (H_0) in space to Equation 4.A.4 in cylindrical coordinates yields:

$$\widehat{U}_z(\varepsilon,\omega) = \frac{\hat{k}^2}{\omega^2}\,\frac{\hat{F}_z(\varepsilon)G(\omega)}{\varepsilon^2-\hat{k}^2}. \qquad (4.A.5)$$

where $\widehat{U}_z(\varepsilon,\omega)$ is the Hankel transform of $U_z(\varepsilon,\omega)$, ε is the spatial frequency, $\hat{k}$ is the complex wave number $\hat{k} = \omega/\hat{c}(\omega)$, and $\hat{F}_z(\varepsilon)$ is the Hankel transform of $\hat{F}_z(r)$. By assuming a force as in Equation 4.A.2, and using the identity $H\left\{e^{-\frac{1}{2}a^2r^2}\right\} = \frac{1}{a^2}e^{-\frac{r^2}{2a^2}}$, then by setting $a^2 = \frac{1}{2\sigma^2}$, $\hat{F}_z(\varepsilon)$ can be computed as:

$$\hat{F}_z(\varepsilon) = A_0 e^{-\sigma^2-\varepsilon^2}. \quad (4.A.6)$$

Now, by applying the inverse Hankel transform to $\widehat{U}_z(\varepsilon,\omega)$in Equation 4.A.5, one may write $U_z(r,\omega)$ as follows:

$$U_z(r,\omega) = \frac{\hat{k}^2}{\omega^2}\int_0^\infty \frac{\hat{F}_z(\varepsilon)G(\omega)}{\varepsilon^2-\hat{k}^2}\,J_0(\varepsilon r)\varepsilon d\varepsilon, \qquad (4.A.7)$$

where J_0 is the zero-order Bessel function. One may factor out $G(\omega)$ in Equation 4.A.7, which gives:

$$U_z(r,\omega) = \frac{\hat{k}^2G(\omega)}{\omega^2}\int_0^\infty \frac{\hat{F}_z(\varepsilon)}{\varepsilon^2-\hat{k}^2}\,J_0(\varepsilon r)\varepsilon d\varepsilon. \qquad (4.A.8)$$

Using Baddour's Theorem 4 [198] for complex wave numbers along with Equation 4.A.8, one may solve for $U_z(r,\omega)$:

$$U_z(r,\omega) = -G(\omega)\frac{\hat{k}^2}{\omega^2}\,\frac{\pi i}{2}H_0^{(2)}(\hat{k}r)\hat{F}_z(\hat{k}), \qquad (4.A.9)$$

where $H_0^{(2)}$is the Hankel function of the second kind, and $\hat{k}$ is a complex number, with a negative imaginary part of the form $\hat{k} = \frac{\omega}{\tilde{c}} - i\alpha_1\omega$, where α_1 is the first order Taylor approximation of the

attenuation, and where in a dispersive medium: $\tilde{c} = c_0 + c_1\omega$. Substituting Equation 4.A.6 into Equation 4.A.9 then yields:

$$U_z(r,\omega) = -G(\omega)\frac{\hat{k}^2}{\omega^2}\, A_0 \frac{\pi i}{2} H_0{}^{(2)}\left(\hat{k}r\right) e^{-\sigma^2(\hat{k}^2)}. \qquad (4.A.10)$$

Substituting for the expression for $\hat{k}$ into Equation 4.A.10 yields:

$$U_z(r,\omega) = -G(\omega)\frac{\left(\frac{\omega}{\tilde{c}} - i\alpha_1\omega\right)^2}{\omega^2}\, A_0 \frac{\pi i}{2} H_0{}^{(2)}\left(\left(\frac{\omega}{\tilde{c}} - i\alpha_1\omega\right)r\right) e^{-\sigma^2\left(\left(\frac{\omega}{\tilde{c}} - i\alpha_1\omega\right)^2\right)}. \qquad (4.A.11)$$

Assuming a complex number of the form $z = x + iy$, where $0 < y << x$, an approximation is suggested in [199] as follows:

$$H_0{}^{(2)}(x - iy) \cong e^{-y} H_0{}^{(2)}(x). \qquad (4.A.12)$$

Now, by assuming $0 < \alpha_1 << \frac{1}{\tilde{c}}$ and considering Equations 4.A.11 and 4.A.12, one obtains the approximation:

$$U_z(r,\omega) \cong -G(\omega)\left(\frac{1}{\tilde{c}}\right)^2 A_0 \frac{\pi i}{2} e^{-\alpha_1\omega r} H_0{}^{(2)}\left(\frac{\omega}{\tilde{c}}r\right) e^{-\sigma^2\left(\frac{\omega}{\tilde{c}}\right)^2}. \quad (4.A.13)$$

By inserting the assumption for a dispersive medium, $U_z(r,\omega)$ can be expressed as follows:

$$U_z(r,\omega) \cong -G(\omega)\left(\frac{1}{c_0 + c_1\omega}\right)^2 A_0 \frac{\pi i}{2} e^{-\alpha_1\omega r} H_0{}^{(2)}\left(\frac{\omega}{c_0 + c_1\omega}r\right) e^{-\sigma^2\left(\frac{\omega}{c_0 + c_1\omega}\right)^2}, \quad (4.A.14)$$

and by considering a small dispersion ($c_1 \approx 0$) for the sake of simplicity, one reaches:

$$U_z(r,\omega) \cong -G(\omega)\left(\frac{1}{c_0}\right)^2 A_0 \frac{\pi i}{2} e^{-\alpha_1\omega r} H_0{}^{(2)}\left(\frac{\omega}{c_0}r\right) e^{-\sigma^2\left(\frac{\omega}{c_0}\right)^2}. \quad (4.A.15)$$

One may then write $V_z(r,\omega) = i\omega U_z(r,\omega)$ as follows:

$$V_z(r,\omega) \cong G(\omega)\left(\frac{1}{c_0}\right)^2 A_0 \frac{\pi}{2} e^{-\alpha_1\omega r} H_0{}^{(2)}\left(\frac{\omega}{c_0}r\right) e^{-\sigma^2\left(\frac{\omega}{c_0}\right)^2}. \quad (4.A.16)$$

According to equation 42 in [179], the Hankel function $H_0{}^{(2)}\left(\frac{\omega}{c_0}r\right)$ may be replaced by the approximation:

$$H_0^{(2)}\left(\frac{\omega}{c_0}r\right) \cong \sqrt{\frac{2}{\pi\left(\frac{\omega}{c_0}r\right)}}\, e^{-i\left(\frac{\omega}{c_0}r-\frac{\pi}{4}\right)}. \quad (4.A.17)$$

Therefore, one obtains the approximation:

$$V_z(r,\omega) \cong G(\omega)\left(\frac{1}{c_0}\right)^2 A_0\omega\frac{\pi}{2}e^{-\alpha_1\omega r}\sqrt{\frac{2}{\pi\left(\frac{\omega}{c_0}r\right)}}\, e^{-i\left(\frac{\omega}{c_0}r-\frac{\pi}{4}\right)}e^{-\sigma^2\left(\frac{\omega}{c_0}\right)^2}. \quad (4.A.18)$$

In our finite element simulations, following [187], $g(t)$ is a temporal rectangular pulse of the form $g(t) = rect\left(\frac{t}{\tau}-\frac{1}{2}\right)$, where $\tau = 1$ (ms), which yields:

$$G(\omega) = \frac{1}{\sqrt{\frac{2\pi}{\tau^2}}} sinc\frac{\omega}{\frac{2\pi}{\tau^2}} e^{-\frac{i}{2}\omega}. \quad (4.A.19)$$

Substituting Equation 4.A.19 into Equation 4.A.18 yields:

$$V_z(r,\omega) \cong \frac{1}{\sqrt{\frac{2\pi}{\tau^2}}} sinc\frac{\omega}{\frac{2\pi}{\tau^2}}\left(\frac{1}{c_0}\right)^2 A_0\omega\frac{\pi}{2}\sqrt{\frac{2}{\pi\left(\frac{\omega}{c_0}r\right)}} \times e^{-i\left(\left(\frac{r}{c_0}+\frac{1}{2}\right)\omega-\frac{\pi}{4}\right)}e^{-\left(\sigma^2\left(\frac{\omega}{c_0}\right)^2+\alpha_1\omega r\right)} \quad (4.A.20)$$

Equation 4.A.20 may be simplified by applying further approximations. In the range of angular frequencies $0 < \omega \leq (2\pi \times 1200)$ rad/s, by setting $\sigma = 5\times10^{-5}$ m, and $c_0 = 1.7$ m/s (based on our simulations) one may assume that $\sigma^2\left(\frac{\omega}{c_0}\right)^2 \leq \left(\frac{0.05\times2\pi\times1.2}{1.7}\right)^2 \approx 0.049$, so that $\left|e^{-\sigma^2\left(\frac{\omega}{c_0}\right)^2}-1\right| \leq 0.048$. Thus, we can neglect the factor $e^{-\sigma^2\left(\frac{\omega}{c_0}\right)^2}$ in Equation 4.A.20, with a relative error of at most 4.8%.

Figure 4.20 displays relative errors for different values of f and c_0 (based on the simulations of this work and the literature [200, 201]), which supports the approximation of $e^{-\sigma^2\left(\frac{\omega}{c_0}\right)^2} \approx 1$. Thus, we can approximate Equation 4.A.20 with:

$$V_z(r,\omega) \cong A(r,\omega)\, e^{-i\left(\left(\frac{r}{c_0}+\frac{1}{2}\right)\omega-\frac{\pi}{4}\right)}e^{-(\alpha_1\omega r)}, \quad (4.A.21)$$

where

$$A(r,\omega) \cong \frac{1}{\sqrt{\frac{2\pi}{\tau^2}}} sinc \frac{\omega}{\frac{2\pi}{\tau^2}} \left(\frac{1}{c_0}\right)^2 A_0 \omega \frac{\pi}{2} \sqrt{\frac{2}{\pi\left(\frac{\omega}{c_0} r\right)}} \quad . \qquad (4.A.22)$$

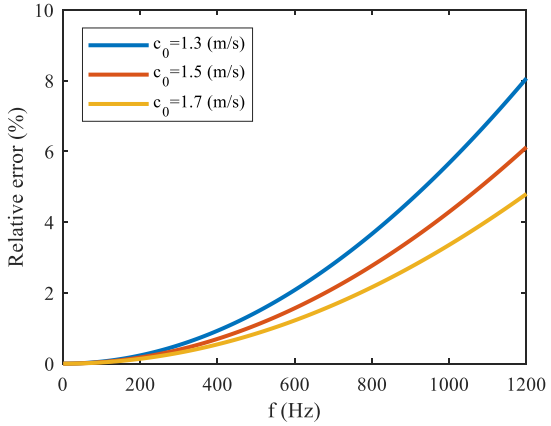

Figure 4.20 Relative error (%) as a function of f (Hz) for three values of c_0 (m/s).

Next, one may write Equation 4.A.22 as follows:

$$A(r,\omega) \cong A_1(r)\, A_2(\omega), \qquad (4.A.23)$$

where $A_1(r) \cong \frac{1}{\sqrt{r}} \frac{1}{\sqrt{\frac{2\pi}{\tau^2}}} \left(\frac{1}{c_0}\right)^2 A_0 \sqrt{\frac{\pi c_0}{2}}$, and $A_2(\omega) \cong sinc \frac{\omega}{\frac{2\pi}{\tau^2}} \sqrt{\omega}$. Equation 4.A.23 simplifies to:

$$A(r,\omega) \cong A_1(r)\, \omega^{n-1}, \qquad (4.A.24)$$

where the exponent n is around 1.5. This value might be slightly lower or higher due to the oscillatory property of the sinc function and the approximations used to derive the equations.

Using the above approximations, Equation 4.A.21 can be simplified in the form of a gamma distribution (up to a constant factor); therefore, the amplitude spectrum can be expressed as follows:

$$|S(r,\omega)| \propto A(r)\, \omega^{n-1} e^{-\beta(r)\omega}, \qquad (4.A.25)$$

where $\beta(r) = \alpha_1 r$.

Furthermore, as an example of an excitation's shape other than the Gaussian one, Parker and Baddour [179] derived, under the assumption of a "bell shape" beam (equation 33 in [179]) in

a dispersive medium together with the other assumptions provided in [179], that the particle velocity in the axial (z) direction can be expressed as follows:

$$V_z(r,\omega) \cong A_0 \frac{\pi}{2} \omega {H_0}^{(2)} \left(\frac{\omega}{c_0} r - i\alpha_1 \omega r\right) \frac{e^{-a\left(\frac{\omega}{c_0}\right)}}{\frac{\omega}{c_0}}, \qquad (4.A.26)$$

where a is a beamwidth parameter. According to Equation 4.A.12 and Equation 4.A.17, one may recast Equation 4.A.26 as follows:

$$V_z(r,\omega) \cong A_0 \frac{\pi}{2} \omega e^{-(\alpha_1 \omega r)} \sqrt{\frac{2}{\pi\left(\frac{\omega}{c_0} r\right)}} e^{-i\left(\frac{\omega r}{c_0} - \frac{\pi}{4}\right)} \frac{e^{-a\left(\frac{\omega}{c_0}\right)}}{\frac{\omega}{c_0}}. \qquad (4.A.27)$$

It follows that the amplitude spectrum can be expressed in the form of a gamma distribution, up to a constant of proportionality:

$$|S(r,\omega)| \propto A(r)\, \omega^{n-1} e^{-\beta(r)\omega}, \qquad (4.A.28)$$

upon setting n=0.5, $A(r) = A_0\sqrt{\frac{\pi {c_0}^3}{2r}}$, and $\beta(r) = \frac{a}{c_0} + \alpha_1 r$.

Altogether, whether one adopts a Gaussian shape (with sufficiently small σ) or a modified bell shape according to equation 33 in [179], then one obtains a gamma distribution within reasonable approximation. Based on the above arguments, we think that our assumption is quite reasonable to fit the SW amplitude spectrum with a gamma distribution (up to a constant factor). As an alternative approach for SW motion with localized excitation force [180], the equation of motion can be differentiated into inside and outside a maximum source radius (R). By neglecting the force for outside the R, the equation of motion could be written as equation 27 in [180] which is in agree with [179]. Using the same approach in this appendix, one can reach to the gamma distribution for SW motion.

4.10 Appendix B

The SNR for simulations, *in vitro* and *in vivo* experiments were estimated using the following equation inspired from [202]:

$$SNR = \frac{\mu^2}{MSE} \; and \; MSE = E[\left(d_e - d_g\right)^2] \qquad (4.B.1)$$

where μ is the mean displacement value at a specific axial location, MSE is the mean square error, d_e is the estimated displacement value, and d_g is the "predicted" ground truth value. For experimental data, d_g is unknown, so we have assumed that it is equal to the mean value of all axial locations within the ROI, which is a common assumption in the literature [203]. Such an approach decreases the variance but has little impact on the bias. A median filter was also applied on the mean value of all axial locations to further reduce the variance of the estimated mean and get closer to a ground truth. The same approach was done for both simulation and experimental data, even if the true SNR was known with simulations. The objective here was to verify if the estimated SNR with Equation (4.B.1) would be close to the imposed one obtained by adding noise on simulated data, which would validate *in vitro* and *in vivo* computations. All SNR estimations are provided in **Table 4.4**. For SNR approximations versus time figures, please see **supplementary material (section 4.12.3)**.

Table 4.4 Estimated SNRs for simulations, *in vitro* and *in vivo* experiments. SD, standard deviation; FF, force feeding.

Simulation viscosity 0.5 Pa·s		Simulation viscosity 2 Pa·s	
Name	Estimated SNR (dB) Mean±SD	Name	Estimated SNR (dB) Mean±SD
SNR 15	11.11 ± 3.53	SNR 15	11.67 ± 3.85
SNR 10	8.72 ± 2.84	SNR 10	8.93 ± 2.92
SNR 5	4.90 ± 1.91	SNR 5	4.89 ± 1.81
SNR 0	0.08 ± 1.04	SNR 0	-0.02 ± 0.91
SNR -5	-5.27 ± 0.48	SNR -5	-5.41 ± 0.43

In vitro phantom		*In vivo* data			
Name	Estimated SNR (dB) Mean±SD		Name	Estimated SNR (dB) Mean±SD	
Phantom I	5.96 ± 3.24	Before FF	Duck I	-4.91 ± 4.48	
Phantom II	1.41 ± 4.17		Duck II	9.87 ± 4.24	
			Duck III	-6.55 ± 2.56	
		After FF	Duck I	8.46 ± 4.63	
			Duck II	1.62 ± 7.44	
			Duck III	-0.53 ± 3.36	

4.11 Acknowledgments

The authors thank Fernande Ouellet and Francis Laroche (farm “Rusé comme un canard”, Granby, Qc, Canada); Nathalie Vermette, veterinarian, for acquiring ultrasound recordings on living awake ducks at the farm; and Dr. Francois Destrempes for his assistance in the Appendix A of this work.

4.12 Supplementary material

4.12.1 Numerical shear wave particle velocity motion data with added white Gaussian noise

An example of a velocity field map for the noisy simulation conditions with a viscosity of 0.5 Pa.s and 2 Pa.s with a SNR of -5 dB is shown in **Figure 4.21**. In addition, the shear wave particle velocity motion for three lateral positions of 5 mm, 10 mm and 15 mm are shown in **Figure 4.21**.

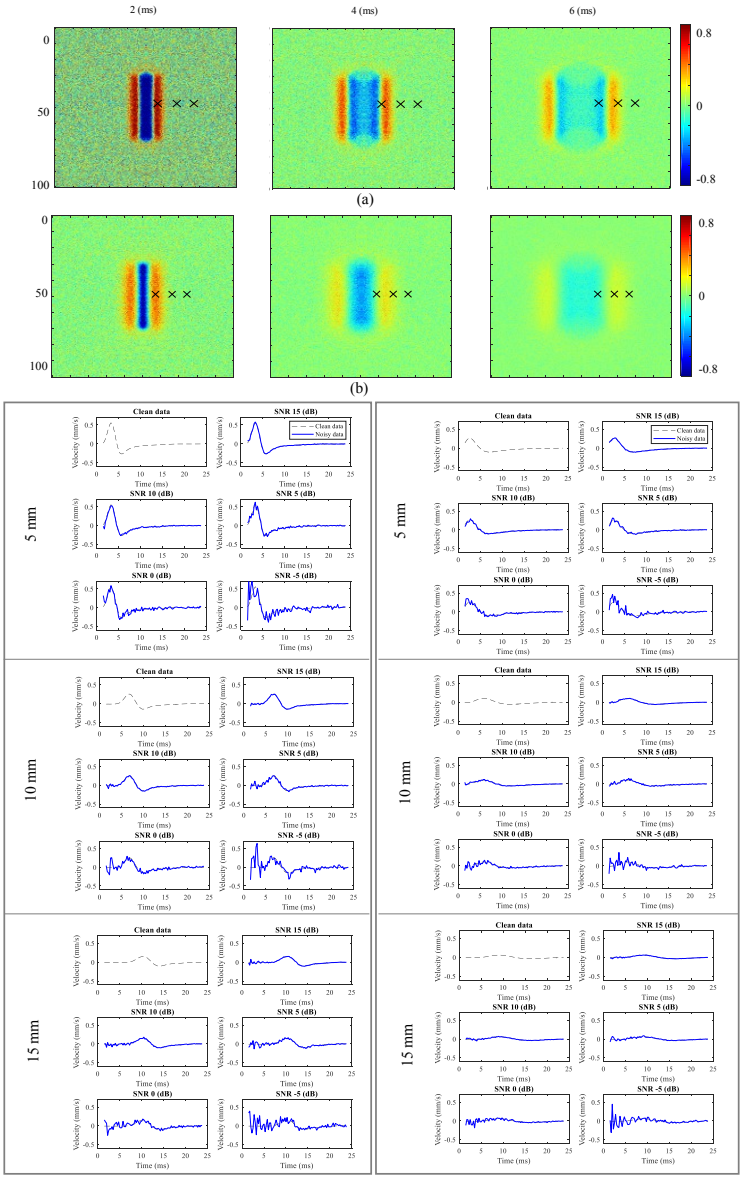

Figure 4.21 Velocity field map for a noisy simulation condition (with a SNR of -5 dB) and a viscosity of 0.5 Pa.s **(a)**, and a viscosity of 2 Pa.s **(b)**. Velocity motion versus time for noisy simulations with a viscosity of 0.5 Pa.s at three lateral positions (5 mm, 10 mm and 15 mm) for all SNR values **(c)**. Velocity motion versus time for noisy simulations with a viscosity of 2 Pa.s at three lateral positions (5 mm, 10 mm and 15 mm) for all SNR values **(d)**.

4.12.2 Attenuation maps of noisy simulations at focal depth

These attenuation maps were made to be able to compare results with the 2P-FS paper for the worst case scenario (data with -5 dB SNR). We just provided the worst-case results in the paper, as all these methods would show better performance in the case of less noise. However, we computed other cases including less noise (SNR of 0, 5, 10 and 15 dB) and presented them here in addition to case with SNR of -5 dB.

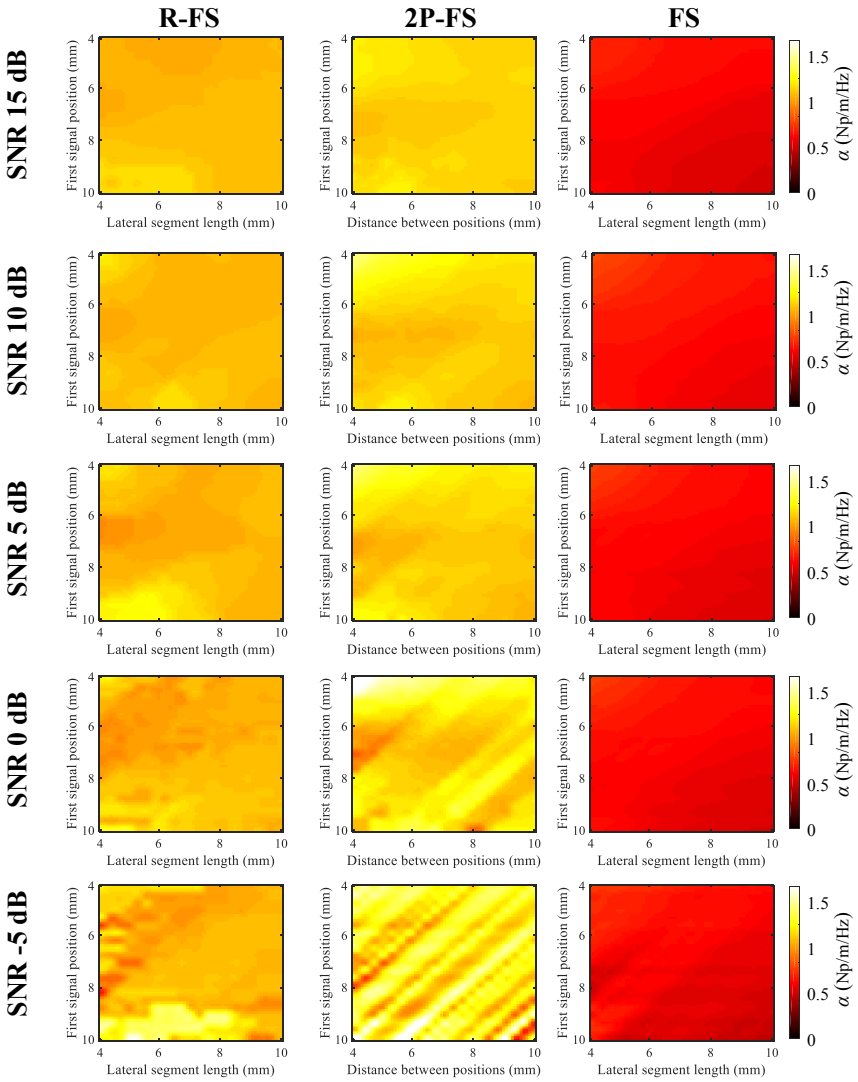

Figure 4.22 Attenuation measurements for the numerically simulated data with added noise (SNR of 15 to -5 dB) and a viscosity of 0.5 Pa.s, using R-FS, 2P-FS, and FS methods for different lateral positions at the focal depth.

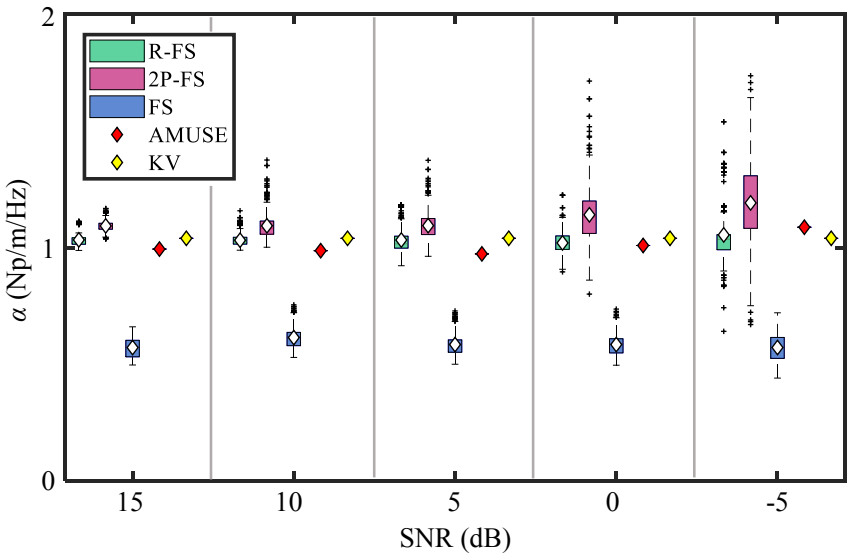

Figure 4.23 Attenuation coefficients computed with R-FS, 2P-FS, FS, AMUSE, and Kelvin-Voigt ground truth methods for noisy simulations (SNR of 15 to -5 dB) at a viscosity of 0.5 Pa.s.

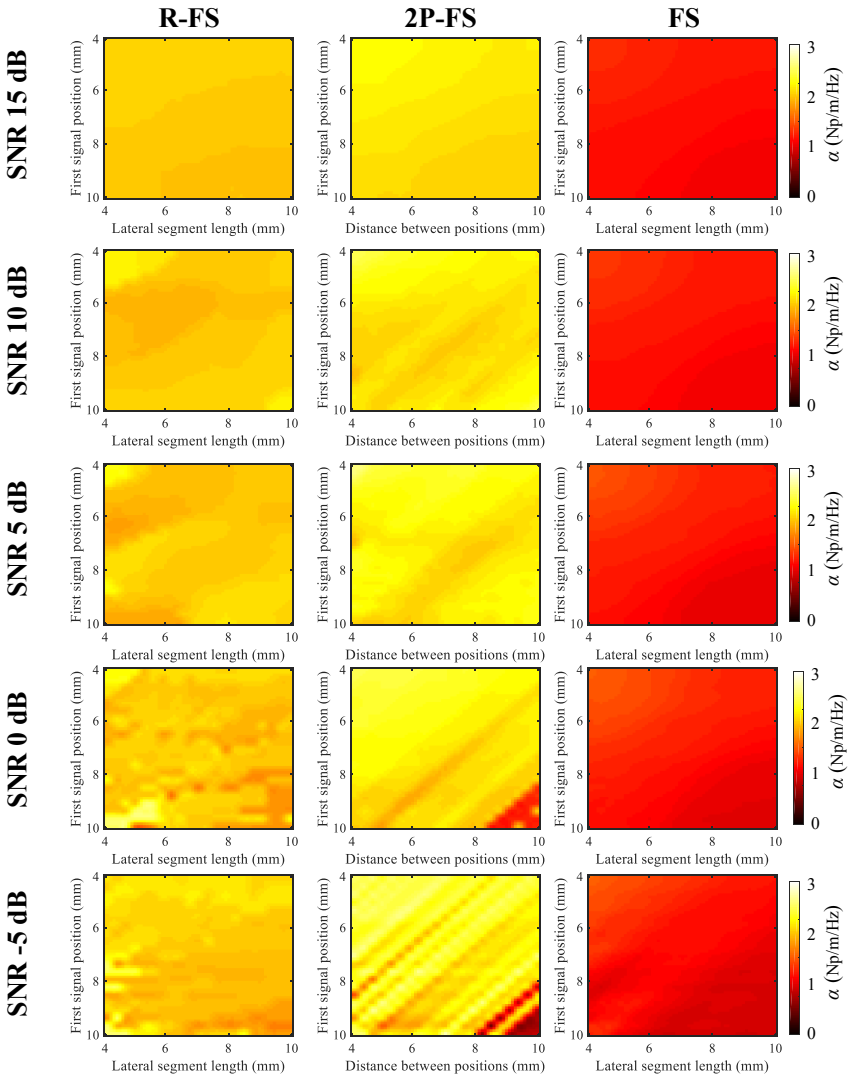

Figure 4.24 Attenuation measurements for the numerically simulated data with added noise (SNR of 15 to -5 dB) and a viscosity of 2 Pa.s, using R-FS, 2P-FS, and FS methods for different lateral positions at the focal depth.

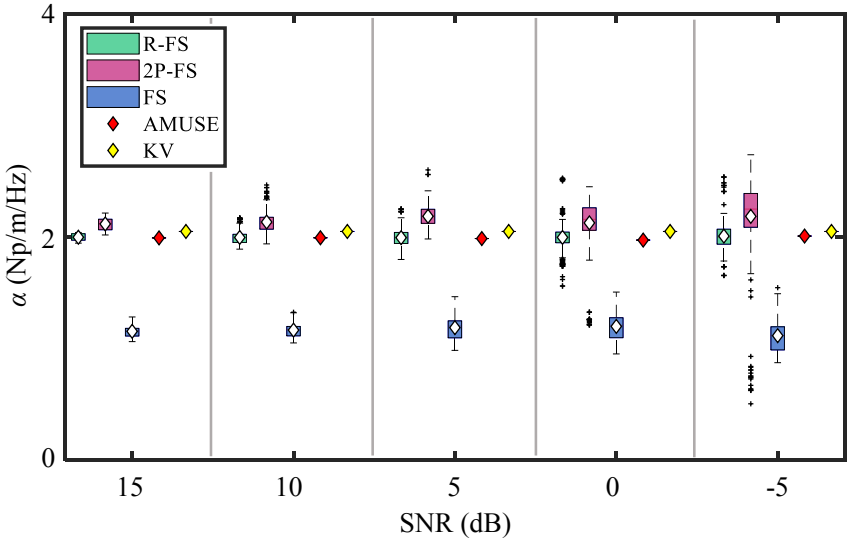

Figure 4.25 Attenuation coefficients computed with R-FS, 2P-FS, FS, AMUSE, and Kelvin-Voigt ground truth methods for noisy simulations (SNR of 15 to -5 dB) at a viscosity of 2 Pa.s.

4.12.3 SNR approximation for simulations, *in vitro*, and *in vivo* data

The SNR estimations values of simulations, *in vitro* phatoms and *in vivo* duck livers data were provided in the paper. Here, we included the figures of the SNR estimations over 25 ms.

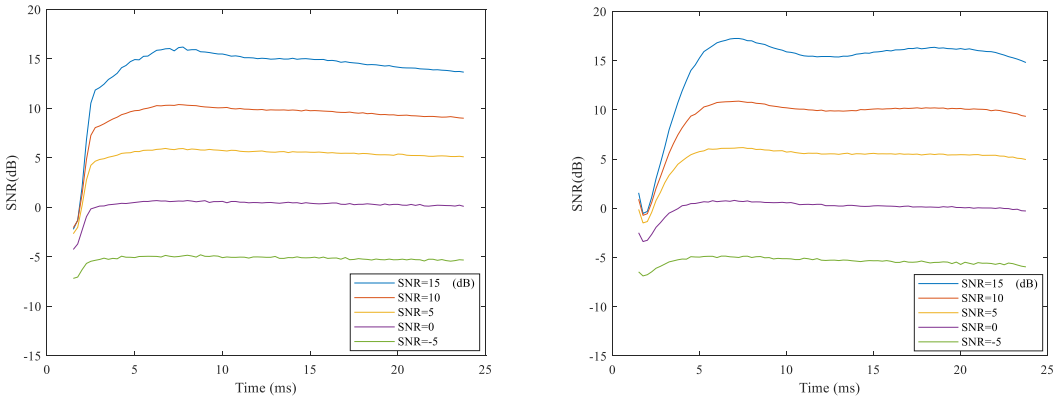

Figure 4.26 The estimated SNRs for simulation data at viscosities of 0.5 Pa.s. (left) and 2 Pa.s (right) versus time (frames).

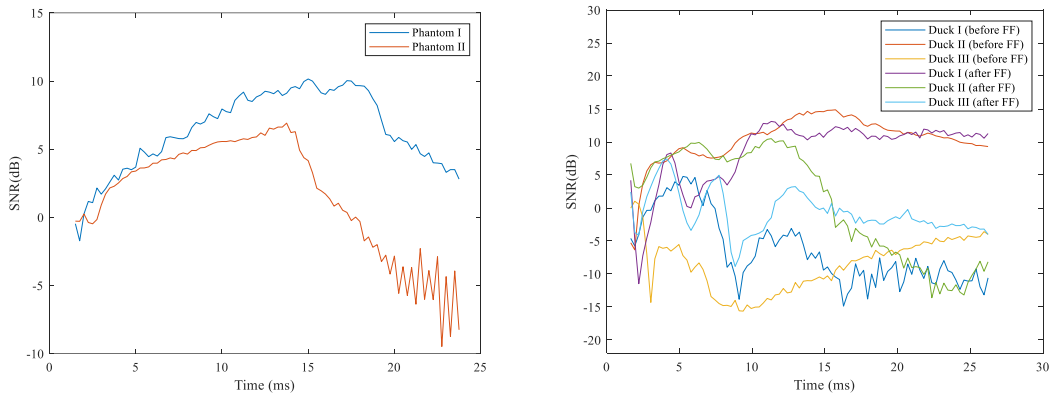

Figure 4.27 The estimated SNRs for *in vitro* data (left) and *in vivo* data (right) versus time (frames).

Chapter 5 – Ultrasound shear wave attenuation imaging for grading liver steatosis in volunteers and patients with nonalcoholic fatty liver disease: a pilot study

5.1 Introduction to manuscript

This chapter reproduces the content of a submitted article 'Ultrasound shear wave attenuation imaging for grading liver steatosis in volunteers and patients with nonalcoholic fatty liver disease: a pilot study' in the journal "Ultrasound in medicine and biology by Ladan Yazdani, Iman Rafati, Marc Gesnik, Frank Nicolet, Boris Chayer, Guillaume Gilbert, Anton Volniansky, Damien Olivié, Jeanne-Marie Giard, Giada Sebastiani, Bich N. Nguyen, An Tang, and Guy Cloutier.

The following is the order of authors for this published article and corresponding affiliations:

Ladan Yazdani[1,2], Iman Rafati[1,2], Marc Gesnik[1], Frank Nicolet[1], Boris Chayer[1], Guillaume Gilbert [3,4], Anton Volniansky[4], Damien Olivié [4], Jeanne-Marie Giard [5], Giada Sebastiani[6], Bich N. Nguyen[7], An Tang [4,8], and Guy Cloutier[1,2,4,*].

Affiliations:

[1] Laboratory of Biorheology and Medical Ultrasonics (LBUM), Centre de recherche du Centre hospitalier de l'Université de Montréal (CRCHUM), Montréal, Québec, Canada;

[2] Institute of Biomedical Engineering, Université de Montréal, Montréal, Québec, Canada;

[3] MR Clinical Science, Philips Healthcare Canada, Markham, Ontario, Canada;

[4] Department of Radiology, Radiation Oncology and Nuclear Medicine, Université de Montréal, Montréal, Québec, Canada;

[5] Department of Hepatology, Université de Montréal, Montréal, Québec, Canada;

[6] Division of Gastroenterology and Hepatology, McGill University Health Centre, Montreal, Quebec, Canada;

[7] Service of Pathology, Centre hospitalier de l'Université de Montréal (CHUM), Montréal, Québec, Canada;

[8] Laboratory of Clinical Image Processing, CRCHUM, Montréal, Québec, Canada.

[*] Corresponding author

The contributions of all authors of the published article are detailed below:

Ladan Yazdani: developed and implemented the algorithm of the R-FS method to be utilized in *in vivo* human liver, developed the algorithm for SW dispersion algorithm, beamforming, statistical analysis, drafted the manuscript and will respond to the reviewer's comments of the article.

Iman Rafati: contributed to the beamforming and statistical analysis of this work.

Marc Gesnik, Frank Nicolet, and Boris Chayer: designed experimental setup and developed algorithms for *in vivo* data acquisitions, beamforming and the electronic supplemental of this article.

Guillaume Gilbert and Anton Volniansky: performed the MRI proton density fat fraction computations and writing the paragraph regarding this.

Damien Olivié, Jeanne-Marie Giard, and Giada Sebastiani: contributed to the clinical aspects of this work.

Bich N. Nguyen: performed to the histopathological assessments of the liver biopsies.

An Tang: contributed to the interpretation of the clinical validations, results, and revision of the manuscript.

Guy Cloutier: supervised this work as the research director, contributed to the interpretation of results as the project director, corrected, and finalized the manuscript for submission and revision.

5.2 Abstract

Objective: To assess shear wave attenuation (SWA) in volunteers and patients with nonalcoholic fatty liver disease (NAFLD) and compare its diagnostic performance with shear wave dispersion (SWD), magnetic resonance imaging (MRI) proton density fat fraction (PDFF), and biopsy.

Methods: Forty participants (13 volunteers and 27 NAFLD patients) were enrolled. Ultrasound and MRI examinations were performed in all participants. Biopsy was also performed in patients. SWA was used to assess histopathology grades as potential confounders. The area under curves (AUC) of SWA, SWD, and MRI-PDFF were assessed in different steatosis grades by biopsy. Youden's thresholds of SWA were obtained for steatosis grading while using biopsy or MRI-PDFF as reference standards.

Results: Low-to-high correlations were observed for SWA with histopathology grades. Multiple linear regressions of SWA confirmed the correlation with steatosis grades (adjusted $R^2 = 0.78$, $p < 0.001$). The AUC of SWA, SWD, and MRI-PDFF were respectively 0.99, 0.93, and 0.97 for S0 vs. ≥S1 ($p > 0.05$); 0.98, 0.80, and 0.95 for ≤S1 vs. ≥S2 (only SWA was higher than SWD, $p < 0.05$); and 0.95, 0.73, and 0.93 for ≤S2 vs. S3 (both SWA and MRI-PDFF were higher than SWD, $p < 0.05$). SWA's Youden thresholds (Np/m/Hz) (sensitivity, specificity) for S0 vs. ≥S1, ≤S1 vs. ≥S2, and ≤S2 vs. S3 were 1.07 (1.00, 0.92), 1.37 (0.95, 0.95), and 1.51 (0.87, 0.92), respectively. These values were 1.17 (1.00, 0.78), 1.49 (0.89, 0.79), and 1.75 (0.86, 0.93) when considering MRI-PDFF as the reference standard.

Conclusion: In this pilot study, SWA increased with increasing steatosis grades and its diagnostic performance was higher than SWD but equivalent to MRI-PDFF.

Keywords:
Ultrasound, shear wave, elastography, attenuation, dispersion, MRI proton density fat fraction, biopsy, liver steatosis, cut-off threshold, non alcoholic fatty liver disease.

5.3 Introduction

Nonalcoholic fatty liver disease (NAFLD) is the most prevalent liver disease, particularly in Western nations [1], and it is a leading cause of liver-related morbidity and mortality [204]. This disease is associated with metabolic impairments such as obesity and type 2 diabetes mellitus [205]. NAFLD may develop to a progressive form, nonalcoholic steatohepatitis (NASH), which may lead to fibrosis, cirrhosis, and cancer. Therefore, early identification is important to prevent progression and reduce overall mortality [206].

Although liver biopsy is recognized as the historical reference standard for assessment of NAFLD and for the definite diagnosis of NASH [38, 207], there are some limitations, including sampling inaccuracy, low patient acceptance (especially for disease monitoring), and the risk of bleeding [32, 208, 209]. Therefore, the acceptability of biopsy for screening on a wide scale and for longitudinal disease monitoring is limited [210, 211].

Different imaging methods have been investigated to quantitate steatosis noninvasively [11, 12, 212]. Magnetic resonance imaging (MRI)-based techniques have been developed to measure the proton density fat fraction (PDFF), a biomarker of steatosis, with good precision and reproducibility [10, 213]. The MRI-PDFF method has been shown to detect steatosis with higher sensitivity than B-mode ultrasound (US) [10, 12, 214]. However, MRI is costly, has more limited availability, and is not available as a point-of-care device [12, 215]. MRI is also impractical for large-scale screening when considering the high prevalence of NAFLD [10, 216]. Computed tomography (CT) can be used for steatosis detection. However, except for opportunistic screening when CT is performed for another indication, it is generally not suitable as a screening method due to concerns about ionizing radiation [217].

B-mode US can be used to grade semi-quantitatively steatosis on the basis of increased backscatter (higher echogenicity), attenuation, and image clutter. However, assessment is operator dependent with moderate agreement between readers [218], the sensitivity is low for detection of mild steatosis [219], the steatosis grading ability is limited [220], and the performance drops markedly in morbidly obese patients [221]. Building on the success of shear wave elastography (SWE) [20] for quantifying and staging fibrosis [24], some US techniques have been proposed for liver fat quantification. A study explored experimentally the link between shear wave dispersion (SWD) and shear wave attenuation (SWA), which are both related to tissue viscosity [177]. Moreover, studies showed that SWD

and SWA correlate with steatosis grades [34, 37, 176, 177, 188]. Also, SWA related to the lossy nature of tissues [37, 160, 164] was found to vary with the fat content, according to preclinical fatty duck liver experiments [37]. However, few studies have assessed the feasibility and diagnostic performance of SWA in the context of NAFLD [164, 176, 177].

The purpose of this pilot study was to assess SWA in volunteers and patients with NAFLD. Secondary aims were to assess potential confounders, compare its diagnostic performance for grading steatosis with SWD and MRI-PDFF, and identify diagnostic thresholds when using either histopathology or MRI-PDFF as the reference standard.

5.4 Materials and methods

5.4.1 Design and subjects

This is a single-site, prospectively designed, cross-sectional imaging trial to evaluate the diagnostic accuracy of shear wave (SW) techniques in non-obese volunteers and patients, using histopathology as the reference standard for patients. This study was approved by the institutional review board of [institution name withheld to preserve blinding] and patient consent was obtained.

Between January 2020 and September 2022, normal volunteers and patients were enrolled to obtain a representative spectrum of disease. Non-NAFLD volunteers were included if they were adults with no risk factors for developing liver steatosis (including type 2 diabetes mellitus, alcohol consumption > 60 g of alcohol per day, lipogenic medication and body mass index (BMI) > 25 kg/m^2) and have no liver steatosis (defined as MRI-PDFF < 5%). NAFLD subjects were included if they were adults with suspected or known NAFLD or NASH, who had to undergo a liver biopsy as part of their clinical standard of care. Subjects were excluded if they had other causes of chronic liver disease or had a liver transplant. Contra-indications to MRI (such as claustrophobia or pacemaker) did not constitute an exclusion criterion since the primary endpoint was the diagnostic accuracy of SW US according to biopsy. Flow chart of patient enrollment is illustrated in **Figure 5.1.**

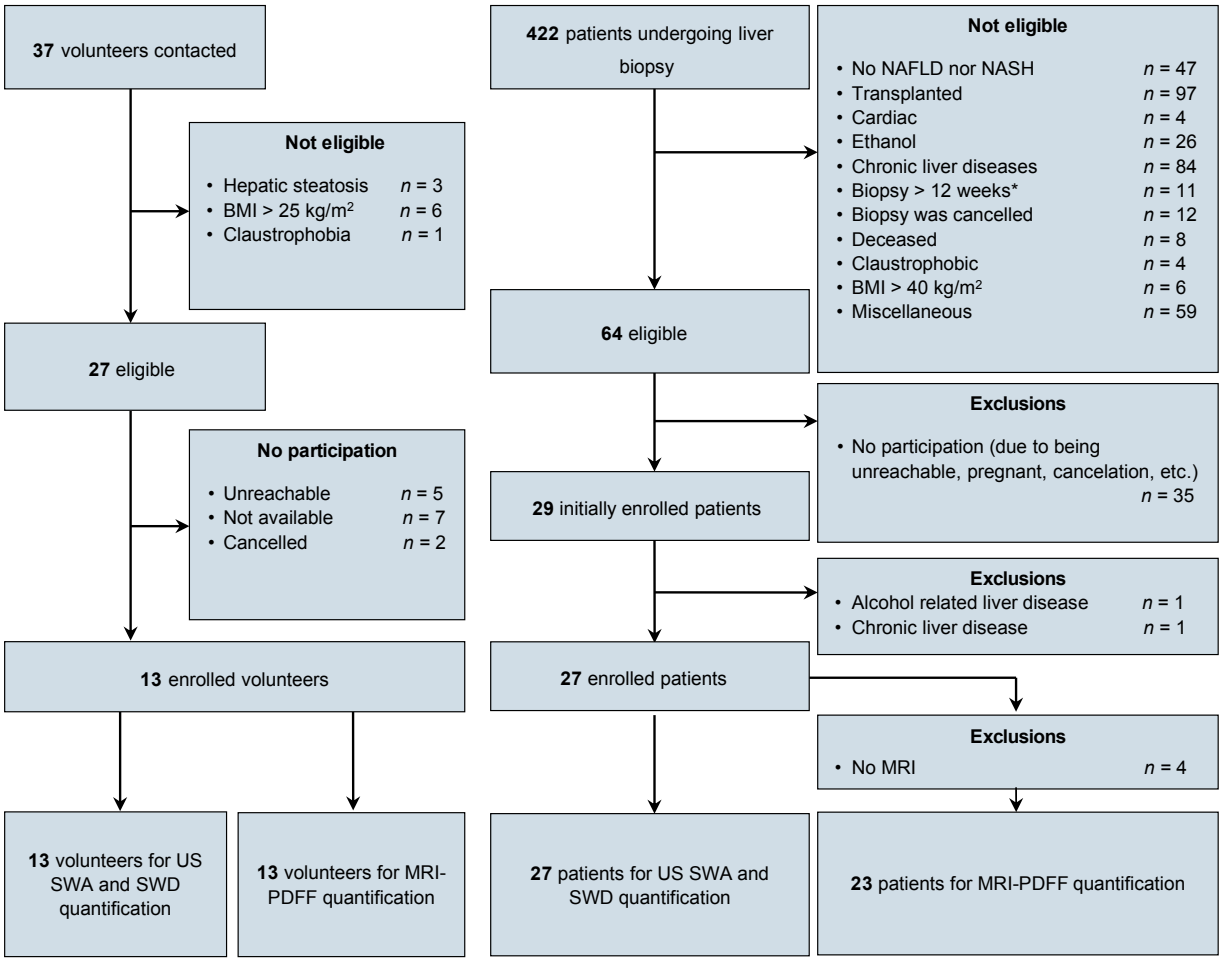

Figure 5.1 Flowchart of the participant enrollment process. US = ultrasound, SWA = shear wave attenuation, SWD = shear wave dispersion, MRI-PDFF = magnetic resonance imaging – proton density fat fraction.

5.4.2 US data acquisition

A Verasonics Vantage programmable system (Verasonics Inc, Kirkland, WA, USA) and a 128-element curved array US transducer (ATL C5-2, Philips Healthcare, Andover, MA, USA) were used to generate radiation pressure push beams and track induced displacements. Details on used US sequence, US SW generation and tracking, and intensity measurements respecting acoustic output standards are provided in **Electronic Supplement S1** (**section 5.7.1**). To visualize the SW propagation and confirm the image quality, a cine-loop reconstruction was done right after

the acquisition. Then, the beamforming was done using the f-k migration method [222] on acquired data by compounding the coherent sum of 3 angulated planes between -1 to 1°.

5.4.3 US data post-processing

A two-dimensional auto-correlation algorithm [190] applied on radiofrequency (RF) data was used to display the SW velocity field. The polar coordinates of acquired data were converted in Cartesian coordinate for further processing. The region-of-interest (ROI) for each acquisition was selected 3 mm away on the right of the last SW push line. Each ROI had a width of 1.5 cm and a length of 1.2 cm, which corresponds to the length of acoustic radiation force push line in depth direction, or smaller in the cases the segmented contour had a smaller size due to high noise. All processing was done in MATLAB (Version 2018a, MathWorks, Natick, MA). SWA was computed based on the revisited frequency shift (R-FS) method [164]. SWD was estimated as the slope of the SW phase velocity versus frequency, according to [34, 153], on the same ROI as SWA computations by averaging the velocity field over depth. The A-RANSAC method inspired from [164] was used for line fitting and for finding the slope. For more details on SWA and SWD computation, readers are referred to **Electronic Supplement S2** (**section 5.7.2**).

5.4.4 MR imaging examination

The MRI-PDFF was measured using the Achieva TX 3T MRI system (Philips Healthcare, Best, Netherlands). A two-channel body coil and a 16-channel surface array coil were used for transmission and signal reception. The software versions were R5.3.1 (January 2020-September 2020) and R5.6.1 (September 2020-September 2022), and the sequence was a three-dimensional chemical-shift encoded multi-echo gradient-echo sequence using six echoes (mDixon Quant). A multi-frequency spectral fat model and a T2* correction were used to perform the water/fat separation in the complex domain. Also, to avoid T1 bias, a low flip angle was used. The ratio of the fat proton density to the total fat and water proton density provided the PDFF [213, 223]. MRI-PDFF analysis was performed using OsiriX MD version 9.0.2 by a medical student under the supervision of an experienced radiology investigator. A single slice of the liver was chosen for segmentation at a level where the spleen was well visible and hepatic veins less prominent. The region of interest included left and right livers and excluded the inferior vena cava and Glisson's capsule.

5.4.5 Histological analysis of tissue samples

For patients, liver biopsies were obtained with 16- or 18-gauge needles for clinical care or as NASH Clinical Research Network (CRN) procedures. Hematoxylin-eosin, periodic acid-Schiff, periodic acid-Schiff-diastase, reticulin and Masson's trichrome stains were used [224]. An expert hepato-pathologist ([initials withheld to preserve blinding]) analyzed histology slides and applied the NASH-CRN scoring system [32]. Steatosis was graded from 0 to 3 (S0 to S3), lobular inflammation was graded from 0 to 3 (I0 to I3), hepatocellular ballooning was graded from 0 to 2 (B0 to B2), and fibrosis was staged from 0 to 4 (F0 to F4).

5.4.6 Statistical analysis

Means and standard deviations (SD) of SWE parameters were reported for each imaging session. When the Shapiro-Wilk normality test failed, a non-parametric Kruskal-Wallis rank sum test was used to determine SWA statistical differences between histopathology grades, and corresponding *p*-values were reported. A post hoc Dunn's test was used for multiple pairwise comparisons between histopathological grades and stages.

Linear regressions were used to determine the relationship between liver biopsy grades and SWA measurements. As histopathology grades are semi quantitative, the non-parametric Spearman's rank correlation coefficient was used to assess strengths of correlations between SWA and liver biopsy grades, age, BMI, and sex. Rank correlations were considered low ($r < 0.5$), moderate ($0.5 < r < 0.7$), and high ($r \geq 0.7$) [225]. Multiple linear regression (MLR) analyses of SWA measurements as a function of steatosis, inflammation, ballooning, and fibrosis were performed. Spearman's *r*, regression coefficients, standard errors, 95% confidence intervals (CI), and adjusted R^2 were reported for each technique.

The diagnostic performance of MRI-PDFF, SWA, and SWD for grading liver steatosis was evaluated by the receiver operating characteristic (ROC) curve. The optimal cut-off thresholds of SWA were calculated by the Youden's index [226]. Areas under the curve (AUCs) were compared using the Delong method [227]. ROC curves of SWA for grading steatosis were also plotted for histopathology and MRI-PDFF as the reference standard. Thresholds for assessing steatosis grades using MRI-PDFF were fixed at 6.4, 17.4, and 22.1%, according to [10]. All statistical tests were performed with software R (version x64 4.2.1, R Foundation).

5.5 Results

Among 40 enrolled participants (23 females and 17 males), 13 were healthy volunteers and 27 had NAFLD or NASH. The mean age was 48.8 years (range, 25.3–70.4 years) for women and 55.2 years (range, 27.1–76.0 years) for men. Cohort characteristics are provided in **Table 5.1**. Four patients only had experimental US scans as they were excluded from MRI due to COVID-19, MRI non-compatibility with implants, and claustrophobia. Thirteen healthy volunteers were included and were considered to have no steatosis, fibrosis, inflammation, or ballooning (US and MRI scans but no biopsy). Representative examples of B-mode images and corresponding SWA maps are provided in **Figure 5.2**.

Table 5.1 Characteristics of the 40 participants. Values in parenthesis are in percentages or correspond to the range when specified.

Characteristic	Results
Sex	
Men	17 (42.5)
Women	23 (57.5)
Age (y)	
Mean ± SD (range)	51.5 ± 16.1 (25.3 – 76.0)
BMI (kg/m^2)	
Mean ± SD (range)	
Non-NAFLD volunteers	[22.5 ± 1.8] (18.8 – 24.8)
NAFLD patients	[28.5 ± 4.9] (16.3 – 39.3)
Steatosis grade	
0	13 (32.5)
1	7 (17.5)
2	4 (10.0)
3	16 (40.0)

Lobular inflammation grade	
0	14 (35.0)
1	15 (37.5)
2	5 (12.5)
3	6 (15.0)
Hepatocellular ballooning grade	
0	14 (35.0)
1	16 (40.0)
2	10 (25.0)
Fibrosis stage	
0	15 (37.5)
1	8 (20.0)
2	4 (10.0)
3	6 (15.0)
4	7 (17.5)

Note.— Steatosis grade, lobular inflammation grade, hepatocellular ballooning grade, and fibrosis stage were presumed to be 0 for the 13 healthy volunteers without steatosis.

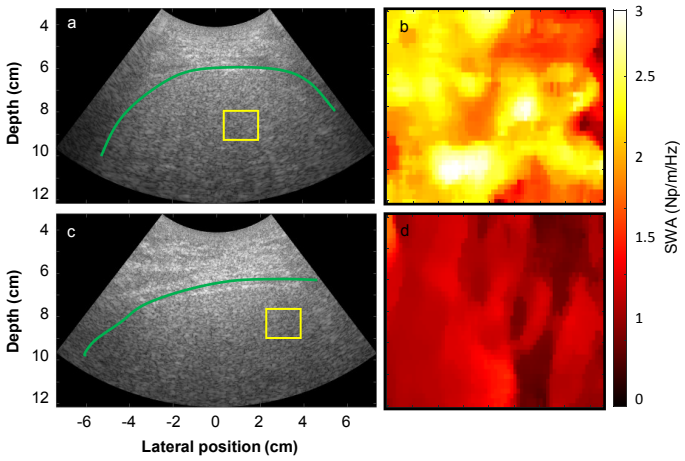

Figure 5.2 The top row shows **(a)** the liver B-mode image and **(b)** the shear wave attenuation (SWA) map of a 45-year-old man with steatosis grade 3, lobular inflammation grade 2, ballooning

grade 1, fibrosis stage 2, and MRI-PDFF of 37.8%. The bottom row shows **(c)** the liver B-mode image and **(d)** the SWA map of a 27-year-old healthy volunteer woman with an MRI-PDFF of 2.1%. Liver boundaries and ROIs of SWA maps are indicated by the green line and the yellow box on B-mode images, respectively.

5.5.1 Shear wave attenuation and histopathological classification

The relationship between SWA and histology grades and stages are shown in **Figure 5.3**. SWA for steatosis grades S0 to S3 were 0.75 ± 0.22, 1.27 ± 0.15, 1.55 ± 0.13, and 1.82 ± 0.30 Np/m/Hz ($p < 0.001$). There were significant differences between S0 and other steatosis grades (S0 vs. S1, S0 vs. S2, and S0 vs. S3), and between S1 and S3 ($p < 0.001$).

SWA for lobular inflammation grades I0 to I3 were 0.79 ± 0.25, 1.58 ± 0.38, 1.79 ± 0.26, and 0.73 ± 0.28 Np/m/Hz ($p < 0.001$), respectively. Differences between mean values of SWA were significantly different between I0 and I1 ($p < 0.001$), I0 and I2 ($p < 0.001$), and I0 and I3 ($p < 0.001$).

SWA for ballooning grades B0 to B2 were 0.79 ± 0.25, 1.71 ± 0.3, and 1.57 ± 0.32 Np/m/Hz ($p < 0.001$), respectively. B0 values were statistically significantly different than B1 ($p < 0.001$) and B2 ($p < 0.001$).

SWA for fibrosis stages F0 to F4 were 0.93 ± 0.53, 1.75 ± 0.32, 1.71 ± 0.29, 1.53 ± 0.34, and 1.41 ± 0.27 Np/m/Hz ($p < 0.001$), respectively. Differences between mean values of SWA were significantly different between F0 and F1 ($p < 0.001$), F0 and F2 ($p < 0.05$), and F0 and F3 ($p < 0.05$).

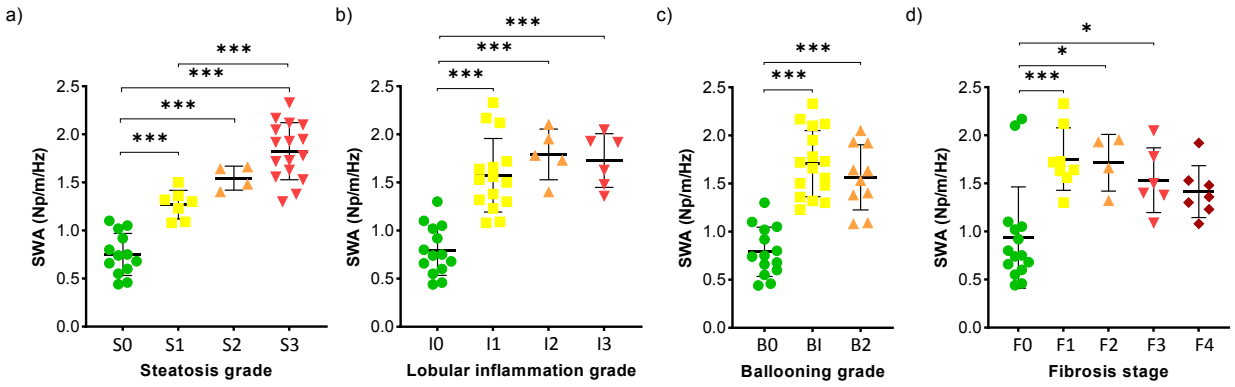

Figure 5.3 Scatter plots, means, and standard deviations of shear wave attenuation (SWA) for different grades of **(a)** steatosis, **(b)** lobular inflammation, **(c)** ballooning, and **(d)** fibrosis. (*: $p < 0.05$, **: $p < 0.01$, and ***: $p < 0.001$).

5.5.2 Univariate and multivariate analyses

Linear regressions, R^2 and p values of SWA are reported in **Table 5.2**. All relations with steatosis, lobular inflammation, ballooning, and fibrosis were statistically significant ($0.13 \leq R^2 \leq 0.79$, $p \leq 0.002$). Based on Spearman's correlations (**Table 5.3**), relations between SWA and steatosis, inflammation, ballooning, and fibrosis were also significant ($0.42 \leq r \leq 0.90$, $p \leq 0.007$). Age and BMI were also correlated with SWA ($p \leq 0.006$). NASH variables with low Spearman's correlations ($r < 0.5$) were neglected in MLR analyses. In MLR models, only SWA was correlated with steatosis grades ($p < 0.001$), with a high determination coefficient ($R^2 = 0.78$).

Table 5.2 Summary of shear wave attenuation (SWA) mean ± SD for different grades of steatosis, lobular inflammation, ballooning, and fibrosis. Linear regressions of SWA with respect to biopsy grades are presented. The R^2 and p values are given in parentheses.

		Steatosis	Inflammation	Ballooning	Fibrosis
		Mean ± SD (Np/m/Hz)	Mean ± SD (Np/m/Hz)	Mean ± SD (Np/m/Hz)	Mean ± SD (Np/m/Hz)
Histopathological grade or stage	0	0.75 ± 0.22	0.79 ± 0.25	0.79 ± 0.25	0.93 ± 0.53
	1	1.27 ± 0.15	1.58 ± 0.38	1.71 ± 0.34	1.75 ± 0.32
	2	1.55 ± 0.13	1.79 ± 0.26	1.57 ± 0.32	1.71 ± 0.29
	3	1.82 ± 0.30	1.73 ± 0.28	-	1.53 ± 0.34
	4	-	-	-	1.41 ± 0.27
Linear regression		0.35 x + 0.80 (R^2 = 0.79, p < 0.001)	0.34 x + 0.98 (R^2 = 0.47, p < 0.001)	0.42 x + 0.97 (R^2 = 0.41, p < 0.001)	0.12 x + 1.16 (R^2 = 0.13, p = 0.02)

Table 5.3 Univariate and multivariate linear regression analyses of shear wave attenuation (SWA) versus liver histopathology grades, age, sex, and body mass index.

	Univariate analysis			**Multiple linear regression analysis**			
	Spearman's r	95% CI	p value	Estimated coefficient	95% CI	p value	Adjusted R^2
Steatosis	0.90	0.81, 0.95	< 0.001	0.33	0.23, 0.43	< 0.001	0.78
Lobular inflammation	0.77	0.60, 0.87	< 0.001	0.10	-0.03, 0.23	0.13	
Ballooning	0.66	0.42, 0.81	< 0.001	-0.04	-0.23, 0.15	0.70	
Fibrosis	0.42	0.12, 0.65	0.007	-	-	-	
Age (y)	0.42	0.12, 0.66	0.006	-	-	-	
Body mass index (kg/m^2)	0.48	0.20, 0.70	0.002	-	-	-	
Sex	0.12	-0.21, 0.42	0.47	-	-	-	

5.5.3 Diagnostic performance

Estimates of diagnostic performance of MRI-PDFF, SWA, and SWD to grade liver steatosis (ROC analyses) are given in **Figure 4**. For differentiating S0 vs. ≥S1, there were no significant differences between AUCs of MRI-PDFF, SWA, and SWD (respectively 0.97, 0.99, and 0.93). For differentiating S1 vs. ≥S2, AUCs were similar for MRI-PDFF and SWA (0.95 vs. 0.98), but significantly higher for SWA than SWD (0.98 vs. 0.80; $p = 0.006$). For differentiating ≤S2 vs. ≥S3, AUCs were similar for MRI-PDFF and SWA (0.93 vs. 0.95), but significantly higher for SWA than SWD (0.95 vs. 0.73; $p = 0.03$), and significantly higher for MRI-PDFF than SWD (0.93 vs. 0.73; $p = 0.03$).

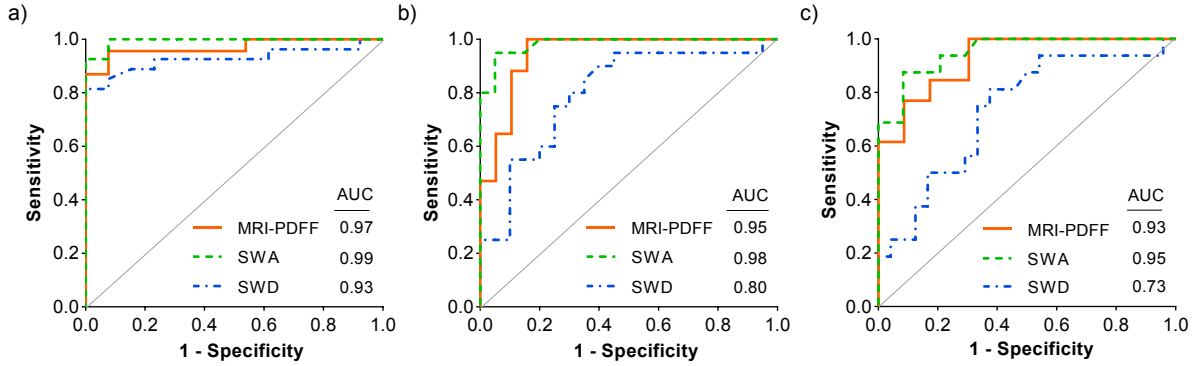

Figure 5.4 ROC curves of MRI-PDFF, SWA, and SWD for dichotomization of **(a)** S0 vs. ≥ S1, **(b)** ≤ S1 vs. ≥ S2, and **(c)** ≤ S2 vs. S3 using histopathological grading as the reference standard.

ROC curves of SWA for grading steatosis were also plotted for histopathology and MRI-PDFF as the reference standard (**Figure 5.5**). Using histopathology as reference, SWA had AUCs of 0.99 for differentiating S0 vs. ≥S1, 0.98 for differentiating ≤S1 vs. ≥S2, and 0.95 for differentiating ≤S2 vs. S3. Using MRI-PDFF as reference, SWA had AUCs of 0.91 for differentiating S0 vs. ≥S1, 0.90 for differentiating ≤S1 vs. ≥S2, and 0.91 for differentiating ≤S2 vs. S3. SWA Youden's thresholds for steatosis grading are reported in **Table 5.4**. Optimal SWA thresholds for grading steatosis were respectively 1.07, 1.37, and 1.51 Np/m/Hz for S0 vs. ≥S1, ≤S1 vs. ≥S2, and ≤S2 vs. S3 using biopsy as the reference standard, and respectively 1.17, 1.49, and 1.75 Np/m/Hz when using MRI-PDFF as the reference standard.

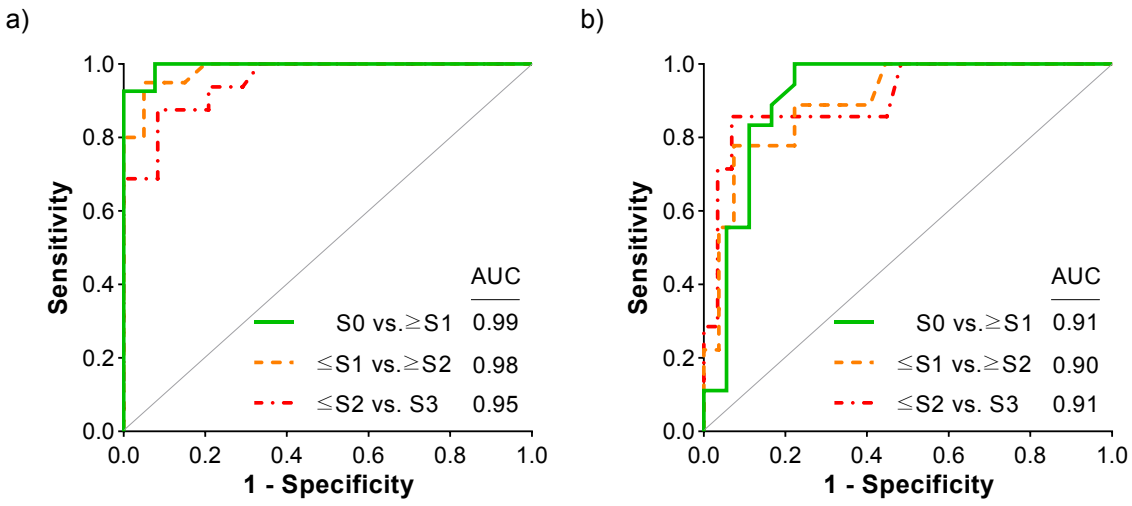

Figure 5.5 ROC curves of SWA for grading liver steatosis using **(a)** histopathology or **(b)** MRI-PDFF as the reference standard.

Table 5.4 Shear wave attenuation (SWA) optimal cut-off values and associated sensitivity, specificity, positive predictive value (PPV), and negative predictive value (NPV) for different steatosis grades using biopsy and MRI-PDFF as the reference standard.

Steatosis grades	**Reference standard: biopsy**				
	Cut-off (Np/m/Hz)	Sensitivity [95% CI]	Specificity [95% CI]	PPV [95% CI]	NPV [95% CI]
S0 vs. ≥ S1	1.07	1.00 [0.88, 1.00]	0.92 [0.67, 1.00]	0.97 [0.77, 1.00]	1.00 [0.95, 1.00]
≤ S1 vs. ≥ S2	1.37	0.95 [0.76, 1.00]	0.95 [0.76, 1.00]	0.95 [0.86, 1.00]	0.95 [0.85, 1.00]
≤ S2 vs. S3	1.51	0.87 [0.64, 0.98]	0.92 [0.74, 0.99]	0.88 [0.71, 1.00]	0.92 [0.81, 1.00]
	Reference standard: MRI-PDFF				
	Cut-off (Np/m/Hz)	Sensitivity [95% CI]	Specificity [95% CI]	PPV [95% CI]	NPV [95% CI]
S0 vs. ≥ S1	1.17	1.00 [0.83, 1.00]	0.78 [0.55, 0.91]	0.82 [0.66, 0.98]	1.00 [0.95, 1.00]
≤ S1 vs. ≥ S2	1.49	0.89 [0.57, 0.99]	0.79 [0.61, 0.90]	0.57 [0.31, 0.83]	0.95 [0.87, 1.00]
≤ S2 vs. S3	1.75	0.86 [0.49, 0.99]	0.93 [0.78, 0.99]	0.75 [0.45, 1.00]	0.96 [0.90, 1.00]

5.6 Discussion

In this prospective pilot study, SWA imaging was investigated as a biomarker for assessing hepatic steatosis, lobular inflammation, ballooning, and fibrosis. Histopathology was used as the reference standard. Liver biopsy specimens were evaluated according to the NASH CRN Pathology Committee using the NAFLD histology scoring system.

At univariate analysis, SWA provided low to high correlations with liver steatosis, lobular inflammation, ballooning scores, and fibrosis. However, at multivariate regression, only SWA was strongly correlated with liver steatosis. SWA provided a high diagnostic performance for classification of dichotomized steatosis grades. We then computed SWA cut-off thresholds for differentiating steatosis grades, either using biopsy or MRI-PDFF as the reference standard. The use of SWA to assess liver steatosis was recently evaluated in a few clinical cases. Ormachea and Parker [177] and Sharma *et al.* [176] reported a moderate correlation between SWA and steatosis grades (Spearman's $r = 0.52$ and $r = 0.69$, respectively). The higher correlation observed in our study ($r = 0.90$) may be explained by the higher number of study participants and the inclusion of healthy volunteers, which provides a broader spectrum of liver conditions. Moreover, in their studies, SWA were computed with a different algorithm at a single frequency.

Because MRI-PDFF and SWD were previously reported to be correlated with steatosis grades [219], we compared the performance of SWA to those biomarkers in the current study. Based on ROC-AUCs, we could demonstrate better performance of SWA and MRI-PDFF than SWD, and similar performance for SWA and MRI-PDFF. This latter observation constitutes a significant advance when considering the value of MRI-PDFF as an alternative reference standard to biopsy for assessing liver steatosis [10, 224, 228-230]).

One of the above cited studies compared the diagnostic performance of SWA and SWD. Ormachea and Parker [177] found that the SWA-AUC for steatosis detection (S0 vs. ≥S1) was higher than that of SWD. On the other hand, AUCs of SWA and SWD were similar for grading the steatosis severity (S1 vs. S2 and ≤S2 vs. S3) [177], whereas we found that SWA provided higher performance than SWD for all steatosis grades. Differences between both studies may again be attributed to the algorithm, and frequencies considered for computing SWA. In our study, SWA was based on a gamma fitting on the whole available frequency bandwidth, whereas in [177] it was

assessed at a fixed frequency of 150 Hz. This is relevant because the chosen frequency bandwidth is known to influence SWA computation [175]. Some studies on SWA reported results at a single frequency [176, 177] or in a range of frequencies [28, 29, 31, 159, 164].

The frequency range is also a source of variation for SWD. Bandwidths from 30 to 450 Hz were reported for liver imaging [34, 37, 153]. In the current study, the selected bandwidth (67–110 Hz) was within reported ranges and it was kept constant for all datasets. To reduce the impact of outliers (*i.e.*, variability in magnitude of frequency spectra), the A-RANSAC method was used to improve robustness of SWD computations. The A-RANSAC applied on gamma fittings of frequency spectra was also used for SWA analyses.

To differentiate histologically-determined steatosis grades with SWA, we computed thresholds that maximized the Youden index. We found a good sensitivity (0.87-1.00) and a high specificity (0.92-0.95) to differentiate steatosis grades. When using biopsy as the reference standard, SWA provided higher sensitivity than MRI-PDFF and the same range of specificity according to previous studies [10, 213]. If independently validated in larger cohorts, SWA may constitute an alternative to MRI-PDFF due to its potential implementation on US scanners, cost-effectiveness, and availability as a point of care tool for screening of liver steatosis.

Quantitative US (QUS) methods that have been investigated as alternative approaches to biopsy for assessment of liver steatosis have also attracted some attentions. Recent studies have evaluated the compression wave attenuation coefficient [171], backscatter coefficient [231], or both attenuation and backscatter coefficients [232] for assessment of steatosis. One limitation of these QUS-based methods is their dependency on reference phantoms for calibrations, but some efforts have been made to overcome this issue [232, 233]. In a recent study involving patients with NAFLD across multiple centers, the effectiveness of multiparametric US was evaluated using various techniques, including attenuation imaging (ATI) to measure the compression wave attenuation coefficient, as well as two-dimensional SWE to assess liver stiffness and dispersion slope [171]. However, further head-to-head comparisons of performances between the most recent SWA technologies and QUS-based techniques on same patients remain to be performed in future studies.

This study has some limitations. First, due to the relatively low number of patients in this pilot study, some combinations of histopathological features were not available (*e.g.*, a patient with

S0 and >F1 or a patient with F0 and S2). Therefore, the diagnostic performance assessment might not have considered the whole spectrum encountered in NASH. Second, since there were no SWA thresholds published in the literature for liver steatosis grading, it was not possible to compare our results with prior results. Finally, the time interval between biopsy and US or MRI measurements was 41.9 ± 21.1 days. SWA accuracy for NASH assessment may be improved using a closer time interval between biopsy, US, and MR imaging [213].

In conclusion, this pilot, prospective, cross-sectional study in a cohort of volunteers and patients with biopsy-confirmed NAFLD or NASH demonstrated the feasibility of SWA to become a noninvasive biomarker for early detection of hepatic steatosis with high sensitivity and specificity. Also, SWA provided excellent accuracy for classification of moderate and severe steatosis grades, whether considering biopsy or MRI-PDFF as the reference standard in this pilot study. Prospective studies with larger cohorts will help validate the diagnostic performance of SWA for noninvasive detection and grading liver steatosis.

5.7 Electronic supplement

5.7.1 (S1) Safety usage of the research ultrasound scanner in shear wave elastography mode

5.7.1.1 Introduction

The human liver imaging sequence developed for this study successively performed ultrasound transmissions and receptions [124]. **Figure 5.6** shows the ultrasound sequence that included B-mode imaging, quantitative ultrasound imaging (QUS, not used in the current study), and 10 shear wave elastography (SWE) acquisitions.

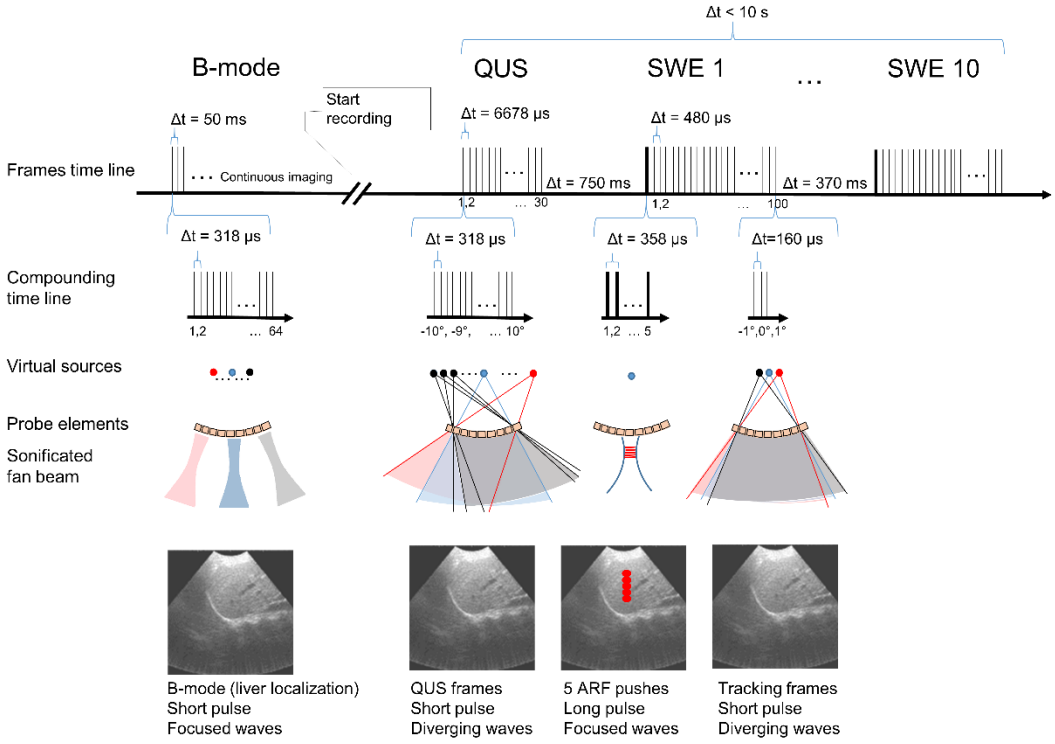

Figure 5.6 Schematic of the human liver imaging sequence. ARF: acoustic radiation force, QUS: quantitative ultrasound, SWE: shear wave elastography.

First, conventional B-mode imaging was used to position the plane and the push location for SWE image acquisitions. The QUS mode allowed acquiring 30 radiofrequency (RF) images. Each image was obtained by compounding divergent wave images at 21 different angles (from -10° to 10°) at a frame rate of 150 per second.

Then, in the SWE mode, each acquisition included 10 SW propagation at the same depth but with different radiation pressure angles (-5° to 5°). Each SWE acquisition begun by focusing 5 pushes (992 cycles long, 357 µs long) at a given angle and 5 axially adjacent points with 3 mm distances in depth to produce a plane SW [100]. The focused push beams were transmitted by 64 elements of the transducer at a center frequency of 2.8 MHz. A radiology technologist positioned the first and last push locations to ensure that all of them targeted liver parenchyma and avoided major vessels. The same transducer was used to track SWs immediately after their propagation at a pulse repetition frequency (PRF) of 6,225 Hz. The propagation of SWs was then tracked by acquiring 100 frames made of ultrafast (2,083 frames per second) divergent waves. At the end of the sequence, the scanner was frozen. Parameters used in this sequence are presented in **Table 5.5**.

Table 5.5 Programmed parameters of the ultrasound sequence for human liver imaging.

Mode	Wave duration (µs)	Wave frequency (MHz)	Wave cycles	PRF (Hz)	Compounding (number of angles)	Focus depth (mm)	Frame rate (s^{-1})	Wave amplitude (volts)
B-mode	0.64	3.125	2	1280	64	50	20	20
Diverging wave QUS	0.64	3.125	2	3145	21	NA	150	30
SWE push	357	2.778	992	2793	5	20-80	N/A	25 or 42
Diverging wave SWE tracking	0.64	3.125	2	6225	3	NA	2083	30

PRF: pulse repetition frequency, QUS: quantitative ultrasound, SWE: shear wave elastography.

Measurements were made to make sure that the energy and acoustic pressure of B-mode, and SWE-mode met regulation standards. The chosen method was inspired by the work of Herman

and Harris [234] and Palmeri *et al*. [235]. Shortly, the maximum of the peak rarefaction was measured using a hydrophone to determine the mechanical index (MI), and the intensity spatial peak temporal averaged (I_{SPTA}). The thermal index was computed from those maxima. MI indicates the ultrasound sequence's ability to cause cavitation-related bioeffects. I_{SPTA} corresponds to the maximum beam intensity averaged over the examination duration. The thermal index corresponds to the quantification of the rise in tissue temperature that may occur during the examination [234, 235]. The food and drug administration (FDA) of the United States recommends to keep either the MI below 1.9 or the intensity spatial peak pulse averaged (I_{SPPA}) below 190 W/cm² [236, 237]. The limiting values for MI and I_{SPPA} are not independent; if either one of them falls below the designated FDA limit, then the other is permitted to exceed the limit [238]. The limit for the I_{SPTA} is 720 mW/cm² as elastography complies with track 3 in [236, 237, 239], while the thermal index must remain under 6 °C [235, 237]. In this work, MI, I_{SPTA}, and thermal index were assessed to investigate the compliance with FDA limits. The maximal sonication power was then limited for the safety of volunteers and patients, and approved by the institutional review board of the Centre de recherche du Centre hospitalier de l'Université de Montréal (CRCHUM)

5.7.1.2 Acoustic measurements

MI, I_{SPTA}, and the thermal index were determined for the selected imaging sequence. A membrane hydrophone (HMB-0200, ONDA Corp., Sunnyvale, CA, USA) connected to a digital oscilloscope (CompuScope 12501, Vitrek LLC, Lockport, IL, USA) was positioned at the bottom of a double-distilled deionized water tank. The research ultrasound system (Verasonics Vantage, Kirkland, WA, USA) was connected to the ATL C5-2 clinical probe (Philips Healthcare, Andover, MA, USA). The 100 MHz hydrophone sampled signals were converted to sound pressure (Pascal) using the sensitivity of the hydrophone at 2.8 MHz (196 mV/Pa). The ultrasound probe was attached to a computer-controlled multi-axis robotic system (ACR9000, Parker Hannifin Corp., Rohnert Park, CA, USA) to localize the maximum pressure position. Because acoustic power measurements were made in a water tank and not in an attenuating tissue environment, the FDA recommends to compensate the attenuation by using a derating attenuation factor of α = 0.3 $dB.MHz^{-1}.cm^{-1}$. The perpendicularity between the hydrophone and the probe was aligned manually using the real-time focused B-mode.

A dedicated pressure measurement strategy was programmed using Matlab (The Mathworks, Natick, MA, USA) to synchronise Verasonics sequence transmissions during hydrophone measurements. Transmitted voltages of 10, 20, 30, 40, and 50 V were studied for a focus distance between the probe and the location of the push of 20, 30, 40, 60, and 80 mm. SWE acoustic pressure measurements included 50 cycles pushes instead of 992 cycles to prevent hydrophone damage (as the amplitude of pushes is constant, this did not impact the identification of the peak rarefaction maximum). Every ultrasound emission was repeated 16 times for averaging purpose. Because acoustic outputs in SWE-mode are much higher than in B-mode or QUS-mode, results given next correspond to the SWE sequence component.

5.7.1.3 Results

5.7.1.3.1 Mechanical index (MI)

MI as a function of focus depths and selected voltages for a derating value of 0.3 $dB.MHz^{-1}.cm^{-1}$ is presented in **Figure 5.7**. To stay below the FDA limit of 1.9, the maximum voltage for SWE measurements at depths ≥ 40 mm was limited to 42 V. For smaller depths, the voltage was limited to 25 V (**Table 5.6**). For comparison, MI in B-mode with parameters of **Table 5.5** was 0.28.

Table 5.6 The voltage used for shear wave elastography (SWE) pushes at different user selected push depths for human liver imaging.

Focus distance	20 mm	30 mm	40 mm	60 mm	80 mm
Voltage	25 V	25 V	42 V	42 V	42 V

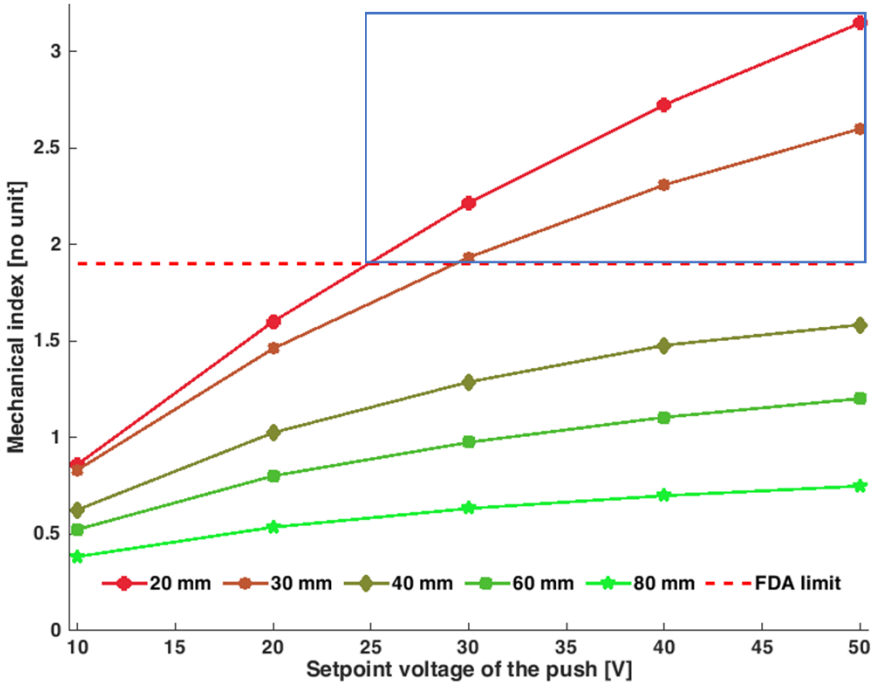

Figure 5.7 Measured mechanical index (MI) in shear wave elastography (SWE) mode as a function of the selected voltage for different focus depths using a hydrophone in a water tank. A derating attenuation value of 0.3 dB.MHz-1.cm-1 was considered for those measurements. The MIs and voltages in blue box never have been used for human acquisition.

5.7.1.3.2 Intensity spatial peak temporal averaged (I_{SPTA})

I_{SPTA} results as a function of depth are given in **Figure 5.8** for selected voltages in **Table 5.6** The voltage used for shear wave elastography (SWE) pushes at different user selected push depths for human liver imaging.. For every radiation pressure depth, I_{SPTA} was lower than the FDA threshold of 720 mW/cm^2. This was achieved by adjusting the delay between the 10 SWE repetitions. In B-mode, it was 6.15 mW/cm^2.

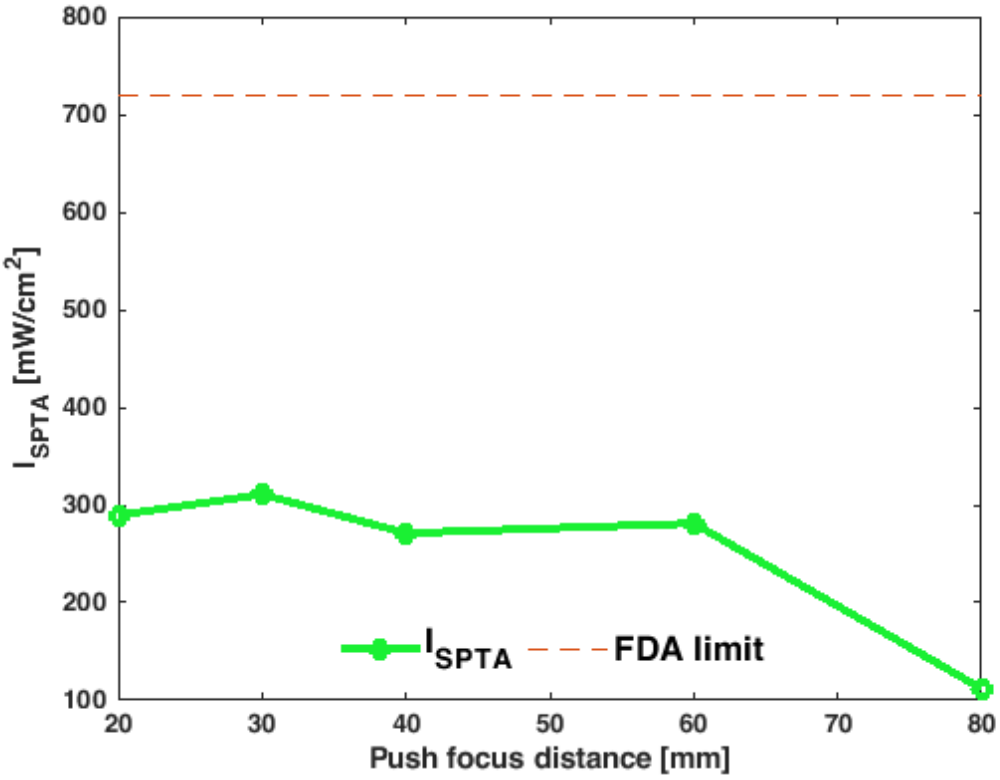

Figure 5.8 Measured intensity spatial peak temporal averaged (I_{SPTA}) in mW/cm^2 as a function of the focus depth for the maximum selected voltage limit (**Table 5.6**) programmed on the Verasonics system for human liver imaging.

5.7.1.3.3 Thermal index

Figure 5.9 presents the estimated thermal index in soft tissues of the SWE sequence as a function of depth for voltages in **Table 5.6**. For every push focus depth, the index was close to 4 ^{o}C and below the FDA threshold of 6 ^{o}C. The estimated thermal index in B-mode using the parameters of **Table 5.5** was 0.09 ^{o}C.

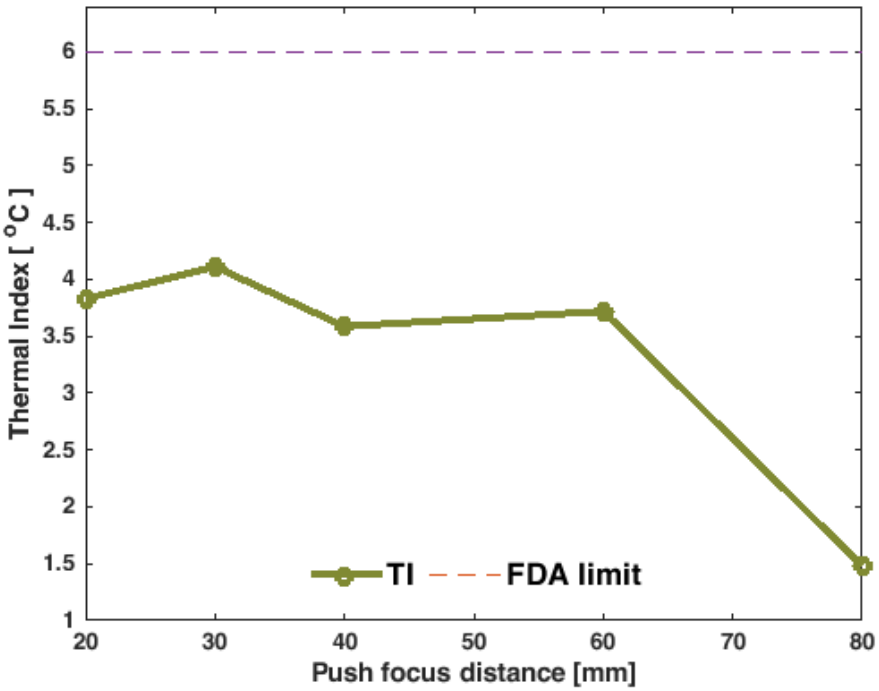

Figure 5.9 Estimated thermal index (TI) in °C as a function of the focus depth for the maximum selected voltage limit (**Table 5.6**) programmed on the Verasonics system for human liver imaging.

5.7.1.4 Discussion

The result in **Figure 5.7** showed that the research ultrasound system could exceed FDA safety criteria when the selected voltage was not constrained within a safe range for given radiation pressure depths. SWE pushes are particularly at risk of overrunning FDA limits since they combine the use of focused waves, high voltages, and several hundreds of emitted cycles.

According to the FDA, compliance with the restriction of MI and I_{SPTA} is sufficient to limit the risk from acoustic output exposure levels [236, 237]. These two parameters are below the FDA limits based on the results in **Figure 5.7** and **Figure 5.8**. As also reported, the thermal index is not well suited for the acoustic radiation force imaging (ARFI) and SWE imaging modalities [240, 241]. According to [242], for the thermal index of 4, the maximum safe duration of examination without thermal risk would be 15 seconds, while all liver imaging sequence in this work lasted less than 10 seconds. Furthermore, as each SWE repetition uses a different radiation angle, diffusion can occur and reduce the heating inside the liver [17]. Thermal index values were presented here

for informative purpose only. Throughout our sequence design process, safety margins have been added to the various parameters of the sequence to respect the principle of ALARA (as low as reasonably achievable). By fixing the maximum voltage at a given depth, the sequence used for this NAFLD human study met all safety criteria recommended by the FDA. By applying the ALARA principle, it was decided to lengthen delays between SWE radiation pressure pushes to reduce the frame rate, and to change the angle between the 10 consecutive push lines to increase the safety for human liver scanning. In addition, it took about one minute to save RF data after running the sequence. During data saving, no ultrasonic emissions were possible, further reducing the risk of thermal overheating.

5.7.2 (S2) Ultrasound shear wave data acquisition and parameter computation

5.7.2.1 Shear wave attenuation (SWA)

The R-FS method was used for SWA computation [164]. This algorithm assumes the amplitude spectrum of SWs to be proportional to a gamma density distribution. If a SW has a frequency spectrum $S(f)$ at a lateral distance x_0, then:

$$S(f) \propto f^{k_0-1} e^{f\beta_0}$$

where f is the SW frequency, and k_0 and β_0 are the shape and rate parameters of the gamma function, respectively. The attenuation coefficient (α) was computed by fitting the gamma spectrum at a lateral distance Δx, and finding the slope of the rate parameter with respect to Δx (*i.e.*, $\beta(\Delta x) = (\beta_0 + \alpha \Delta x)$). Both the shape and rate parameters are allowed to vary with the R-FS method, and the A-RANSAC algorithm was used for line fitting [164].

Ten SWA maps were reconstructed from each acquisition by applying the R-FS method on the defined ROI. SWA coefficients were averaged on each pixel using images with gamma fitting providing coefficients of determination $R^2 > 0.8$ or larger.

5.7.2.2 Shear wave dispersion (SWD)

SWD was estimated as the slope of the SW phase velocity versus frequency, according to [34, 243], on the same ROI as SWA computations by averaging the velocity field over depth. The A-

RANSAC method was used for line fitting and for finding the slope. The SWD was computed between averaged values of the lower frequency at half maximum (67 Hz) and peak frequency (110 Hz), determined *a posteriori* on the whole dataset. For a given acquisition, SWD values were estimated from ten SW records, and the mean and standard deviation (SD) were computed for line fittings with $R^2 > 0.8$ or larger.

5.8 Funding information

This work was supported in part by the Natural Sciences and Engineering Research Council of Canada under Grant 2022-03729, in part by the Canadian Institutes of Health Research under Grant 389385, and in part by the Oncotech consortium (Oncopole, Medteq, Transmedtech, Cancer Research Society, Fonds de Recherche Santé du Québec, and Siemens Healthcare) under Grant 293741. Salary award by the Fonds de recherche du Québec en Santé and Fondation de l'association des radiologistes du Québec (FRQS-FARQ #298509) was obtained by An Tang. Giada Sebastiani is supported by a Senior Salary Award from *FRQS* (#296306).

5.9 Disclosures

Giada Sebastiani has acted as speaker for Pfizer, Merck, Novonordisk, Novartis, Gilead, and AbbVie; served as an advisory board member for Merck, Gilead, Pfizer, Allergan, Novonordisk, Intercept, and Novartis; and has received unrestricted research funding from Theratechnologies Inc. An Tang and Guy Cloutier have received equipment loans and funding from Siemens Healthcare.

5.10 Acknowledgements

We thank Dr. Marie-Hélène Roy-Cardinal for her guidance in statistical analysis and Mr. Miloud Zenati for his assistance in patient enrollment and data collection.

Chapter 6 – Between-visit reproducibility of shear wave viscoelastography in volunteers and patients with nonalcoholic fatty liver disease

6.1 Introduction to manuscript

This chapter reproduces the content of an under review article 'Between-visit reproducibility of shear wave viscoelastography in volunteers and patients with nonalcoholic fatty liver disease' in the journal "Ultrasound in medicine and biology by Ladan Yazdani, Sathiyamoorthy Selladurai, Iman Rafati, Manish Bhatt, Damien Olivié, Jeanne-Marie Giard, Giada Sebastiani, Bich N. Nguyen, Guy Cloutier, and An Tang.

The following is the order of authors for this published article and corresponding affiliations:

Ladan Yazdani[1,2], Sathiyamoorthy Selladurai[1], Iman Rafati[1,2], Manish Bhatt[1,3], Damien Olivié[4], Jeanne-Marie Giard[5], Giada Sebastiani[6], Bich N. Nguyen[7], Guy Cloutier[1,2,4], and An Tang[4,8,*].

Affiliations:

1 Laboratory of Biorheology and Medical Ultrasonics (LBUM), Centre de recherche du Centre hospitalier de l'Université de Montréal (CRCHUM), Montréal, Québec, Canada;

2 Institute of Biomedical Engineering, Université de Montréal, Montréal, Québec, Canada;

3 Department of Electronics and Electrical Engineering, Indian Institute of Technology, Guwahati, India;

4 Department of Radiology, Radiation Oncology and Nuclear Medicine, Université de Montréal, Montréal, Québec, Canada;

5 Department of Hepatology, Université de Montréal, Montréal, Québec, Canada;

6 Division of Gastroenterology and Hepatology, McGill University Health Centre, Montreal, Quebec, Canada;

7 Service of Pathology, Centre hospitalier de l'Université de Montréal (CHUM), Montréal, Québec, Canada;

[8] Laboratory of Clinical Image Processing, CRCHUM, Montréal, Québec, Canada.

[*] Corresponding author

The contributions of all authors of the published article are detailed below:

Ladan Yazdani: developed and updated the algorithms of the viscoelastic parameters for utilizing in *in vivo* human liver, updated beamforming algorithms, performed statistical analysis, drafted the manuscript and will respond to the reviewer's comments of the article.

Sathiyamoorthy Selladurai: contributed to the beamforming processing and drafting the manuscript.

Iman Rafati: contributed to the statistical analysis and drafting the manuscript.

Manish Bhatt: developed and implemented some of the viscoelastic parameters and beamforming algorithms.

Damien Olivié, Jeanne-Marie Giard, and Giada Sebastiani: contributed to the clinical aspects of this work.

Bich N. Nguyen: performed to the histopathological assessments of the liver biopsies.

Guy Cloutier: contributed to the interpretation of the validations, results, and revision of the manuscript.

An Tang: supervised this work as the co-research director, contributed to the interpretation of results as the project director, corrected, and finalized the manuscript for submission and revision.

6.2 Abstract

Objective: To assess the reproducibility of six ultrasound (US)-determined shear wave (SW) viscoelastography parameters for assessment of mechanical properties of liver in volunteers and patients with biopsy-proven nonalcoholic fatty liver disease (NAFLD).

Methods: This prospective, cross-sectional, institutional review board-approved study included 10 volunteers and 10 patients with NAFLD who underwent liver US elastography twice, at least two weeks apart. SW speed (SWS), SW attenuation (SWA), SW dispersion (SWD),

Young's modulus (E), shear modulus (|G|), and viscosity were computed from radiofrequency data recorded on a research US scanner. The reproducibility of measurements was assessed by the coefficient of variation (CV), the intraclass correlation coefficient (ICC), and a Bland-Altman analysis.

Results: CV s of SWS, SWA, SWD, E, |G|, and viscosity were 7.86%, 9.82%, 21.37%, 17.67%, 18.36%, and 29.38%; ICCs were 0.93 (95% confidence intervals [CI]: 0.84-0.97), 0.97 (95% CI: 0.95-0.99), 0.91 (95% CI: 0.79-0.96), 0.92 (95% CI: 0.82-0.97), 0.93 (95% CI: 0.84-0.97), and 0.95 (95% CI: 0.89-0.98); and Bland-Altman mean biases and 95% limits of agreement were -0.02 (-0.21, 0.17), 0.04 (-0.19, 0.27), -0.52 (-5.51, 4.45), -0.15 (-1.96, 1.66), -0.05 (-0.72, 0.62), and -0.01 (-0.78, 0.75), between the two visits, respectively.

Conclusion: US-determined viscoelastography parameters can be measured with high reproducibility and consistency between two visits.

Key points:

• Within-visit CVs of US-determined viscoelastography parameters in volunteers and adults with biopsy-proven nonalcoholic fatty liver disease of 7.86% to 29.38% indicate good precision; best results are with SWS and SWA.

• Between-visit ICCs of US-determined viscoelastography parameters ranging from 0.91 to 0.97 indicate high reproducibility for all measures.

• Bland-Altman biases of US-determined viscoelastography parameters were small for all measures.

Key words: ultrasound imaging; reproducibility; bias; viscoelasticity; nonalcoholic fatty liver disease (NAFLD); nonalcoholic steatohepatitis (NASH); fibrosis.

6.3 Introduction

Nonalcoholic fatty liver disease (NAFLD) has a high prevalence and is encountered in 25% of the adult Western population [244]. One of key challenges with NAFLD is to differentiate simple steatosis from the more advanced form known as nonalcoholic steatohepatitis (NASH), and NASH-

induced fibrosis and cirrhosis [245]. This spectrum of NAFLD is characterized by macrovesicular steatosis, lobular inflammation, hepatocellular ballooning, and fibrosis [32]. While liver biopsy constitutes the reference standard for diagnosis of NASH, there is a need to investigate noninvasive diagnostic techniques [38, 207].

In this regard, ultrasound (US) elastography approaches seem promising and are finding their way into clinical use. US elastography has provided an important means of assessing fibrosis or steatosis in the liver tissue [246]. Current quantitative methods include transient elastography (TE) and shear wave elastography (SWE). They provide an estimate of the quantitative stiffness of an insonified tissue. TE provides stiffness measurements from only selected locations identified blindly, as it is not integrated with a standard US system that can provide a B-mode image for guidance. SWE measures parameters such as SW speed (SWS) to measure liver stiffness [23]. However, in recent years, more attention has been given to SW attenuation (SWA) as a measure of the dispersive characteristics of a tissue [28, 31, 164, 176]. SW dispersion (SWD) and viscosity are other parameters that have also been explored to quantify the lossy nature of biological tissues [27, 34, 158]. Liver stiffness is enhanced by fibrosis, and viscosity-based measures might help to grade fatty liver disease.

Prior studies have focused on US-based SWE for staging liver fibrosis [35, 36]. However, because as many quantitative parameters could be required as there are histopathological unknowns, there is interest in exploring additional parameters. Recently, six SW viscoelasticity-based biomarkers have been examined in the context of a preclinical model of NAFLD [37]: SWS, SWA, SWD, Young's modulus (E), shear modulus (G), and viscosity. To advance acceptance of US-based SW viscoelastography biomarkers of NAFLD and NASH, it is important to evaluate their reproducibility [38]. To minimize sources of variability, an automated method averaging measurements from several radiation pressure pushes at three angles and repeated 10 times has been developed [Chapter 5]. This SWE acquisition sequence was used for the current report.

The purpose of this study was to assess the reproducibility of six US-based SW viscoelastography parameters for the assessment of mechanical properties of livers in volunteers and patients with biopsy-proven NAFLD.

6.4 Materials and Methods

6.4.1 Study design and subjects

This is a single-site, prospectively designed, cross-sectional study to evaluate the reproducibility of SW viscoelastography biomarkers. This study was approved by the institutional review board of the institutional review board of the Centre de recherche du Centre hospitalier de l'Université de Montréal (CRCHUM). Ten normal volunteers and ten patients with biopsy-proven NAFLD were recruited between November 2019 and February 2022. Volunteers were adults with no risk factors for developing liver steatosis, such as type 2 diabetes mellitus, alcohol consumption >60 g per day, lipogenic medication, and body mass index >25 kg/m2. Patients were adults with biopsy-proven NAFLD or NASH. They were excluded if they had another cause of chronic liver disease or a liver transplant. Flow chart of patient enrollment is illustrated in **Figure 6.1**.

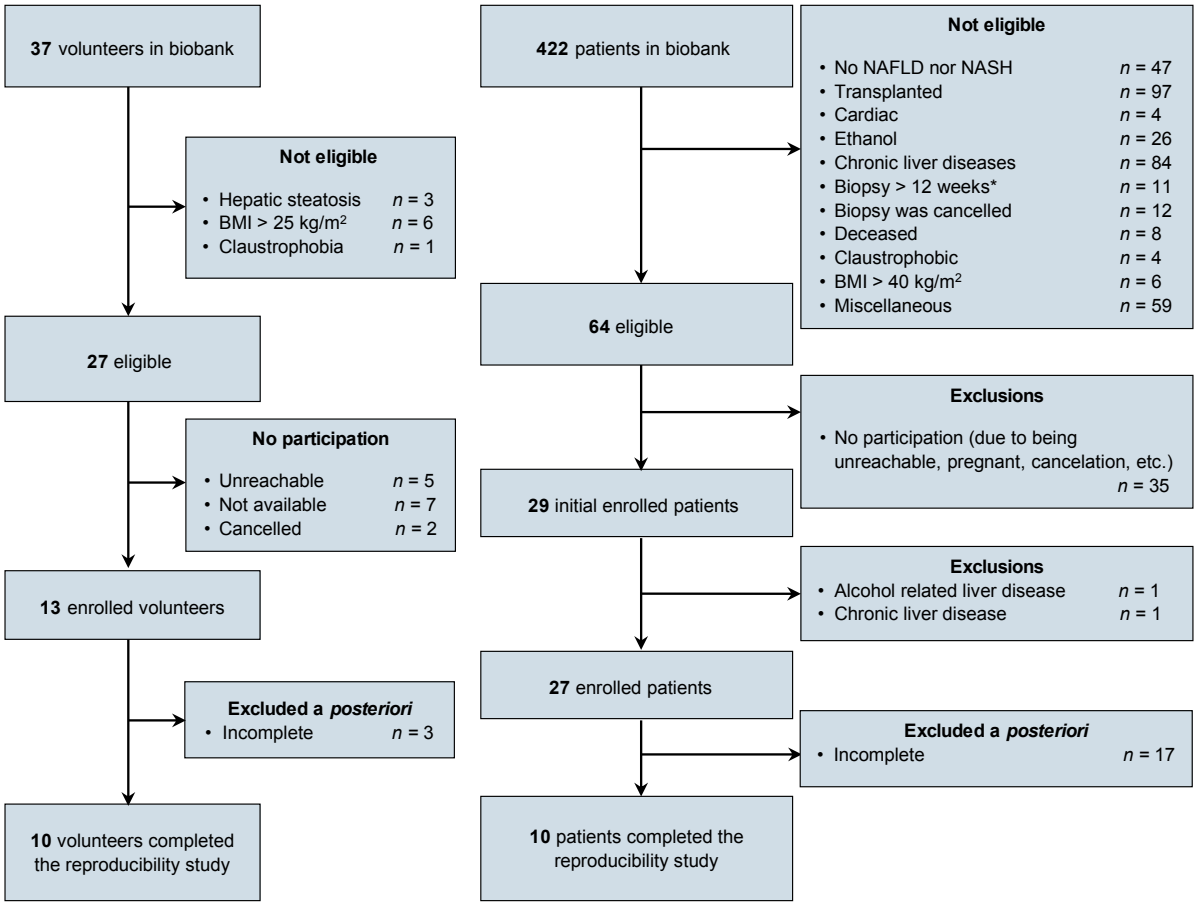

Figure 6.1 Flowchart of the participant enrollment process.

6.4.2 Ultrasound examinations

US exams were repeated at least 13 days apart for all study participants to prevent recall bias. The first US examinations were done within 49.4 ± 22.1 days of the liver biopsy.

6.4.3 Ultrasound data acquisition

Subjects were required to fast at least 3 hours prior to US examination and were examined supine. A Verasonics Vantage programmable system (Verasonics Inc., Kirkland, WA, USA) was used to perform US measurements using a 128-element C5-2 curvilinear probe (Philips, WA, USA) driven at 5 MHz. First, conventional B-mode imaging allowed the placement of the imaging plane and the position of SW pushes in the area of interest where SWE image acquisitions were

subsequently performed. Each SWE mode began by focusing 5 pushes (992 cycles long) at 5 axially adjacent points to produce a plane SW. This process was performed at ten angles of -5o to 5o. The propagation of SWs at each angle was then tracked by acquiring 100 radiofrequency (RF) frames made of ultrafast (2083 frames per sec.) divergent waves. The SWE acquisition was repeated 10 times at the same depth with different radiation pressure angles (-5° to 5°) for averaging purpose [see Supplementary material (**section 5.7.1**) in Chapter 5].

6.4.4 Shear wave elastography (SWE)

For all reported results, SWE computations were averaged from measurements over the 10 acquisitions with ten different angles. The liver was assumed to be locally homogeneous, and computations were performed over a region-of-interest (ROI) of size 1.2 cm × 1.5 cm or smaller in cases the segmented contour had a smaller size because of noise. The SW velocity field inside the liver was computed using a 2D auto-correlation algorithm [190] and a directional filter was used [191]. This ROI was selected 3 mm on the right of the foremost push line, at depths corresponding to acoustic pushes, as illustrated in **Figure 6.2**. Post-processing steps were implemented in MATLAB (Version 2018a, The MathWorks, Natick, MA, USA).

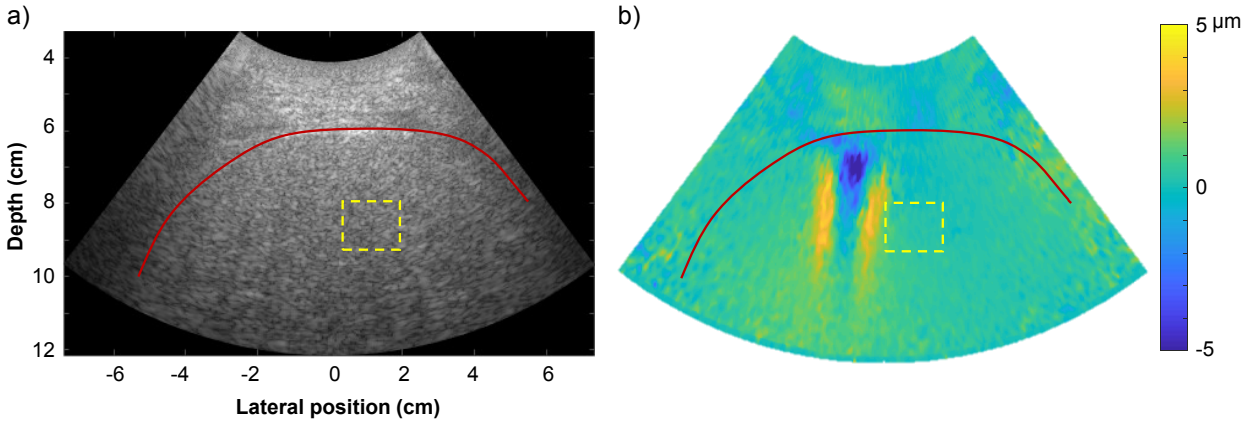

Figure 6.2 45-year-old man with biopsy-proven steatosis grade 3, lobular inflammation grade 2, ballooning grade 1, and fibrosis stage 2. **(a)** B-mode image of the liver and **(b)** shear wave propagation in the liver. The liver capsule is indicated by a curved red line and the region of interest for quantitative shear wave ultrasound measurements is shown as a yellow rectangle.

6.4.5 Shear wave speed (SWS)

The velocity field was averaged over depth z within the selected ROI to estimate the SWS (i.e., phase velocity that depends on frequency in m/s), as described in [163]. The phase velocity was computed over an a priori estimated bandwidth (67 to 110 Hz) corresponding to the range between the lower bound of the full width at half-maximum and peak frequency of the SW amplitude spectrum. The SWS estimation was performed by computing the slope of the linear fit of the phase velocity as a function of the lateral position x, as in the following equation:

$$SWS = \frac{\omega \Delta x}{\Delta \varphi}, \qquad (6.1)$$

where ω is the SW angular frequency (radian/s), and $\Delta\varphi$ is the phase difference (radian) after the wave has travelled a distance Δx (m) [163]. The goodness-of-fit of the phase velocity linear function was evaluated for each SW acquisition using the coefficient of determination (R^2) [188, 247]. SWS estimates with values R^2 below 0.9 were not considered. For each subject, SWSs were averaged to a single value using estimates from different angles and acquisitions.

6.4.6 Shear wave attenuation (SWA)

The revisited frequency-shift method (R-FS) was used to estimate SWA (Np/m/Hz) [233]. With this method, the SW amplitude spectrum at a lateral position x_0 was fitted by a gamma distribution function as follow:

$$|S(f)| \propto f^k e^{f\beta}, \qquad (6.2)$$

where f, k, and β are the SW frequency (Hz), shape and rate parameters (no units) of the gamma distribution, respectively. The frequency spectrum at a location $x_0+\Delta x$ can then be written as:

$$|S(f)| \propto f^k e^{f(\beta+\alpha\Delta x)}. \qquad (6.3)$$

The slope of the varying rate parameter $\beta(\Delta x)$ with respect to Δx represents the SWA coefficient (α). Both shape and rate parameters of this function were assumed as non-constant parameters [29, 233]. An adaptive random sample consensus (A-RANSAC) method was used for the line fitting [233]. SWA values with R^2 below 0.9 were not considered. Remaining values over angles and acquisitions were averaged.

6.4.7 Shear wave speed dispersion (SWD)

The frequency dispersion of the SWS (m/s/kHz) was measured over the bandwidth of 67 to 110 Hz, as in [34, 243]. In our study, the A-RANSAC line fitting method [233] was used to find the slope of the SWS versus frequency.

6.4.8 Young's modulus

The Young's modulus (E in kPa) was computed using the SW phase velocity:

$$E = 3\rho c^2, \qquad (6.4)$$

where ρ and c are the tissue mass density (assumed at 1050 kg/m3) and the SWS (m/s) at the peak frequency of 110 Hz, respectively. This equation assumes the liver as elastic and incompressible [34].

6.4.9 Shear modulus

The magnitude of the shear modulus ($|G|$ in kPa) was computed by assuming the liver as a linear and isotropic viscoelastic medium [158] using:

$$|G(\omega)| = |G'(\omega) + iG''(\omega)|, \qquad (6.5)$$

where $G(\omega)$ is the complex shear modulus, ω is the angular SW frequency, G' is the storage modulus, and G'' is the loss modulus. Storage and loss moduli were computed using the SWA coefficient (α) and SWS at 110 Hz (c) [150, 158, 161], according to following equations:

$$G' = \rho\omega^2 c^2 \frac{\omega^2 - c^2\alpha^2}{(c^2\alpha^2 + \omega^2)^2}, \qquad (6.6)$$

$$G'' = \rho\omega^2 c^2 \frac{2\omega c\alpha}{(c^2\alpha^2 + \omega^2)^2}, \qquad (6.7)$$

6.4.10 Viscosity

A linear frequency dependency hypothesis was assumed to compute the dynamic viscosity (Pa.s) [37, 158], using:

$$\eta = \frac{G''}{\omega}, \qquad (6.8)$$

6.4.11 Histology of tissue samples

Histopathology was used as the reference standard for all patients with NAFLD or NASH. For each patient, the liver biopsy specimen was placed in 10% formalin solution and tissue sections were processed with hematoxylin & eosin, Masson's trichrome, and sirius red staining. Histology slides were assessed by a liver pathologist [initials withheld to preserve blinding] according to the NASH Clinical Research Network scoring system [32]. The scoring included the steatosis grade from 0 to 3 (S0 to S3), lobular inflammation grade from 0 to 3 (I0 to I3), hepatocellular ballooning from 0 to 2 (B0 to B2), and fibrosis stage from 0 to 4 (F0 to F4).

6.4.12 Statistical analyses

Statistical analyses were done using software R (version x64 4.2.1, R Foundation). The mean and standard deviation (SD) of SWE parameters were reported in a constant ROI. Linear regression analyses between 2 visits were provided for each viscoelastic parameter. As recommended by the Quantitative Imaging Biomarkers Alliance ® (QIBA) [248], the following metrics were computed: intraclass correlation coefficient (ICC), bias, standard deviation (SD), limits of agreement (LOA), within-subject coefficient of variation (CV), and coefficient of reproducibility (RDC). The Bland-Altman analysis was used to determine the bias and 95% LOA between the first and second visits for all study participants. Scatterplots and Bland-Altman plots were produced.

6.5 Results

6.5.1 Patient characteristics

Patient characteristics are summarized in **Table 6.1**. Twenty subjects were included: ten were normal volunteers and ten had suspected or known NAFLD (10 women, 10 men; age range: 25.2 to 76.0 years).

Volunteers had an average body mass index (BMI) of 22.0 ± 1.7 (range: 18.8 to 24.8), whereas patients had values of 29.3 ± 3.4 (24.9 to 36.2). The mean and standard deviation of the time interval between first and second US exams were 16.6 ± 6.1 days (range: 13 to 40 days).

Table 6.1 Study Population Characteristics.

Characteristic	Results
Sex	
Male (%)	10 (50)
Female (%)	10 (50)
Adults (# (%))	20 (100)
Age (y)	
Mean ± SD	45.3 ± 16.9
(range)	(25.3 - 76.0)
BMI (kg/m^2)	
Volunteers: mean ± SD	22.0 ± 1.7
Patients: mean ± SD	29.3 ± 3.3
Steatosis grade (# (%))	
0 (< 5% hepatocytes)	10 (50)
1 (5 - 33% hepatocytes)	2 (10)
2 (33 - 66% hepatocytes)	2 (10)
3 (> 66% hepatocytes)	6 (30)
Lobular inflammation grade (# (%))	
0 (no foci)	11 (55)
1 (< 2 foci per 200 x field)	5 (25)
2 (2-4 foci per 200 x field)	4 (20)
3 (> 4 foci per 200 x field)	0 (0)
Hepatocellular ballooning grade (# (%))	
0 (no ballooned cells)	11 (55)
1 (few ballooned cells)	7 (35)
2 (many ballooned cells or prominent ballooning)	2 (10)
Fibrosis stage (# (%))	
0 (none)	12 (60)
1 (perisinusoidal or periportal)	3 (15)
2 (perisinusoidal and periportal)	2 (10)
3 (bridging fibrosis)	3 (15)
4 (cirrhosis)	0 (0)
NAS (# (%))	
0	10 (50)
1	1 (5)
2	0 (0)
3	0 (0)
4	2 (10)
5	3 (15)
6	4 (20)
7	0 (0)
8	0 (0)

Note—Steatosis grade, lobular inflammation grade, hepatocellular ballooning grade, and fibrosis stage were presumed to be 0 for the 10 healthy volunteers without steatosis. NAS = nonalcoholic fatty liver disease activity score.

6.5.2 Reproducibility

Figure 6.3 shows plots of SWS, SWA, SWD, E, $|G|$, and viscosity for first and second visits of all study participants, along with a comparison of parameters for pooled data between visits and groups. No differences were observed between visits for all viscoelastic parameters, and all viscoelastic parameters of volunteers and patients were statistically significant different in each visit. Based on this figure, values for NASH cases were higher than volunteers for all parameters.

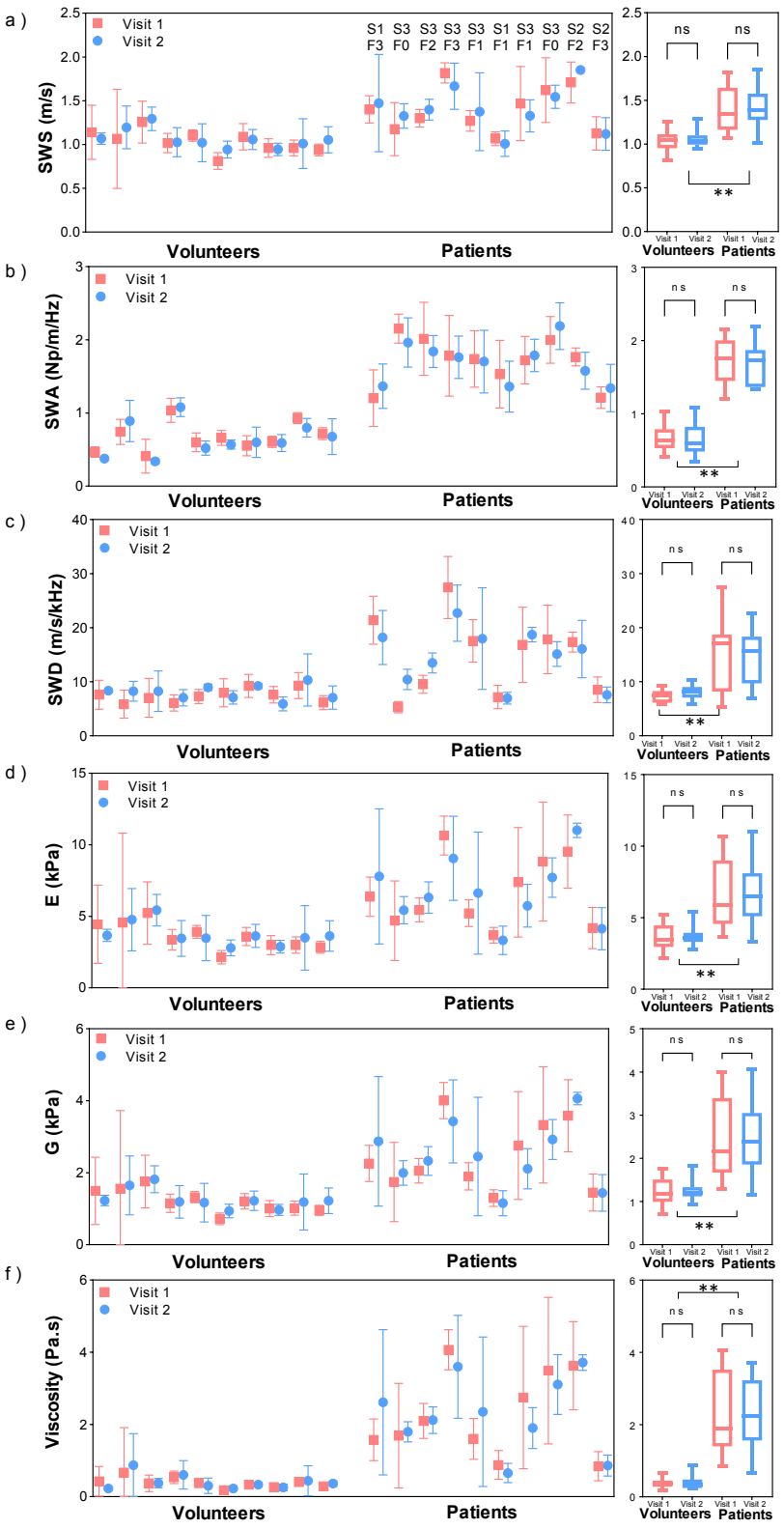

Figure 6.3 Boxplots of **a)** shear wave speed (SWS), **b)** shear wave attenuation (SWA), **c)** shear wave dispersion (SWD), **d)** Young's modulus, **e)** shear modulus, and **f)** viscosity. The left boxes

represent the mean and standard deviation of viscoelastic parameters of the first (red) and second (blue) visits for volunteers and patients. The right boxes represent the boxplots of the first and second visits for volunteers and patients (p values based on two-way ANOVA, **: $p < 0.01$, ns: not significant). S and F in panel a) respectively represent the steatosis grade and fibrosis stage according to liver biopsy.

Figure 6.4 presents ranges of SW viscoelastic parameters between visits with linear regression analyses that include the coefficient of determination (R^2) and ICC values. Slopes of linear regressions varied between 0.79 to 0.97 ($p < 0.0001$) with x-axis zero crossing differing from zero for most parameters. Coefficients of determination indicating the goodness of line fitting were $R^2 > 0.85$. The ICCs of all computed parameters varied from 0.91 to 0.97, indicated excellent reliability.

Figure 6.5 shows the Bland-Altman analysis of each parameter. Biases between visits were not significant for all measures. Coefficients of variation between visits 1 and 2 were 7.9%, 9.8%, 21.4%, 17.7%, 18.4%, and 29.8%.

Table 6.2 summarizes all performed reproducibility analyses of SW viscoelastic parameters. The reproducibility coefficients between visits were 21.8%, 27.2%, 59.2%, 49.0%, 50.9%, and 82.5% for the SWS, SWA, SWD, E, G, and viscosity, respectively.

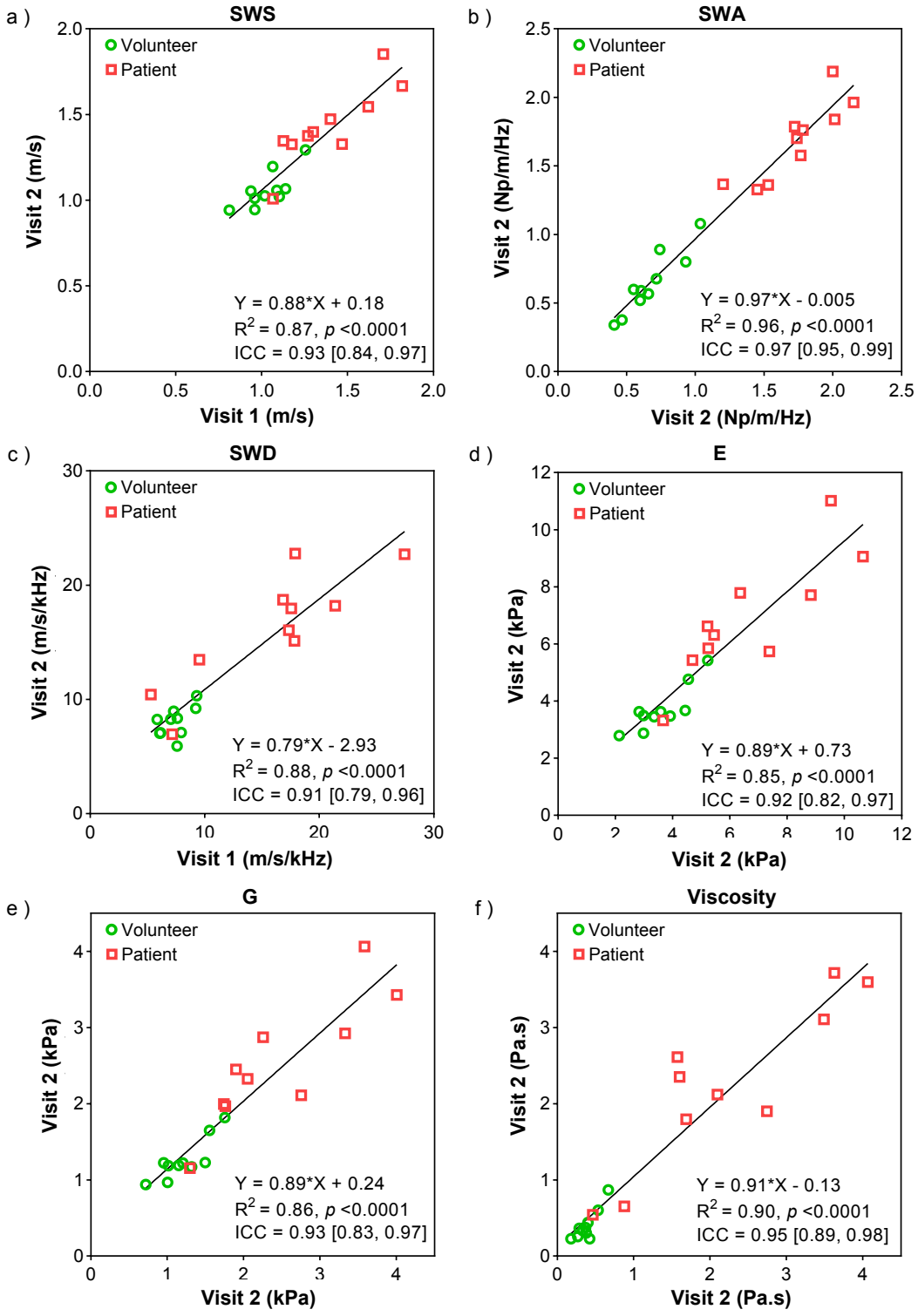

Figure 6.4 Scatterplots with linear regressions and intra-class correlations of first and second visits for **a)** shear wave speed (SWS), **b)** shear wave attenuation (SWA), **c)** shear wave dispersion (SWD), **d)** Young's modulus, **e)** shear modulus, and **f)** viscosity.

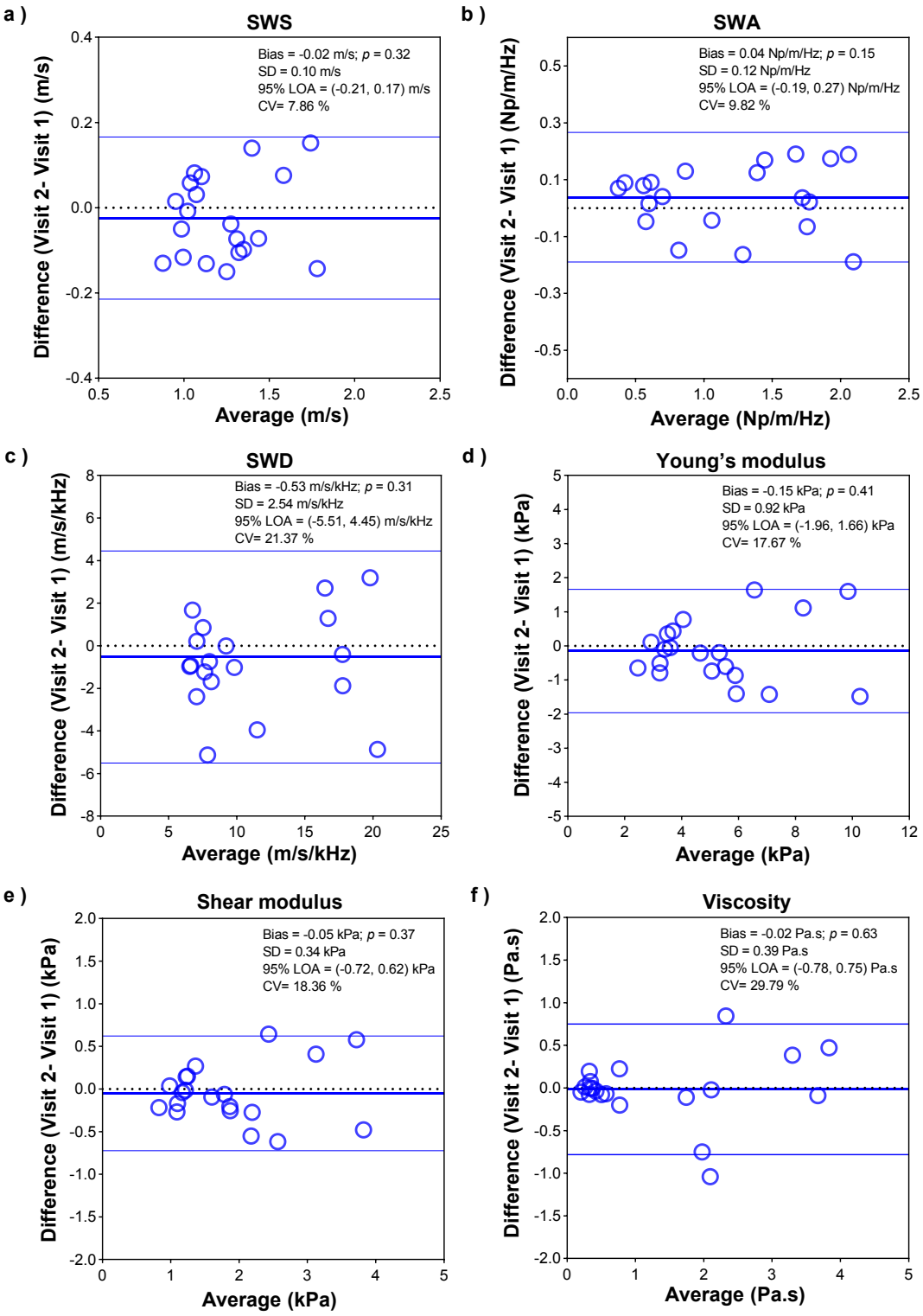

Figure 6.5 Bland-Altman plots of viscoelastic parameters based on first and second visits for **a)** shear wave speed (SWS), **b)** shear wave attenuation (SWA), **c)** shear wave dispersion (SWD), **d)** Young's modulus, **e)** shear modulus, and **f)** viscosity.

Table 6.2 Reproducibility of shear wave viscoelastic parameters in 20 participants.

	Linear Regression Analysis	ICC [95% CI]	Bland-Altman Analysis		CV (%)	RDC (%)
			Bias ± SD	95% LOA		
Shear wave speed	Y = 0.88 X + 0.11, R^2 = 0.87, p < 0.0001	0.93 [0.84, 0.97]	-0.02 ± 0.10 (m/s) (p = 0.32)	(-0.21,0.17) (m/s)	7.9	21.83
Shear wave attenuation	Y = 0.97 X - 0.005, R^2 = 0.96, p < 0.0001	0.97 [0.95, 0.99]	0.04 ± 0.12 (Np/m/Hz) (p = 0.15)	(-0.19,0.27) (Np/m/Hz)	9.8	27.20
Shear wave dispersion	Y = 0.79 X - 2.93, R^2 = 0.88, p < 0.0001	0.91 [0.79, 0.96]	-0.52 ± 2.54 (m/s/kHz) (p = 0.31)	(-5.51,4.45) (m/s/kHz)	21.4	59.19
Young's modulus	Y = 0.89 X + 0.73, R^2 = 0.85, p < 0.0001	0.92 [0.82, 0.97]	-0.15 ± 0.92 (kPa) (p = 0.41)	(-1.96,1.66) (kPa)	17.7	48.95
Shear modulus	Y = 0.89 X + 0.24, R^2 = 0.86, p < 0.0001	0.93 [0.84, 0.97]	-0.05 ± 0.34 (kPa) (p = 0.37)	(-0.72,0.62) (kPa)	18.4	50.86
Viscosity	Y = 0.91 X - 0.13, R^2 = 0.90, p < 0.0001	0.95 [0.89, 0.98]	-0.01 ± 0.39 (Pa.s) (p = 0.63)	(-0.78,0.75) (Pa.s)	29.8	82.52

Note—CI = confidence interval, CV = coefficient of variation, ICC = intraclass correlation coefficient, LOA = limits of agreement, RDC = reproducibility coefficient, and SD = standard deviation.

6.6 Discussion

This prospective study assessed the reproducibility of SW viscoelastic measurements of the liver for two visits in volunteers and patients with diagnosed NAFLD. Results revealed excellent reproducibility between visits. The SWS, Young's modulus and shear modulus describe the stiffness of the liver [158, 184] , whereas SWA, SWD and viscosity are related to its lossy nature [20, 27, 153, 164] .

The mean SWSs were higher in patients than volunteers. SWSs for volunteers were within the range of values reported for healthy human livers (1.16 ± 0.14 m/s) [249] and results for patients were consistent with [250], where a threshold of 1.33 m/s was considered for NASH detection.

Similar trends were observed for the Young's modulus. Young's moduli reported in the literature for healthy livers were within the range of 2.6 to 6.2 kPa [54], and based on another study [251] , the Young's modulus of 6.3 kPa was the threshold for detection of significant fibrosis ($F \geq 2$) in NAFLD patients. The shear modulus is not a standard parameter reported in the literature but by assuming the liver as an isotropic material, $G = E/3$.

There were no statistical differences between the two visits for the SWS, Young's modulus, and shear modulus. Furthermore, values in patients were higher compared to volunteers. Between visits CVs of the SWS were consistent with the reported range of 6.9 - 8.1 % of supersonic imaging [201]. The SWS had a lowest RDC compared with the Young's and shear moduli. According to Equation 6.2, SWS is related to the Young's modulus by a power of two. Thus, it was expected for the Young's modulus to have a higher RDC compared to the SWS. Furthermore, as both SWS and SWA are used to compute the shear modulus (Equations 6.5-6.7), that could be the reason for the high RDC compared with SWS and the Young's modulus.

SWAs obtained for all subjects were consistent with the literature [164, 176] , with patients having higher attenuation compared to volunteers. The SWA revealed a good reproducibility between visits with a CV of 9.8%. There was no significant difference between visits, and the linear regression showed a slope close to unity. Therefore, SWA may be considered as a valuable parameter with diagnostic capability for NAFLD.

On the other hand, SWD and viscosity also showed excellent ICC between the two visits, and higher values in patients, as in [122]. Mean SWDs for volunteers were in agreement with values reported in the literature (10.24 ± 1.65 m/s/kHz)) [250]. However, different values of liver viscosity are given in the literature, depending on which rheological model was used to describe the liver [122]. Nevertheless, viscosities obtained in this study agreed with values reported when assuming linear viscoelasticity (Voigt model) [122]. The Voigt model has been shown to correspond to a lower viscosity compared to other models, such as the Spring-Pot [252].

CVs for SWA and SWD between visits were less than those observed for the viscosity, which may be due to the fact that viscosity is determined from both variables (Equations 6.7 and 6.8). In this study, all parameters defining the lossy nature of the liver had coefficients of variation below 30% between the two visits. SWS and SWA had lowest CVs below 10% compared with other

viscoelastic parameters. This suggests adding SWA to describe the lossy nature of the liver to the most often used SWS parameter as biomarkers for diagnosing NAFLD patients.

In summary, this study confirmed the good reproducibility of six viscoelastic parameters between two visits, with SWS and SWA being the most robust. This study has some limitations. First, the total number of cases is limited. Due to the limited sample size, we were unable to analyze all possible combinations of biopsy grades. Future research should also assess other components, such as the scanner and sonographer reproducibility. Second, subjects involved in this study did not have fibrosis stage 4 and inflammation grade 3. Third, time intervals between the two visits for each participant were different and varied approximately from 2 weeks to 6 weeks due to the COVID-19 pandemic. Thus, a study based on a larger dataset may provide a more accurate picture of reproducibility of these parameters. Fourth, this study was conducted at a single site and would require external validation of results at multiple sites.

6.7 Conclusion

This study establishes good reproducibility of results for SWS, SWA, SWD, Young modulus, shear modulus, and viscosity as viscoelastic parameters between two visits in volunteers and patients with NASH. Among the three parameters representing liver's stiffness, SWS provided the best reproducibility. Among the three parameters representing liver's lossy nature, SWA provided the best reproducibility. Given promising reproducibility for clinical assessment of NAFLD, future studies may prospectively assess the cost-effectiveness of using these methods for assessing viscoelastic parameters in those patients. More datasets would be needed to confirm reproducibility of viscoelastic parameters.

6.8 Funding information

This work was supported in part by the Natural Sciences and Engineering Research Council of Canada under Grant 2022-03729, in part by the Canadian Institutes of Health Research under Grant 389385, and in part by the Oncotech consortium (Oncopole, Medteq, Transmedtech, Cancer Research Society, Fonds de Recherche Santé du Québec, and Siemens Healthcare) under Grant 293741. Salary award by the Fonds de recherche du Québec en Santé and Fondation de l'association des radiologistes du Québec (FRQS-FARQ #298509) to An Tang.

6.9 Disclosures

Giada Sebastiani has acted as speaker for Pfizer, Merck, Novonordisk, Novartis, Gilead, and AbbVie; served as an advisory board member for Merck, Gilead, Pfizer, Allergan, Novonordisk, Intercept, and Novartis; and has received unrestricted research funding from Theratechnologies Inc. An Tang and Guy Cloutier have received equipment loans and grant funding supports from Siemens Healthcare.

Chapter 7 – Discussion and general conclusion

7.1 General summary

In this thesis, we presented a series of accomplishments, from algorithm development to experimental validations, to provide a potential biomarker for diagnosing NAFLD.

In the first article of this thesis (Chapter 4), the R-FS method for SWA measurement was designed and implemented, and compared with three other SWA measurement methods (FS, 2P-FS, and AMUSE). They were validated with numerical phantoms (with different SNRs), *in vitro* homogenous phantoms, and *in vivo* duck liver acquisitions. The study proposed two main improvements to the FS method; firstly, the shape parameter of the gamma frequency fit on the SW attenuation spectrum was not assumed constant and equal to the shape parameter of the source spectrum, yielding high *R*-squared values of gamma fits. The second modification was to use an A-RANSAC line fitting approach to improve the robustness in the presence of outliers. For all numerical, *in vitro* homogenous phantoms, and *in vivo* duck livers, the R-FS method outperformed the FS, 2P-FS, and AMUSE methods. Another finding in this article was that the SWA increases in fatty duck livers compared to normal duck livers. Thus, as the next step of this study, the potential of the R-FS method as a diagnostic tool for NAFLD was investigated using a clinical human dataset.

As in the first article, higher SWAs were observed after the development of steatohepatitis. In the second article in this thesis (Chapter 5), the diagnostic performance of SWA using the R-FS method for detecting NAFLD was compared to biopsy, MRI-PDFF, and SWD. The study included 40 participants, 27 with NAFLD and 13 healthy volunteers. Another novelty of this article was utilizing the A-RANSAC line fitting, developed in Chapter 4, for SWD computation. As A-RANSAC was proven to be superior in the presence of many outliers, especially with the *in vivo* human dataset, it was used in both SWA and SWD computations. The results showed that SWA had low-to-high correlations with the severity of steatosis, inflammation, ballooning, and fibrosis determined by biopsy. In addition, in this pilot study, SWA demonstrated high diagnostic performance for grading liver steatosis, comparable to that of MRI-PDFF and superior to that of SWD. This article provided valuable insights into the potential use of SWA for diagnosing NAFLD and NASH. The statistically significant correlations between SWA and the severity of steatosis,

inflammation, ballooning, and fibrosis highlights the potential of this method as a noninvasive tool for assessing liver diseases. Moreover, the high diagnostic performance of SWA for grading liver steatosis, as shown by the comparable results to those of MRI-PDFF, suggests that SWA may be a valuable alternative to MRI-PDFF for diagnosing NAFLD.

In the third article of this thesis (Chapter 6), we focused on assessing the reproducibility of various viscoelastic parameters related to liver stiffness and its lossy nature in healthy volunteers and patients with biopsy-proven NAFLD between a first and a second visit of participants. This study included 20 subjects, with ten volunteers and ten patients, comprising equal numbers of women and men aged between 25.2 to 76.0 years. The time interval between the first and second ultrasound exams was 16.6 ± 6.1 days for all participants. The results showed no significant differences between the first and second visits for all viscoelastic parameters. However, values for NAFLD cases were higher than for volunteers for all parameters. The ICCs of all computed parameters varied from 0.91 to 0.97, indicating excellent reliability. Bias values between visits were not statistically significant for all measures, and coefficients of variation between visits ranged from 7.9% to 29.8%. Overall, the results suggested that the selected viscoelastic parameters (SWS, SWA, SWD, Young's modulus, shear modulus, and viscosity) are reproducible and reliable, even in patients with NAFLD.

7.2 Contribution and limitations

The originality of the three main chapters of this thesis was to improve and evaluate US SWE to measure viscoelastic parameters to diagnose NAFLD by ways of improving the frequency shift method to measure SWA, and it was validated in numerical and experimental setups with comparisons to other recent methods. The reproducibility of the viscoelastic parameters to detect NAFLD was also investigated.

The main contributions of the first article were improvements to the FS and 2P-FS methods for SW attenuation computation, and the provision of robust attenuation maps that can be utilized for medical diagnosis of steatotic livers. This study reported a comprehensive comparative analysis of R-FS, 2P-FS, and FS methods. The R-FS model provided robust estimation of the attenuation coefficient, and it outperformed other imaging methods with simulations, *in vitro,* and *in vivo* datasets. Another novel contribution of this study was the development of the A-RANSAC

technique, which exhibits the autonomous capacity to establish a unique threshold for each dataset by leveraging the inliers present within the data to be analyzed, allowing for the exclusion of erroneous measurements. The use of a varying shape parameter and the A-RANSAC line fitting allowed for such improvements over FS and 2P-FS methods. Another contribution of this study was to make noisy numerical phantoms with low-to-high SNR values to validate R-FS. The R-FS model overcame the limitations of other imaging methods and provided a robust estimation of the attenuation coefficient, which was validated by comparing results with theoretical KV and AMUSE estimations. **Table 7.1** presents the strengths and limitations of the utilized methods.

Table 7.1 Strengths and limitations of revisited frequency shift (R-FS), two point frequency shift (2P-FS), frequency shift (FS), and attenuation measuring ultrasound shear wave elastography (AMUSE) methods.

Methods	Strengths	Limitations
R-FS	Less variances specially with *in vivo* data, closer mean value to ground truth and AMUSE value (low biases) compared to FS and 2P-FS even within larger ROIs, and able to provide images (or maps) of shear wave attenuation	Assumption of locally isotropic and homogeneous media, and more computation time than 2P-FS and AMUSE
2P-FS	Less computation time, less bias values, and variances than FS in some datasets, and able to provide images of shear wave attenuation	Assumption of locally isotropic and homogeneous media, limitation in the case of selecting the two points and showed higher variances in more viscous media or in the presence of more fat in duck livers
FS	Proposed earlier than the other methods, which was improved to develop 2P-FS and R-FS methods	Assumption of locally isotropic and homogeneous media, high bias values, and higher variances with *in vivo* cases
AMUSE	Faster than other methods as it just provides a single value close to the gold standard (liver biopsy)	Assumption of locally isotropic and homogeneous media, does not provide images of shear wave attenuation, and sensitive to the selection of the frequency range

The main contribution of the second article was the evaluation of shear wave attenuation (SWA) imaging as a biomarker for assessing hepatic steatosis, lobular inflammation, ballooning, and fibrosis in the liver, using histopathology as the reference standard. We compared the

performance of SWA to other biomarkers, such as MRI-PDFF and SWD. We found that SWA provided high diagnostic performance for the classification of dichotomized steatosis grades and could differentiate histologically determined steatosis grades with good sensitivity and high specificity. The study also demonstrated that SWA had better performance than SWD and similar performance to MRI-PDFF for steatosis grading. Therefore, this study showed that SWA has the potential to be implemented on US scanners, is cost-effective, and available as a point-of-care tool for screening liver steatosis. This study's limitations include the relatively low number of patients and some combinations of histopathological features not being available, which may affect the diagnostic performance assessment.

The contribution of the third article lied in the confirmation of the reproducibility of the six viscoelastic parameters selected for diagnosing NAFLD. This study also provided information on the range of values for these parameters in healthy livers and NAFLD patients. Furthermore, the study suggested that the SWS and SWA are the most robust and could be utilized as biomarkers for diagnosing NASH patients, and for staging fibrosis and steatosis, respectively. Furthermore, this study provided reference values for the six viscoelastic parameters analyzed in healthy volunteers and NAFLD patients, which can be used as a baseline for future studies. We provided an interpretation of the results based on the previous studies. However, the study had several limitations. First, the sample size is limited, which prevented a comprehensive analysis of the parameters through all combinations of histopathological grades. The study only included patients with NAFLD and did not include patients with advanced fibrosis or inflammation, limiting the generalizability of the findings. Second, the time intervals between visits varied due to the COVID-19 pandemic, which may have influenced the reproducibility of the parameters. Finally, the study was conducted at a single site and requires external validation of the results at multiple sites.

7.3 Future works

Future works should first address the limitations of this thesis. The R-FS method could be implemented in a user-friendly software that clinicians and researchers can use for SWA mapping. The software should be easy to use and have a graphical user interface allowing users to interact with the data, select ROIs and obtain attenuation maps. The feasibility of the SWA implementation on US scanners as a point-of-care tool for screening liver steatosis needs to be investigated. This might be done with our commercial partner, Siemens Healthcare, but obtaining SWA maps with

Siemens Sequoia datasets instead of Verasonics datasets would need first to be explored. Although the R-FS method was validated on numerical phantoms, *in vitro* and *in vivo* datasets, the datasets were relatively small.

Further validation on larger datasets would confirm the proposed method's robustness and accuracy. Also, the validation of SWA as an alternative to MRI-PDFF for the assessment of liver steatosis in larger cohorts of patients with NAFLD is needed. Another suggested future work is investigating the correlation between SWA and histopathological features such as ballooning, lobular inflammation, and fibrosis in larger patient cohorts to determine the diagnostic potential of SWA for these conditions. Also, the diagnostic performance of SWA in patients with different degrees of steatosis and fibrosis severity, as well as in patients with comorbidities such as diabetes or obesity, can be assessed. It would be of interest to explore SWA maps in the case of liver cancer assessment. The R-FS method utilizes the assumption of homogeneity in the liver. It might be applied to liver cancer by taking two regions of interest (ROIs), one inside and the other outside the tumor. This would allow comparing different SWA values in presumably more homogeneous regions. The method could also be applied to other organs affected by various diseases, such as breast cancer detection and characterization.

The evaluation of the potential of SWA for monitoring the progression and/or regression of liver steatosis over time in response to lifestyle modifications or pharmacological interventions would be of interest. Another future work is investigating the diagnostic performance of SWA in patients with other liver diseases, such as viral hepatitis, alcoholic liver disease, or autoimmune liver diseases, to assess the specificity of SWA. Another essential future work will be comparing the performance of the latest SWA technologies and QUS-based techniques on the same patients with NAFLD to identify the most effective and accurate methods for assessing liver steatosis.

To confirm the diagnostic capabilities of SWA and other viscoelastic parameters assessed in Chapter 6, validation studies should be conducted with a larger cohort of NAFLD patients with all combinations of different steatosis, inflammation, ballooning grades, and fibrosis stages. Future studies should assess inter-scanner reproducibility to understand whether the observed variations are due to the scanner or the sonographer. Also, future studies can address the effects of time intervals on reproducibility by having a larger dataset and more frequent and uniform intervals between visits. To improve reproducibility, there is a need for standardized techniques and

protocols for acquiring and analyzing SW viscoelastic measurements. Future studies should focus on developing and validating standardized protocols for this purpose. Chapter 6's findings may be helpful to future studies assessing the effectiveness of treatments for NAFLD and other liver diseases. However, further studies with larger sample sizes and more extended follow-up periods are required to confirm the reproducibility and reliability of these parameters.

7.4 General conclusion

In summary, this thesis demonstrated promising advancements for the noninvasive diagnosis and assessment of liver pathologies, particularly NAFLD. The proposed R-FS method offered a robust and accurate approach for computing the shear wave attenuation coefficient, which could lead to improved viscoelasticity imaging in biological tissues and provide robust biomarkers for diagnosing fatty livers and other organ pathologies. The pilot clinical study on SWA demonstrated its feasibility as a noninvasive biomarker for the early detection and grading of hepatic steatosis, showing a high sensitivity and specificity. Larger prospective studies can help validate its diagnostic performance. Finally, the study on the reproducibility of viscoelastic parameters highlighted the robustness and reproducibility of the proposed SWE methods for accurately measuring liver viscoelasticity, providing potential biomarkers for NAFLD. Overall, this thesis represented significant progress toward improving the diagnosis and assessment of NAFLD, which could substantially impact patient outcomes and healthcare systems worldwide.

References

[1] S. Mitra, A. De, and A. Chowdhury, "Epidemiology of non-alcoholic and alcoholic fatty liver diseases," *Translational Gastroenterology and Hepatology,* vol. 5, no. 16, pp. 16-33, 2019.

[2] "Canadian Liver Foundation," *Canadian Liver Foundation,* 2022.

[3] E. Fabbrini, S. Sullivan, and S. Klein, "Obesity and nonalcoholic fatty liver disease: biochemical, metabolic, and clinical implications," (in eng), *Hepatology,* vol. 51, no. 2, pp. 679-89, Feb 2010.

[4] G. Vernon, A. Baranova, and Z. M. Younossi, "Systematic review: the epidemiology and natural history of non-alcoholic fatty liver disease and non-alcoholic steatohepatitis in adults," *Alimentary pharmacology & therapeutics,* vol. 34, no. 3, pp. 274-285, 2011.

[5] Z. M. Younossi, A. B. Koenig, D. Abdelatif, Y. Fazel, L. Henry, and M. Wymer, "Global epidemiology of nonalcoholic fatty liver disease—Meta-analytic assessment of prevalence, incidence, and outcomes," vol. 64, no. 1, pp. 73-84, 2016.

[6] M. Benedict and X. Zhang, "Non-alcoholic fatty liver disease: An expanded review," (in eng), *World J Hepatol,* vol. 9, no. 16, pp. 715-732, Jun 8 2017.

[7] M. Ekstedt *et al.*, "Long-term follow-up of patients with NAFLD and elevated liver enzymes," *Hepatology,* vol. 44, no. 4, pp. 865-873, 2006.

[8] E. Martinou, M. Pericleous, I. Stefanova, V. Kaur, and A. M. Angelidi, "Diagnostic modalities of non-alcoholic fatty liver disease: from biochemical biomarkers to multi-omics non-invasive approaches," *Diagnostics (Basel),* vol. 12, no. 2, p. 407, 2022.

[9] Y. Sumida, A. Nakajima, and Y. Itoh, "Limitations of liver biopsy and non-invasive diagnostic tests for the diagnosis of nonalcoholic fatty liver disease/nonalcoholic steatohepatitis," (in eng), *World J Gastroenterol,* vol. 20, no. 2, pp. 475-85, Jan 14 2014.

[10] A. Tang *et al.*, "Accuracy of MR imaging-estimated proton density fat fraction for classification of dichotomized histologic steatosis grades in nonalcoholic fatty liver disease," (in eng), *Radiology,* vol. 274, no. 2, pp. 416-25, Feb 2015.

[11] A. Qayyum *et al.*, "Evaluation of diffuse liver steatosis by ultrasound, computed tomography, and magnetic resonance imaging: which modality is best?," (in eng), *Clinical Imaging,* vol. 33, no. 2, pp. 110-5, Mar-Apr 2009.

[12] S. R. Mehta, E. L. Thomas, J. D. Bell, D. G. Johnston, and S. D. Taylor-Robinson, "Non-invasive means of measuring hepatic fat content," (in eng), *World Journal of Gastroenterology,* vol. 14, no. 22, pp. 3476-83, Jun 14 2008.

[13] R. Hernaez *et al.*, "Diagnostic accuracy and reliability of ultrasonography for the detection of fatty liver: a meta-analysis," (in eng), *Hepatology,* vol. 54, no. 3, pp. 1082-1090, Sep 2 2011.

[14] J. F. Gerstenmaier and R. N. Gibson, "Ultrasound in chronic liver disease," (in eng), *Insights Imaging,* vol. 5, no. 4, pp. 441-55, Aug 2014.

[15] S. K. Baik, "Haemodynamic evaluation by doppler ultrasonography in patients with portal hypertension: a review," (in eng), *Liver Int,* vol. 30, no. 10, pp. 1403-13, Nov 2010.

[16] R. Sirli and I. Sporea, "Controlled attenuation parameter for quantification of steatosis: which cut-offs to use?," (in eng), *Can J Gastroenterol Hepatol,* vol. 2021, p. 6662760, 2021.

[17] K. Nightingale, "Acoustic radiation force impulse (ARFI) imaging: a review," (in eng), *Curr Med Imaging Rev,* vol. 7, no. 4, pp. 328-339, Nov 1 2011.

[18] T. J. Czernuszewicz and C. M. Gallippi, "Acoustic radiation force impulse ultrasound," in *Ultrasound Elastography for Biomedical Applications and Medicine*, 2018, pp. 334-356.

[19] M. W. Urban, "Production of acoustic radiation force using ultrasound: methods and applications," (in eng), *Expert Rev Med Devices,* vol. 15, no. 11, pp. 819-834, Nov 2018.

[20] H. Li *et al.*, "Viscoelasticity imaging of biological tissues and single cells using shear wave propagation," (in English), *Frontiers in Physics,* Review vol. 9, p. 350, 2021-June-21 2021.

[21] A. Tang, G. Cloutier, N. M. Szeverenyi, and C. B. Sirlin, "Ultrasound elastography and MR elastography for assessing liver fibrosis: part 1, principles and techniques," (in eng), *AJR Am J Roentgenol,* vol. 205, no. 1, pp. 22-32, Jul 2015.

[22] A. Tang, G. Cloutier, N. M. Szeverenyi, and C. B. Sirlin, "Ultrasound elastography and MR elastography for assessing liver fibrosis: part 2, diagnostic performance, confounders, and future directions," *American Journal of Roentgenology,* vol. 205, no. 1, pp. 33-40, 2015/07/01 2015.

[23] R. M. S. Sigrist, J. Liau, A. E. Kaffas, M. C. Chammas, and J. K. Willmann, "Ultrasound elastography: review of techniques and clinical applications," (in eng), *Theranostics,* vol. 7, no. 5, pp. 1303-1329, 2017.

[24] R. G. Barr *et al.*, "Elastography assessment of liver fibrosis: society of radiologists in ultrasound consensus conference statement," (in eng), *Radiology,* vol. 276, no. 3, pp. 845-61, Sep 2015.

[25] J. L. Gennisson, T. Deffieux, M. Fink, and M. Tanter, "Ultrasound elastography: principles and techniques," (in eng), *Diagn Interv Imaging,* vol. 94, no. 5, pp. 487-95, May 2013.

[26] M. Friedrich-Rust *et al.*, "Liver fibrosis in viral hepatitis: noninvasive assessment with acoustic radiation force impulse imaging versus transient elastography," (in eng), *Radiology,* vol. 252, no. 2, pp. 595-604, Aug 2009.

[27] M. Bhatt *et al.*, "Reconstruction of Viscosity Maps in Ultrasound Shear Wave Elastography," (in eng), *IEEE Trans Ultrason Ferroelectr Freq Control,* Apr 11 2019.

[28] S. Bernard, S. Kazemirad, and G. Cloutier, "A frequency-shift method to measure shear-wave attenuation in soft tissues," *IEEE Transactions on Ultrasonics, Ferroelectrics, and Frequency Control,* vol. 64, no. 3, pp. 514-524, 2017.

[29] P. Kijanka and M. W. Urban, "Two-point frequency shift method for shear wave attenuation measurement," (in eng), *IEEE Transactions on Ultrasonics, Ferroelectrics, and Frequency Control,* vol. 67, no. 3, pp. 483-496, Mar 2020.

[30] M. A. Fischler and R. C. Bolles, "Random sample consensus: a paradigm for model fitting with applications to image analysis and automated cartography," vol. 24, no. 6 %J Commun. ACM, pp. 381–395, 1981.

[31] I. Z. Nenadic *et al.*, "Attenuation measuring ultrasound shearwave elastography and in vivo application in post-transplant liver patients," (in eng), *Physics in Medicine and Biology,* vol. 62, no. 2, pp. 484-500, Jan 21 2017.

[32] D. E. Kleiner *et al.*, "Design and validation of a histological scoring system for nonalcoholic fatty liver disease," (in eng), *Journal of Hepatology,* vol. 41, no. 6, pp. 1313-21, Jun 2005.

[33] E. Herrmann *et al.*, "Assessment of biopsy-proven liver fibrosis by two-dimensional shear wave elastography: An individual patient data-based meta-analysis," (in eng), *Hepatology,* vol. 67, no. 1, pp. 260-272, Jan 2018.

[34] C. T. Barry *et al.*, "Shear Wave dispersion measures liver steatosis," *Ultrasound in Medicine and Biology,* vol. 38, no. 2, pp. 175-182, 2012/02/01/ 2012.

[35] J. Fu, B. Wu, H. Wu, F. Lin, and W. Deng, "Accuracy of real-time shear wave elastography in staging hepatic fibrosis: a meta-analysis," (in eng), *BMC Med Imaging,* vol. 20, no. 1, p. 16, Feb 11 2020.

[36] W. Zhang, Y. Zhu, C. Zhang, and H. Ran, "Diagnostic accuracy of 2-dimensional shear wave elastography for the staging of liver fibrosis: a meta-analysis," (in eng), *Ultrasound in Medicine and Biology,* vol. 38, no. 3, pp. 733-740, Mar 2019.

[37] M. Bhatt *et al.*, "Multiparametric in vivo ultrasound shear wave viscoelastography on farm-raised fatty duck livers: human radiology imaging applied to food sciences," (in eng), *Poult Sci,* vol. 100, no. 4, p. 100968, Apr 2021.

[38] S. McPherson, T. Hardy, E. Henderson, A. D. Burt, C. P. Day, and Q. M. Anstee, "Evidence of NAFLD progression from steatosis to fibrosing-steatohepatitis using paired biopsies: implications for prognosis and clinical management," (in eng), *Journal of Hepatology,* vol. 62, no. 5, pp. 1148-55, May 2015.

[39] J. B. Furness, E. K. Boyle, J. Fakhry, J. Gajewski, and L. J. Fothergill, "Digestive System," in *Oxford Handbook of Evolutionary Medicine*, M. Brüne and W. Schiefenhövel, Eds.: Oxford University Press, 2019, pp. 530–562.

[40] G. Y. Wu, *Clinical gastroenterology*. [Online]. Available: http://www.springer.com/series/7672.

[41] W.-X. D. and and X.-M. Yin, *Cellular injury in liver diseases.* Springer, 2017.

[42] M. Van Haele, J. Snoeck, and T. Roskams, "Human liver regeneration: an etiology dependent process," (in eng), *Int J Mol Sci,* vol. 20, no. 9, May 10 2019.

[43] J. M. Llovet *et al.*, "Hepatocellular carcinoma," *Nature Reviews Disease Primers,* vol. 7, no. 1, p. 6, 2021/01/21 2021.

[44] M. M. Asfari, M. Talal Sarmini, M. Alomari, R. Lopez, S. Dasarathy, and A. J. McCullough, "The association of nonalcoholic steatohepatitis and hepatocellular carcinoma," (in eng), *Eur J Gastroenterol Hepatol,* vol. 32, no. 12, pp. 1566-1570, Dec 2020.

[45] J. C. Cohen, J. D. Horton, and H. H. Hobbs, "Human fatty liver disease: old questions and new insights," (in eng), *Science,* vol. 332, no. 6037, pp. 1519-23, Jun 24 2011.

[46] J. C. J. C. Perazzo, *Chronic liver disease : from molecular biology to therapy* (Hepatology Research and Clinical Developments). 2017.

[47] M. Benedict and X. Zhang, "Non-alcoholic fatty liver disease: An expanded review," *World Journal of Hepatology,* vol. 9, p. 715, 06/01 2017.

[48] K. A. McGlynn, J. L. Petrick, and H. B. El-Serag, "Epidemiology of Hepatocellular Carcinoma," vol. 73, no. S1, pp. 4-13, 2021.

[49] D. Q. Huang *et al.*, "Global epidemiology of cirrhosis — aetiology, trends and predictions," *Nature Reviews Gastroenterology & Hepatology,* 2023/03/28 2023.

[50] J. Maurice and P. Manousou, "Non-alcoholic fatty liver disease," (in eng), *Clin Med (Lond),* vol. 18, no. 3, pp. 245-250, Jun 2018.

[51] G. S. Mark *et al.*, "Burden of nonalcoholic fatty liver disease in Canada, 2019–2030: a modelling study," *CMAJ Open,* vol. 8, no. 2, p. E429, 2020.

[52] C. Lackner, "Hepatocellular ballooning in nonalcoholic steatohepatitis: the pathologist's perspective," *Expert Review of Gastroenterology & Hepatology,* vol. 5, no. 2, pp. 223-231, 2011/04/01 2011.

[53] M. Naim Ibrahim, "Automated Fatty Liver Disease Detection in Point-of-Care Ultrasound B-mode Images," MSc, School of Engineering, University of Guelph, Ontario, Canada, 2022.

[54] Y. Qu *et al.*, "Diagnostic performance of FibroTouch ultrasound attenuation parameter and liver stiffness measurement in assessing hepatic steatosis and fibrosis in patients with nonalcoholic fatty liver disease," (in eng), *Clin Transl Gastroenterol,* vol. 12, no. 4, p. e00323, Apr 13 2021.

[55] R. Parker *et al.*, "Natural history of histologically proven alcohol-related liver disease: A systematic review," *Journal of Hepatology,* vol. 71, no. 3, pp. 586-593, 2019/09/01/ 2019.

[56] Z. M. Younossi *et al.*, "Nonalcoholic steatofibrosis independently predicts mortality in nonalcoholic fatty liver disease," *Hepatology communications,* vol. 1, no. 5, pp. 421-428, 2017.

[57] I. L. Nalbantoglu and E. M. Brunt, "Role of liver biopsy in nonalcoholic fatty liver disease," (in eng), *World J Gastroenterol,* vol. 20, no. 27, pp. 9026-37, Jul 21 2014.

[58] H. E. Xu and J. Guo, "All about NASH: disease biology, targets, and opportunities on the road to NASH drugs," *Acta Pharmacologica Sinica,* vol. 43, no. 5, pp. 1101-1102, 2022/05/01 2022.

[59] E. Hughes, L. J. Hopkins, and R. Parker, "Survival from alcoholic hepatitis has not improved over time," *PLOS ONE,* vol. 13, no. 2, p. e0192393, 2018.

[60] L. A. Adams and V. Ratziu, "Non-alcoholic fatty liver - Perhaps not so benign," *Journal of Hepatology,* vol. 62, no. 5, pp. 1002-1004, 2015.

[61] F. Xia, L. Zeng, X. R. Yao, and B. J. Zhou, "Chapter 3 - Hepatic apoptosis and necrosis: mechanisms and clinical relevance," in *Liver Pathophysiology*, P. Muriel, Ed. Boston: Academic Press, 2017, pp. 47-60.

[62] R. Lomonaco *et al.*, "Advanced liver fibrosis Is common in patients with type 2 diabetes followed in the qutpatient setting: the need for systematic screening," (in eng), *Diabetes Care,* vol. 44, no. 2, pp. 399-406, Feb 2021.

[63] A. Smith, K. Baumgartner, and C. Bositis, "Cirrhosis: diagnosis and management," (in eng), *Am Fam Physician,* vol. 100, no. 12, pp. 759-770, Dec 15 2019.

[64] X. Zhang, G. L. Wong, and V. W. Wong, "Application of transient elastography in nonalcoholic fatty liver disease," (in eng), *Clin Mol Hepatol,* vol. 26, no. 2, pp. 128-141, Apr 2020.

[65] L. Petitclerc, G. Sebastiani, G. Gilbert, G. Cloutier, and A. Tang, "Liver fibrosis: Review of current imaging and MRI quantification techniques," *Journal of magnetic resonance imaging : JMRI,* vol. 45, 12/16 2016.

[66] R. Bataller and D. A. Brenner, "Liver fibrosis," (in eng), *J Clin Invest,* vol. 115, no. 2, pp. 209-18, Feb 2005.

[67] L. Petitclerc, G. Gilbert, B. N. Nguyen, and A. Tang, "Liver fibrosis quantification by magnetic resonance imaging," (in eng), *Top Magn Reson Imaging,* vol. 26, no. 6, pp. 229-241, Dec 2017.

[68] A. S. and M. N., *Liver imaging*. StatPearls [Internet]. Treasure Island (FL): StatPearls Publishing, 2022.

[69] S. J. Forbes and P. N. Newsome, "Liver regeneration - mechanisms and models to clinical application," (in eng), *Nat Rev Gastroenterol Hepatol,* vol. 13, no. 8, pp. 473-85, Aug 2016.

[70] V. Pandyarajan, R. G. Gish, N. Alkhouri, and M. Noureddin, "Screening for nonalcoholic fatty liver disease in the primary care clinic," (in eng), *Gastroenterol Hepatol (N Y),* vol. 15, no. 7, pp. 357-365, Jul 2019.

[71] A. D. Burt, C. Lackner, and D. G. Tiniakos, "Diagnosis and assessment of NAFLD: definitions and histopathological classification," (in eng), *Semin Liver Dis,* vol. 35, no. 3, pp. 207-20, Aug 2015.

[72] E. Vilar-Gomez and N. Chalasani, "Non-invasive assessment of non-alcoholic fatty liver disease: Clinical prediction rules and blood-based biomarkers," (in eng), *J Hepatol,* vol. 68, no. 2, pp. 305-315, Feb 2018.

[73] K. Patel and G. Sebastiani, "Limitations of non-invasive tests for assessment of liver fibrosis," *JHEP Reports,* vol. 2, no. 2, 2020.

[74] W. N. Hannah, Jr. and S. A. Harrison, "Nonalcoholic fatty liver disease and elastography: Incremental advances but work still to be done," (in eng), *Hepatology,* vol. 63, no. 6, pp. 1762-4, Jun 2016.

[75] A. Larghi, "Which needle and technique should we use for endoscopic ultrasound-guided liver biopsy? A work in progress," (in En), *Referring to Hasan MK et al. p.818–824,* vol. 51, no. 09, pp. 811-812, 2019/08/28 2019.

[76] A. A. Bravo, S. G. Sheth, and S. Chopra, "Liver biopsy," (in eng), *N Engl J Med,* vol. 344, no. 7, pp. 495-500, Feb 15 2001.

[77] Z. M. Younossi *et al.*, "Diagnostic modalities for nonalcoholic fatty liver disease, nonalcoholic steatohepatitis, and associated fibrosis," (in eng), *Hepatology,* vol. 68, no. 1, pp. 349-360, Jul 2018.

[78] A. Hamon, C. Piquet-Pellorce, M. T. Dimanche-Boitrel, M. Samson, and J. Le Seyec, "Intrahepatocytic necroptosis is dispensable for hepatocyte death in murine immune-mediated hepatitis," (in eng), *J Hepatol,* vol. 73, no. 3, pp. 699-701, Sep 2020.

[79] T. Hennedige and S. K. Venkatesh, "Imaging of hepatocellular carcinoma: diagnosis, staging and treatment monitoring," (in eng), *Cancer Imaging,* vol. 12, no. 3, pp. 530-47, Feb 8 2013.

[80] A. M. Allen, H. K. Van Houten, L. R. Sangaralingham, J. A. Talwalkar, and R. G. McCoy, "Healthcare cost and utilization in nonalcoholic fatty liver disease: real-world data from a large U.S. claims database," (in eng), *Hepatology,* vol. 68, no. 6, pp. 2230-2238, Dec 2018.

[81] M. Noureddin *et al.*, "Utility of magnetic resonance imaging versus histology for quantifying changes in liver fat in nonalcoholic fatty liver disease trials," (in eng), *Hepatology,* vol. 58, no. 6, pp. 1930-40, Dec 2013.

[82] S. K. Venkatesh, M. Yin, and R. L. Ehman, "Magnetic resonance elastography of liver: technique, analysis, and clinical applications," (in eng), *J Magn Reson Imaging,* vol. 37, no. 3, pp. 544-55, Mar 2013.

[83] J.-R. Chen *et al.*, "Clinical Value of Information Entropy Compared with Deep Learning for Ultrasound Grading of Hepatic Steatosis," *Entropy,* vol. 22, no. 9, p. 1006, 2020.

[84] C. C. Park *et al.*, "Magnetic Resonance Elastography vs Transient Elastography in Detection of Fibrosis and Noninvasive Measurement of Steatosis in Patients With Biopsy-Proven Nonalcoholic Fatty Liver Disease," *Gastroenterology,* vol. 152, no. 3, pp. 598-607.e2, 2017.

[85] S. Jayakumar *et al.*, "Longitudinal correlations between MRE, MRI-PDFF, and liver histology in patients with non-alcoholic steatohepatitis: Analysis of data from a phase II trial of selonsertib," *Journal of Hepatology,* vol. 70, no. 1, pp. 133-141, 2019.

[86] S. B. Reeder, I. Cruite, G. Hamilton, and C. B. Sirlin, "Quantitative assessment of liver fat with magnetic resonance imaging and spectroscopy," (in eng), *J Magn Reson Imaging,* vol. 34, no. 4, pp. 729-749, Oct 2011.

[87] S. B. Reeder, H. H. Hu, and C. B. Sirlin, "Proton density fat-fraction: a standardized MR-based biomarker of tissue fat concentration," (in eng), *J Magn Reson Imaging,* vol. 36, no. 5, pp. 1011-4, Nov 2012.

[88] S. H. Kang *et al.*, "KASL clinical practice guidelines: Management of nonalcoholic fatty liver disease," *Clin Mol Hepatol,* vol. 27, no. 3, pp. 363-401, 7 2021.

[89] L. Sandrin *et al.*, "Transient elastography: a new noninvasive method for assessment of hepatic fibrosis," (in eng), *Ultrasound Med Biol,* vol. 29, no. 12, pp. 1705-13, Dec 2003.

[90] M. Hidaka *et al.*, "Living donor liver transplantation from a donor previously treated with interferon for hepatitis C virus: a case report," (in eng), *J Med Case Rep,* vol. 5, p. 276, Jul 3 2011.

[91] F. Shen *et al.*, "Impact of skin capsular distance on the performance of controlled attenuation parameter in patients with chronic liver disease," *Liver international,* vol. 35, no. 11, pp. 2392-2400, 2015.

[92] M. Sasso, V. Miette, L. Sandrin, and M. Beaugrand, "The controlled attenuation parameter (CAP): a novel tool for the non-invasive evaluation of steatosis using Fibroscan®," *Clinics*

and Research in Hepatology and Gastroenterology, vol. 36, no. 1, pp. 13-20, 2012/02/01/ 2012.

[93] J. H. Yu and J. I. Lee, "Current role of transient elastography in the management of chronic hepatitis B patients," *Ultrasonography,* vol. 36, no. 2, pp. 86-94, 4 2017.

[94] M. Friedrich-Rust *et al.*, "Performance of acoustic radiation force impulse imaging for the staging of liver fibrosis: a pooled meta-analysis," *Journal of viral hepatitis,* vol. 19, no. 2, pp. e212-e219, 2012.

[95] S. Kapur *et al.*, "Comparison of elastography point quantification with transient elastography in patients with chronic viral hepatitis and nonalcoholic fatty liver disease: a pilot study," (in eng), *J Clin Exp Hepatol,* vol. 11, no. 1, pp. 21-29, Jan-Feb 2021.

[96] C. Felicani *et al.*, "Point quantification elastography in the evaluation of liver elasticity in healthy volunteers: a reliability study based on operator expertise," (in eng), *J Ultrasound,* vol. 21, no. 2, pp. 89-98, Jun 2018.

[97] F. Conti *et al.*, "Assessment of liver fibrosis with elastography point quantification vs other noninvasive methods," *Clinical Gastroenterology and Hepatology,* vol. 17, no. 3, pp. 510-517.e3, 2019/02/01/ 2019.

[98] G. Ferraioli *et al.*, "Liver ultrasound elastography: an update to the world federation for ultrasound in medicine and biology guidelines and recommendations," (in eng), *Ultrasound Med Biol,* vol. 44, no. 12, pp. 2419-2440, Dec 2018.

[99] K. Nightingale, S. McAleavey, and G. Trahey, "Shear-wave generation using acoustic radiation force: in vivo and ex vivo results," (in eng), *Ultrasound Med Biol,* vol. 29, no. 12, pp. 1715-23, Dec 2003.

[100] J. Bercoff, M. Tanter, and M. Fink, "Supersonic shear imaging: a new technique for soft tissue elasticity mapping," (in eng), *IEEE Trans Ultrason Ferroelectr Freq Control,* vol. 51, no. 4, pp. 396-409, Apr 2004.

[101] M. Muller, J. L. Gennisson, T. Deffieux, M. Tanter, and M. Fink, "Quantitative viscoelasticity mapping of human liver using supersonic shear imaging: preliminary in vivo feasibility study," (in eng), *Ultrasound Med Biol,* vol. 35, no. 2, pp. 219-29, Feb 2009.

[102] R. Chimoriya, M. K. Piya, D. Simmons, G. Ahlenstiel, and V. Ho, "The Use of Two-Dimensional Shear Wave Elastography in People with Obesity for the Assessment of Liver

Fibrosis in Non-Alcoholic Fatty Liver Disease," *Journal of Clinical Medicine*, vol. 10, no. 1. doi: 10.3390/jcm10010095

[103] G. Ferraioli, C. Tinelli, B. Dal Bello, M. Zicchetti, G. Filice, and C. Filice, "Accuracy of real-time shear wave elastography for assessing liver fibrosis in chronic hepatitis C: a pilot study," (in eng), *Hepatology,* vol. 56, no. 6, pp. 2125-33, Dec 2012.

[104] R. Sirli *et al.*, "Liver stiffness measurements by means of supersonic shear imaging in patients without known liver pathology," (in eng), *Ultrasound Med Biol,* vol. 39, no. 8, pp. 1362-7, Aug 2013.

[105] J. H. Yoon *et al.*, "Hepatic fibrosis: prospective comparison of MR elastography and US shear-wave elastography for evaluation," (in eng), *Radiology,* vol. 273, no. 3, pp. 772-82, Dec 2014.

[106] A. P. Sarvazyan, O. V. Rudenko, S. D. Swanson, J. B. Fowlkes, and S. Y. Emelianov, "Shear wave elasticity imaging: a new ultrasonic technology of medical diagnostics," (in eng), *Ultrasound Med Biol,* vol. 24, no. 9, pp. 1419-35, Nov 1998.

[107] M. M. Doyley, "Model-based elastography: a survey of approaches to the inverse elasticity problem," (in eng), *Phys Med Biol,* vol. 57, no. 3, pp. R35-73, Feb 7 2012.

[108] K. J. Parker, M. M. Doyley, and D. J. Rubens, "Imaging the elastic properties of tissue: the 20 year perspective," (in eng), *Phys Med Biol,* vol. 56, no. 1, pp. R1-r29, Jan 7 2011.

[109] T. Shiina *et al.*, "WFUMB guidelines and recommendations for clinical use of ultrasound elastography: Part 1: basic principles and terminology," (in eng), *Ultrasound Med Biol,* vol. 41, no. 5, pp. 1126-47, May 2015.

[110] M. Fatemi and J. F. Greenleaf, "Ultrasound-stimulated vibro-acoustic spectrography," (in eng), *Science,* vol. 280, no. 5360, pp. 82-5, Apr 3 1998.

[111] S. A. McAleavey, M. Menon, and J. Orszulak, "Shear-modulus estimation by application of spatially-modulated impulsive acoustic radiation force," (in eng), *Ultrason Imaging,* vol. 29, no. 2, pp. 87-104, Apr 2007.

[112] E. C. Elegbe and S. A. McAleavey, "Single tracking location methods suppress speckle noise in shear wave velocity estimation," (in eng), *Ultrason Imaging,* vol. 35, no. 2, pp. 109-25, Apr 2013.

[113] P. Song, H. Zhao, A. Manduca, M. W. Urban, J. F. Greenleaf, and S. Chen, "Comb-push ultrasound shear elastography (CUSE): a novel method for two-dimensional shear elasticity

imaging of soft tissues," (in eng), *IEEE Trans Med Imaging,* vol. 31, no. 9, pp. 1821-32, Sep 2012.

[114] P. Song, M. W. Urban, A. Manduca, H. Zhao, J. F. Greenleaf, and S. Chen, "Comb-push ultrasound shear elastography (CUSE) with various ultrasound push beams," (in eng), *IEEE Trans Med Imaging,* vol. 32, no. 8, pp. 1435-47, Aug 2013.

[115] D. Cosgrove *et al.*, "EFSUMB guidelines and recommendations on the clinical use of ultrasound elastography. Part 2: Clinical applications," (in eng), *Ultraschall Med,* vol. 34, no. 3, pp. 238-53, Jun 2013.

[116] J. Bamber *et al.*, "EFSUMB guidelines and recommendations on the clinical use of ultrasound elastography. Part 1: Basic principles and technology," (in eng), *Ultraschall Med,* vol. 34, no. 2, pp. 169-84, Apr 2013.

[117] D. Cosgrove *et al.*, "WFUMB guidelines and recommendations on the clinical use of ultrasound elastography: Part 4. Thyroid," (in eng), *Ultrasound Med Biol,* vol. 43, no. 1, pp. 4-26, Jan 2017.

[118] R. G. Barr *et al.*, "WFUMB guidelines and recommendations on the clinical use of ultrasound elastography: Part 5. Prostate," (in eng), *Ultrasound Med Biol,* vol. 43, no. 1, pp. 27-48, Jan 2017.

[119] G. Ferraioli *et al.*, "WFUMB guidelines and recommendations for clinical use of ultrasound elastography: Part 3: liver," (in eng), *Ultrasound Med Biol,* vol. 41, no. 5, pp. 1161-79, May 2015.

[120] R. G. Barr *et al.*, "WFUMB guidelines and recommendations for clinical use of ultrasound elastography: Part 2: breast," (in eng), *Ultrasound Med Biol,* vol. 41, no. 5, pp. 1148-60, May 2015.

[121] S. Chen *et al.*, "Assessment of liver viscoelasticity by using shear waves induced by ultrasound radiation force," (in eng), *Radiology,* vol. 266, no. 3, pp. 964-70, Mar 2013.

[122] T. Deffieux *et al.*, "Investigating liver stiffness and viscosity for fibrosis, steatosis and activity staging using shear wave elastography," (in eng), *J Hepatol,* vol. 62, no. 2, pp. 317-24, Feb 2015.

[123] K. R. Nightingale *et al.*, "Derivation and analysis of viscoelastic properties in human liver: impact of frequency on fibrosis and steatosis staging," (in eng), *IEEE Trans Ultrason Ferroelectr Freq Control,* vol. 62, no. 1, pp. 165-75, Jan 2015.

[124] Y. Deng, N. C. Rouze, M. L. Palmeri, and K. R. Nightingale, "Ultrasonic shear wave elasticity imaging sequencing and data processing using a verasonics research scanner," (in eng), *IEEE Trans Ultrason Ferroelectr Freq Control,* vol. 64, no. 1, pp. 164-176, Jan 2017.

[125] J. Bercoff, M. Pernot, M. Tanter, and M. Fink, "Monitoring thermally-induced lesions with supersonic shear imaging," *Ultrasonic imaging,* vol. 26, no. 2, pp. 71-84, 2004.

[126] A. M. Osman, A. El Shimy, and M. M. Abd El Aziz, "2D shear wave elastography (SWE) performance versus vibration-controlled transient elastography (VCTE/fibroscan) in the assessment of liver stiffness in chronic hepatitis," (in eng), *Insights Imaging,* vol. 11, no. 1, p. 38, Mar 10 2020.

[127] M. Tanter *et al.*, "Quantitative assessment of breast lesion viscoelasticity: initial clinical results using supersonic shear imaging," (in eng), *Ultrasound Med Biol,* vol. 34, no. 9, pp. 1373-86, Sep 2008.

[128] T. Deffieux, J. L. Gennisson, M. Tanter, and M. Fink, "Assessment of the mechanical properties of the musculoskeletal system using 2-D and 3-D very high frame rate ultrasound," (in eng), *IEEE Trans Ultrason Ferroelectr Freq Control,* vol. 55, no. 10, pp. 2177-90, Oct 2008.

[129] H. Han *et al.*, "Role of virtual touch tissue imaging quantification in the assessment of hepatic sinusoidal obstruction syndrome in a rat model," *J Ultrasound Med.,* vol. 38, no. 8, pp. 2039-2046, 2019.

[130] T. Nishio *et al.*, "Prediction of posthepatectomy liver failure based on liver stiffness measurement in patients with hepatocellular carcinoma," (in eng), *Surgery,* vol. 159, no. 2, pp. 399-408, Feb 2016.

[131] A. Nanashima *et al.*, "Usefulness of evaluating hepatic elasticity using artificial acoustic radiation force ultrasonography before hepatectomy," (in eng), *Hepatol Res,* vol. 44, no. 13, pp. 1308-19, Dec 2014.

[132] S. Chen, M. Fatemi, and J. F. Greenleaf, "Quantifying elasticity and viscosity from measurement of shear wave speed dispersion," (in eng), *J Acoust Soc Am,* vol. 115, no. 6, pp. 2781-5, Jun 2004.

[133] M. W. Urban, S. Chen, and M. Fatemi, "A review of shear wave dispersion ultrasound vibrometry (SDUV) and its applications," (in eng), *Curr Med Imaging Rev,* vol. 8, no. 1, pp. 27-36, Feb 1 2012.

[134] Y. Yamakoshi, J. Sato, and T. Sato, "Ultrasonic imaging of internal vibration of soft tissue under forced vibration," (in eng), *IEEE Trans Ultrason Ferroelectr Freq Control,* vol. 37, no. 2, pp. 45-53, 1990.

[135] S. Catheline, F. Wu, and M. Fink, "A solution to diffraction biases in sonoelasticity: the acoustic impulse technique," (in eng), *J Acoust Soc Am,* vol. 105, no. 5, pp. 2941-50, May 1999.

[136] Z. Wu, L. S. Taylor, D. J. Rubens, and K. J. Parker, "Sonoelastographic imaging of interference patterns for estimation of the shear velocity of homogeneous biomaterials," (in eng), *Phys Med Biol,* vol. 49, no. 6, pp. 911-22, Mar 21 2004.

[137] S. Chen *et al.*, "Shearwave dispersion ultrasound vibrometry (SDUV) for measuring tissue elasticity and viscosity," (in eng), *IEEE Trans Ultrason Ferroelectr Freq Control,* vol. 56, no. 1, pp. 55-62, Jan 2009.

[138] H. Tzschätzsch *et al.*, "In vivo time-harmonic multifrequency elastography of the human liver," (in eng), *Phys Med Biol,* vol. 59, no. 7, pp. 1641-54, Apr 7 2014.

[139] H. Tzschätzsch *et al.*, "Two-dimensional time-harmonic elastography of the human liver and spleen," (in eng), *Ultrasound Med Biol,* vol. 42, no. 11, pp. 2562-2571, Nov 2016.

[140] T. V. Moga *et al.*, "Performance of a noninvasive time-harmonic elastography technique for liver fibrosis evaluation using vibration controlled transient elastography as reference method," (in eng), *Diagnostics,* vol. 10, no. 9, Aug 31 2020.

[141] S. Saadeh *et al.*, "The utility of radiological imaging in nonalcoholic fatty liver disease," (in eng), *Gastroenterology,* vol. 123, no. 3, pp. 745-50, Sep 2002.

[142] D. F. Chan *et al.*, "Hepatic steatosis in obese Chinese children," (in eng), *Int J Obes Relat Metab Disord,* vol. 28, no. 10, pp. 1257-63, Oct 2004.

[143] H. B. Holt *et al.*, "Non-esterified fatty acid concentrations are independently associated with hepatic steatosis in obese subjects," (in eng), *Diabetologia,* vol. 49, no. 1, pp. 141-8, Jan 2006.

[144] M. Byra *et al.*, "Liver fat assessment in multiview sonography using transfer learning with convolutional neural networks," (in eng), *J Ultrasound Med,* vol. 41, no. 1, pp. 175-184, Jan 2022.

[145] M. Wu, P. G. Sharma, and J. R. Grajo, "The echogenic liver: steatosis and beyond," (in eng), *Ultrasound Q,* vol. 37, no. 4, pp. 308-314, Sep 21 2020.

[146] J. H. Zhou, J. J. Cai, Z. G. She, and H. L. Li, "Noninvasive evaluation of nonalcoholic fatty liver disease: Current evidence and practice," (in eng), *World J Gastroenterol,* vol. 25, no. 11, pp. 1307-1326, Mar 21 2019.

[147] A. Chauhan, L. R. Sultan, E. E. Furth, L. P. Jones, V. Khungar, and C. M. Sehgal, "Diagnostic accuracy of hepatorenal index in the detection and grading of hepatic steatosis," (in eng), *J Clin Ultrasound,* vol. 44, no. 9, pp. 580-586, Nov 12 2016.

[148] (Ultrasound for the generalist: a guide to point of care imaging). Cambridge: Cambridge University Press, 2021, pp. 1-3.

[149] M. S. Taljanovic *et al.*, "Shear-wave elastography: Basic physics and musculoskeletal applications," *Radiographics,* vol. 37, no. 3, pp. 855-870, 2017.

[150] C. Amador, M. W. Urban, S. Chen, and J. F. Greenleaf, "Loss tangent and complex modulus estimated by acoustic radiation force creep and shear wave dispersion," (in eng), *Phys Med Biol,* vol. 57, no. 5, pp. 1263-82, Mar 7 2012.

[151] M. Orescanin, Y. Wang, and M. Insana, "3-D FDTD simulation of shear waves for evaluation of complex modulus imaging," (in eng), *IEEE Trans Ultrason Ferroelectr Freq Control,* vol. 58, no. 2, pp. 389-98, Feb 2011.

[152] M. Orescanin, M. A. Qayyum, K. S. Toohey, and M. F. Insana, "Dispersion and shear modulus measurements of porcine liver," (in eng), *Ultrason Imaging,* vol. 32, no. 4, pp. 255-66, Oct 2010.

[153] K. J. Parker, A. Partin, and D. J. Rubens, "What do we know aout shear wave dispersion in normal and steatotic livers?," *Ultrasound in Medicine and Biology,* vol. 41, no. 5, pp. 1481-1487, 2015/05/01/ 2015.

[154] A. H. Henni, C. Schmitt, and G. Cloutier, "Shear wave induced resonance elastography of soft heterogeneous media," (in eng), *J Biomech,* vol. 43, no. 8, pp. 1488-93, May 28 2010.

[155] E. Montagnon, A. Hadj-Henni, C. Schmitt, and G. Cloutier, "Rheological assessment of a polymeric spherical structure using a three-dimensional shear wave scattering model in dynamic spectroscopy elastography," (in eng), *IEEE Trans Ultrason Ferroelectr Freq Control,* vol. 61, no. 2, pp. 277-87, Feb 2014.

[156] M. Bhatt, E. Montagnon, F. Destrempes, B. Chayer, S. Kazemirad, and G. Cloutier, "Acoustic radiation force induced resonance elastography of coagulating blood: theoretical

viscoelasticity modeling and ex vivo experimentation," *Physics in Medicine & Biology,* vol. 63, no. 6, p. 065018, 2018/03/21 2018.

[157] S. Bernard and G. Cloutier, "Forward and inverse viscoelastic wave scattering by irregular inclusions for shear wave elastography," (in eng), *J Acoust Soc Am,* vol. 142, no. 4, p. 2346, Oct 2017.

[158] S. Kazemirad, S. Bernard, S. Hybois, A. Tang, and G. Cloutier, "Ultrasound shear wave viscoelastography: Model-independent quantification of the complex shear modulus," (in eng), *IEEE Trans Ultrason Ferroelectr Freq Control,* vol. 63, no. 9, pp. 1399-1408, Sep 2016.

[159] E. Budelli *et al.*, "A diffraction correction for storage and loss moduli imaging using radiation force based elastography," (in eng), *Phys Med Biol,* vol. 62, no. 1, pp. 91-106, Jan 7 2017.

[160] I. Z. Nenadic *et al.*, "Application of attenuation measuring ultrasound shearwave elastography in 8 post-transplant liver patients," in *2014 IEEE International Ultrasonics Symposium*, 2014, pp. 987-990.

[161] N. C. Rouze, M. L. Palmeri, and K. R. Nightingale, "An analytic, Fourier domain description of shear wave propagation in a viscoelastic medium using asymmetric Gaussian sources," (in eng), *J Acoust Soc Am,* vol. 138, no. 2, pp. 1012-22, Aug 2015.

[162] J. D. Achenbach, *Wave Propagation in Elastic Solids*. North-Holland Publishing Company, Amsterdam, 1973.

[163] T. Deffieux, G. Montaldo, M. Tanter, and M. Fink, "Shear wave spectroscopy for in vivo quantification of human soft tissues visco-elasticity," (in eng), *IEEE Trans Med Imaging,* vol. 28, no. 3, pp. 313-22, Mar 2009.

[164] L. Yazdani, M. Bhatt, I. Rafati, A. Tang, and G. Cloutier, "The revisited frequency-shift method for shear wave attenuation computation and imaging," *IEEE Transactions on Ultrasonics, Ferroelectrics, and Frequency Control,* vol. 69, no. 6, pp. 2061-2074, 2022.

[165] M. W. Urban, C. Pislaru, I. Z. Nenadic, R. R. Kinnick, and J. F. Greenleaf, "Measurement of viscoelastic properties of in vivo swine myocardium using lamb wave dispersion ultrasound vibrometry (LDUV)," (in eng), *IEEE Trans Med Imaging,* vol. 32, no. 2, pp. 247-61, Feb 2013.

[166] C. Helfenstein-Didier *et al.*, "In vivo quantification of the shear modulus of the human Achilles tendon during passive loading using shear wave dispersion analysis," (in eng), *Phys Med Biol,* vol. 61, no. 6, pp. 2485-96, Mar 21 2016.

[167] L. Ambrozinski, P. Packo, L. Pieczonka, T. Stepinski, T. Uhl, and W. J. Staszewski, "Identification of material properties – efficient modelling approach based on guided wave propagation and spatial multiple signal classification," *Struct. Control Health Monit.,* vol. 22, no. 7, pp. 969-983, 2015.

[168] K. J. Parker, J. Ormachea, S. Will, and Z. Hah, "Analysis of transient shear wave in lossy media," (in eng), *Ultrasound Med Biol,* vol. 44, no. 7, pp. 1504-1515, Jul 2018.

[169] K. J. Parker, T. Szabo, and S. Holm, "Towards a consensus on rheological models for elastography in soft tissues," (in eng), *Phys Med Biol,* vol. 64, no. 21, p. 215012, Oct 31 2019.

[170] C. T. Barry *et al.*, "Shear wave dispersion in lean versus steatotic rat livers," (in eng), *J Ultrasound Med,* vol. 34, no. 6, pp. 1123-9, Jun 2015.

[171] J. K. Jang *et al.*, "Two-dimensional shear-wave elastography and US attenuation imaging for nonalcoholic steatohepatitis diagnosis: A cross-sectional, multicenter study," *Radiology,* vol. 305, no. 1, pp. 118-126, 2022/10/01 2022.

[172] X.-q. Zhang, R.-q. Zheng, J.-y. Jin, J.-f. Wang, T. Zhang, and J. Zeng, "US shear-wave elastography dispersion for characterization of chronic liver disease," *Radiology,* p. 212609, 2022.

[173] E. H. Clayton, G. M. Genin, and P. V. Bayly, "Transmission, attenuation and reflection of shear waves in the human brain," (in eng), *J R Soc Interface,* vol. 9, no. 76, pp. 2899-910, Nov 7 2012.

[174] J. L. Gennisson, S. Lerouge, and G. Cloutier, "Assessment by transient elastography of the viscoelastic properties of blood during clotting," (in eng), *Ultrasound Med Biol,* vol. 32, no. 10, pp. 1529-37, Oct 2006.

[175] K. J. Parker, J. Ormachea, M. G. Drage, H. Kim, and Z. Hah, "The biomechanics of simple steatosis and steatohepatitis," (in eng), *Phys Med Biol,* vol. 63, no. 10, p. 105013, May 17 2018.

[176] A. K. Sharma *et al.*, "Attenuation of shear waves in normal and steatotic livers," (in eng), *Ultrasound in Medicine and Biology,* vol. 45, no. 4, pp. 895-901, Apr 2019.

[177] J. Ormachea and K. J. Parker, "Comprehensive viscoelastic characterization of tissues and the inter-relationship of shear wave (group and phase) velocity, attenuation and dispersion," *Ultrasound in Medicine & Biology,* vol. 46, no. 12, pp. 3448-3459, 2020/12/01/ 2020.

[178] M. M. Doyley and K. J. Parker, "Elastography: general principles and clinical applications," (in eng), *Ultrasound Clin,* vol. 9, no. 1, pp. 1-11, Jan 2014.

[179] C. T. Barry *et al.*, "Mouse liver dispersion for the diagnosis of early-stage Fatty liver disease: a 70-sample study," (in eng), *Ultrasound Med Biol,* vol. 40, no. 4, pp. 704-13, Apr 2014.

[180] N. C. Rouze, Y. Deng, C. A. Trutna, M. L. Palmeri, and K. R. Nightingale, "Characterization of Viscoelastic Materials Using Group Shear Wave Speeds," (in eng), *IEEE transactions on ultrasonics, ferroelectrics, and frequency control,* vol. 65, no. 5, pp. 780-794, 2018.

[181] C. A. Trutna, N. C. Rouze, M. L. Palmeri, and K. R. Nightingale, "Measurement of viscoelastic material model parameters using fractional derivative group shear wave speeds in simulation and phantom data," (in eng), *IEEE transactions on ultrasonics, ferroelectrics, and frequency control,* vol. 67, no. 2, pp. 286-295, 2020.

[182] J. Ormachea and K. J. Parker, "Reverberant shear wave phase gradients for elastography," *Physics in Medicine & Biology,* vol. 66, no. 17, p. 175001, Aug 2021.

[183] M. Fischler and R. Bolles, "Random sample consensus: a paradigm for model fitting with applications to image analysis and automated cartography," *Commun. ACM,* vol. 24, pp. 381-395, 1981.

[184] M. L. Palmeri *et al.*, "Noninvasive evaluation of hepatic fibrosis using acoustic radiation force-based shear stiffness in patients with nonalcoholic fatty liver disease," (in eng), *J Hepatol,* vol. 55, no. 3, pp. 666-672, Sep 2011.

[185] M. Waine, C. Rossa, R. Sloboda, N. Usmani, and M. Tavakoli, "3D shape visualization of curved needles in tissue from 2D ultrasound images using RANSAC," *2015 IEEE International Conference on Robotics and Automation (ICRA),* pp. 4723-4728, 2015.

[186] J. L. Gennisson and G. Cloutier, "Sol-gel transition in agar-gelatin mixtures studied with transient elastography," (in eng), *IEEE Trans Ultrason Ferroelectr Freq Control,* vol. 53, no. 4, pp. 716-23, Apr 2006.

[187] F. Zvietcovich, N. Baddour, J. P. Rolland, and K. J. Parker, "Shear wave propagation in viscoelastic media: validation of an approximate forward model," (in eng), *Phys Med Biol,* vol. 64, no. 2, p. 025008, Jan 8 2019.

[188] M. Gesnik *et al.*, "In vivo ultrafast quantitative ultrasound and shear wave elastography imaging on farm-raised duck livers during force feeding," (in eng), *Ultrasound Med Biol,* vol. 46, no. 7, pp. 1715-1726, Jul 2020.

[189] D. Garcia, L. Le Tarnec, S. Muth, E. Montagnon, J. Porée, and G. Cloutier, "Stolt's f-k migration for plane wave ultrasound imaging," (in eng), *IEEE Trans Ultrason Ferroelectr Freq Control,* vol. 60, no. 9, pp. 1853-67, Sep 2013.

[190] T. Loupas, R. B. Peterson, and R. W. Gill, "Experimental evaluation of velocity and power estimation for ultrasound blood flow imaging, by means of a two-dimensional autocorrelation approach," *IEEE Transactions on Ultrasonics, Ferroelectrics, and Frequency Control,* vol. 42, no. 4, pp. 689-699, 1995.

[191] T. Deffieux, J. L. Gennisson, J. Bercoff, and M. Tanter, "On the effects of reflected waves in transient shear wave elastography," (in eng), *IEEE Trans Ultrason Ferroelectr Freq Control,* vol. 58, no. 10, pp. 2032-5, Oct 2011.

[192] J. Ophir *et al.*, "Attenuation estimation in reflection: progress and prospects," *Ultrasonic Imaging,* vol. 6, no. 4, pp. 349-395, 1984.

[193] X. Jacob, S. Catheline, J.-L. Gennisson, C. Barrière, D. Royer, and M. Fink, "Nonlinear shear wave interaction in soft solids," *The Journal of the Acoustical Society of America,* vol. 122, no. 4, pp. 1917-1926, 2007.

[194] S. A. Goss, L. A. Frizzell, and F. Dunn, "Ultrasonic absorption and attenuation in mammalian tissues," (in eng), *Ultrasound Med Biol,* vol. 5, no. 2, pp. 181-6, 1979.

[195] P. Kijanka and M. W. Urban, "Local phase velocity based imaging of viscoelastic phantoms and tissues," (in eng), *IEEE Trans Ultrason Ferroelectr Freq Control,* vol. 68, no. 3, pp. 389-405, Mar 2021.

[196] B. R. Chintada, R. Rau, and O. Goksel, "Nonlinear characterization of tissue viscoelasticity with acoustoelastic attenuation of shear waves," (in eng), *IEEE Trans Ultrason Ferroelectr Freq Control,* vol. 69, no. 1, pp. 38-53, Aug 2021.

[197] P. A. Narayana and J. Ophir, "On the frequency dependence of attenuation in normal and fatty liver," *IEEE Transactions on Sonics and Ultrasonics,* vol. 30, no. 6, pp. 379-382, 1983.

[198] N. Baddour, "Multidimensional wave field signal theory: Mathematical foundations," *AIP Advances,* vol. 1, no. 2, p. 022120, June 2011.

[199] M. Abramowitz and I. Stegun, *Handbook of mathematical functions with formulas, graphs, and mathematical tables.* Washington,:U.S.: Govt. Print. Off.; 1964.

[200] F. B. Palabiyik, E. Inci, R. Turkay, and D. Bas, "Evaluation of liver, kidney, and spleen elasticity in healthy newborns and infants using shear wave elastography," *Journal of ultrasound in medicine,* vol. 36, no. 10, pp. 2039-2045, 2017.

[201] L. A. Gilligan, A. T. Trout, P. Bennett, and J. R. Dillman, "Repeatability and agreement of shear wave speed measurements in phantoms and human livers across 6 ultrasound 2-dimensional shear wave elastography systems," (in eng), *Invest Radiol,* vol. 55, no. 4, pp. 191-199, Apr 2020.

[202] M. D. Horeh, A. Asif, and H. Rivaz, "Analytical minimization-based regularized subpixel shear-wave tracking for ultrasound elastography," *IEEE Transactions on Ultrasonics, Ferroelectrics, and Frequency Control,* vol. 66, no. 2, pp. 285-296, 2019.

[203] D. M. Dumont and B. C. Byram, "Robust tracking of small displacements with a bayesian estimator," (in eng), *IEEE Trans Ultrason Ferroelectr Freq Control,* vol. 63, no. 1, pp. 20-34, Jan 2016.

[204] A. Ofosu, D. Ramai, and M. Reddy, "Non-alcoholic fatty liver disease: controlling an emerging epidemic, challenges, and future directions," (in eng), *Annals of Gastroenterology,* vol. 31, no. 3, pp. 288-295, May-Jun 2018.

[205] L. A. Adams and K. D. Lindor, "Nonalcoholic fatty liver disease," (in eng), *Annals of Epidemiology,* vol. 17, no. 11, pp. 863-9, Nov 2007.

[206] J. Z. Zhang, J. J. Cai, Y. Yu, Z. G. She, and H. Li, "Nonalcoholic fatty liver disease: an update on the diagnosis," (in eng), *Gene Expression The Journal of Liver Research,* vol. 19, no. 3, pp. 187-198, Nov 4 2019.

[207] J. K. Gaidos, B. E. Hillner, and A. J. Sanyal, "A decision analysis study of the value of a liver biopsy in nonalcoholic steatohepatitis," (in eng), *Liver International,* vol. 28, no. 5, pp. 650-8, May 2008.

[208] G. Colloredo, M. Guido, A. Sonzogni, and G. Leandro, "Impact of liver biopsy size on histological evaluation of chronic viral hepatitis: the smaller the sample, the milder the disease," (in eng), *Hepatology,* vol. 39, no. 2, pp. 239-44, Aug 2003.

[209] R. P. Myers, A. Fong, and A. A. Shaheen, "Utilization rates, complications and costs of percutaneous liver biopsy: a population-based study including 4275 biopsies," (in eng), *Liver Int,* vol. 28, no. 5, pp. 705-12, May 2008.

[210] M. Noureddin and R. Loomba, "Nonalcoholic fatty liver disease: Indications for liver biopsy and noninvasive biomarkers," (in eng), *Clinical Liver Disease (Hoboken),* vol. 1, no. 4, pp. 104-107, Sep 2012.

[211] Y. Sumida, A. Nakajima, and Y. Itoh, "Limitations of liver biopsy and non-invasive diagnostic tests for the diagnosis of nonalcoholic fatty liver disease/nonalcoholic steatohepatitis," (in eng), *World Journal of Gastroenterology,* vol. 20, no. 2, pp. 475-85, Jan 14 2014.

[212] H. Kramer *et al.*, "Accuracy of liver fat quantification with advanced CT, MRI, and Ultrasound techniques: prospective comparison with MR spectroscopy," (in eng), *AJR. American Journal of Roentgenology,* vol. 208, no. 1, pp. 92-100, Jan 2017.

[213] A. Tang *et al.*, "Nonalcoholic fatty liver disease: MR imaging of liver proton density fat fraction to assess hepatic steatosis," (in eng), *Radiology,* vol. 267, no. 2, pp. 422-31, May 2013.

[214] G. Ferraioli *et al.*, "Quantification of liver fat content with ultrasound: A WFUMB position paper," (in eng), *Ultrasound Med Biol,* vol. 47, no. 10, pp. 2803-2820, Oct 2021.

[215] N. Kalra *et al.*, "Chemical shift magnetic resonance imaging is helpful in detecting hepatic steatosis but not fibrosis in patients with nonalcoholic fatty liver disease (NAFLD)," (in eng), *Annals of Hepatology,* vol. 8, no. 1, pp. 21-5, Jan-Mar 2009.

[216] S. C. Lin *et al.*, "Noninvasive diagnosis of nonalcoholic fatty liver disease and quantification of liver fat using a new quantitative ultrasound technique," (in eng), *Clinical Gastroenterology and Hepatology,* vol. 13, no. 7, pp. 1337-1345.e6, Jul 2015.

[217] R. Smith-Bindman *et al.*, "Radiation dose associated with common computed tomography examinations and the associated lifetime attributable risk of cancer," (in eng), *Arch Intern Med,* vol. 169, no. 22, pp. 2078-86, Dec 14 2009.

[218] S. Strauss, E. Gavish, P. Gottlieb, and L. Katsnelson, "Interobserver and intraobserver variability in the sonographic assessment of fatty liver," *American Journal of Roentgenology,* vol. 189, no. 6, pp. W320-W323, 2007/12/01 2007.

[219] N. Khov, A. Sharma, and T. R. Riley, "Bedside ultrasound in the diagnosis of nonalcoholic fatty liver disease," (in eng), *World J Gastroenterol,* vol. 20, no. 22, pp. 6821-5, Jun 14 2014.

[220] Y. N. Zhang *et al.*, "Liver fat imaging-a clinical overview of ultrasound, CT, and MR imaging," (in eng), *Br J Radiol,* vol. 91, no. 1089, p. 20170959, Sep 2018.

[221] W. J. Zwiebel, "Sonographic diagnosis of diffuse liver disease," (in eng), *Semin Ultrasound CT MR,* vol. 16, no. 1, pp. 8-15, Feb 1995.

[222] D. Garcia, L. L. Tarnec, S. Muth, E. Montagnon, J. Porée, and G. Cloutier, "Stolt's f-k migration for plane wave ultrasound imaging," *IEEE Transactions on Ultrasonics, Ferroelectrics, and Frequency Control,* vol. 60, no. 9, pp. 1853-1867, 2013.

[223] R. Longo *et al.*, "Proton MR spectroscopy in quantitative in vivo determination of fat content in human liver steatosis," (in eng), *J Magn Reson Imaging,* vol. 5, no. 3, pp. 281-5, May-Jun 1995.

[224] A. Tang *et al.*, "MR elastography in nonalcoholic fatty liver disease: inter-center and inter-analysis-method measurement reproducibility and accuracy at 3T," (in eng), *Eur Radiol,* vol. 32, no. 5, pp. 2937-2948, May 2022.

[225] M. M. Mukaka, "Statistics corner: A guide to appropriate use of correlation coefficient in medical research," (in eng), *Malawi Med J,* vol. 24, no. 3, pp. 69-71, Sep 2012.

[226] W. J. Youden, "Index for rating diagnostic tests," (in eng), *Cancer,* vol. 3, no. 1, pp. 32-5, Jan 1950.

[227] E. R. DeLong, D. M. DeLong, and D. L. Clarke-Pearson, "Comparing the areas under two or more correlated receiver operating characteristic curves: a nonparametric approach," (in eng), *Biometrics,* vol. 44, no. 3, pp. 837-45, Sep 1988.

[228] Q. Qi *et al.*, "Magnetic resonance imaging-derived proton density fat fraction (MRI-PDFF) is a viable alternative to liver biopsy for steatosis quantification in living liver donor transplantation," (in eng), *Clin Transplant,* vol. 35, no. 7, p. e14339, Jul 2021.

[229] G. Ligabue, G. Besutti, R. Scaglioni, C. Stentarelli, and G. Guaraldi, "MR quantitative biomarkers of non-alcoholic fatty liver disease: technical evolutions and future trends," (in eng), *Quant Imaging Med Surg,* vol. 3, no. 4, pp. 192-5, Aug 2013.

[230] G. Ferraioli *et al.*, "Detection of liver steatosis with a novel ultrasound-based technique: A pilot study using MRI-derived proton density fat fraction as the gold standard," *Clinical and Translational Gastroenterology,* vol. 10, no. 10, 2019.

[231] K. A. Wear *et al.*, "US Backscatter for liver fat quantification: an AIUM-RSNA QIBA Pulse-Echo quantitative ultrasound initiative," *Radiology,* vol. 305, no. 3, pp. 526-537, 2022/12/01 2022.

[232] Y. Labyed and A. Milkowski, "Novel method for ultrasound-derived fat fraction using an integrated phantom," *Journal of Ultrasound in Medicine,* https://doi.org/10.1002/jum.15364 vol. 39, no. 12, pp. 2427-2438, 2020/12/01 2020.

[233] I. Rafati, F. Destrempes, L. Yazdani, M. Gesnik, A. Tang, and G. Cloutier, "Regularized ultrasound phantom-free local attenuation coefficient slope (ACS) imaging in homogeneous and heterogeneous tissues," *IEEE Transactions on Ultrasonics, Ferroelectrics, and Frequency Control,* vol. 69, no. 12, pp. 3338-3352, 2022.

[234] B. A. Herman and G. R. Harris, "Models and regulatory considerations for transient temperature rise during diagnostic ultrasound pulses," (in eng), *Ultrasound Med Biol,* vol. 28, no. 9, pp. 1217-24, Sep 2002.

[235] M. L. Palmeri, K. D. Frinkley, and K. R. Nightingale, "Experimental studies of the thermal effects associated with radiation force imaging of soft tissue," (in eng), *Ultrason Imaging,* vol. 26, no. 2, pp. 100-14, Apr 2004.

[236] F. a. D. Administration, "Information for manufacturers seeking marketing clearance of diagnostic ultrasound systems and transducers.," 2008.

[237] F. a. D. Administration, "Marketing clearance of diagnostic ultrasound systems and transducers: Guidance for industry and food and drug administration staff.," Silver Spring, MD : Center for Devices and Radiological Health2019.

[238] G. t. Haar, Ed. *The Safe Use of Ultrasound in Medical Diagnosis, 3rd ed* (no. 2). 2013, pp. 345-346.

[239] D. L. Miller *et al.*, "Diagnostic ultrasound safety review for point-of-care ultrasound practitioners," (in eng), *J Ultrasound Med,* vol. 39, no. 6, pp. 1069-1084, Jun 2020.

[240] C. C. Church, C. Labuda, and K. Nightingale, "A theoretical study of inertial cavitation from acoustic radiation force impulse imaging and implications for the mechanical index," (in eng), *Ultrasound Med Biol,* vol. 41, no. 2, pp. 472-85, Feb 2015.

[241] T. A. Bigelow *et al.*, "The thermal index: its strengths, weaknesses, and proposed improvements," (in eng), *J Ultrasound Med,* vol. 30, no. 5, pp. 714-34, May 2011.

[242] M. C. Ziskin, "The thermal dose index," (in eng), *J Ultrasound Med,* vol. 29, no. 10, pp. 1475-9, Oct 2010.

[243] K. J. Parker, A. Partin, and D. J. Rubens, "What do we know about shear wave dispersion in normal and steatotic livers?," (in eng), *Ultrasound Med Biol,* vol. 41, no. 5, pp. 1481-7, May 2015.

[244] Z. M. Younossi, A. B. Koenig, D. Abdelatif, Y. Fazel, L. Henry, and M. Wymer, "Global epidemiology of nonalcoholic fatty liver disease-Meta-analytic assessment of prevalence, incidence, and outcomes," (in eng), *Hepatology,* vol. 64, no. 1, pp. 73-84, Jul 2016.

[245] M. M. Ruissen, A. L. Mak, U. Beuers, M. E. Tushuizen, and A. G. Holleboom, "Non-alcoholic fatty liver disease: a multidisciplinary approach towards a cardiometabolic liver disease," (in eng), *Eur J Endocrinol,* vol. 183, no. 3, pp. R57-r73, Sep 2020.

[246] T. Deffieux *et al.*, "Investigating liver stiffness and viscosity for fibrosis, steatosis and activity staging using shear wave elastography," *Journal of Hepatology,* vol. 62, no. 2, pp. 317-324, 2015/02/01/ 2015.

[247] R. R. Bouchard, S. J. Hsu, P. D. Wolf, and G. E. Trahey, "In vivo cardiac, acoustic-radiation-force-driven, shear wave velocimetry," (in eng), *Ultrason Imaging,* vol. 31, no. 3, pp. 201-13, Jul 2009.

[248] D. L. Raunig *et al.*, "Quantitative imaging biomarkers: a review of statistical methods for technical performance assessment," (in eng), *Stat Methods Med Res,* vol. 24, no. 1, pp. 27-67, Feb 2015.

[249] J. Eiler *et al.*, "Standard value of ultrasound elastography using acoustic radiation force impulse imaging (ARFI) in healthy liver tissue of children and adolescents," (in eng), *Ultraschall Med,* vol. 33, no. 5, pp. 474-9, Oct 2012.

[250] A. T. Trout, S. A. Xanthakos, P. S. Bennett, and J. R. Dillman, "Liver shear wave speed and other quantitative ultrasound measures of liver parenchyma: prospective evaluation in

healthy children and adults," (in eng), *AJR Am J Roentgenol,* vol. 214, no. 3, pp. 557-565, Mar 2020.

[251] C. Cassinotto *et al.*, "Liver stiffness in nonalcoholic fatty liver disease: A comparison of supersonic shear imaging, FibroScan, and ARFI with liver biopsy," (in eng), *Hepatology,* vol. 63, no. 6, pp. 1817-27, Jun 2016.

[252] G. E. Leclerc *et al.*, "Analysis of liver viscosity behavior as a function of multifrequency magnetic resonance elastography (MMRE) postprocessing," (in eng), *J Magn Reson Imaging,* vol. 38, no. 2, pp. 422-8, Aug 2013.

Appendix: List of publications

Journal publications

1. Manish Bhatt, **Ladan Yazdani**, François Destrempes, Louise Allard, Bich Nguyen, An Tang, Guy Cloutier, "Multiparametric in vivo ultrasound shear wave viscoelastography on farm-raised fatty duck livers: Human radiology imaging applied to food sciences," *Poultry Science.* vol. 100, no. 4, p. 100968, 2021.

2. Hongliang Li, Guillaume Flé, Manish Bhatt, Zhen Qu, Sajad Ghazavi, **Ladan Yazdani**, Guillaume Bosio, Iman Rafati, Guy Cloutier, "Viscoelasticity Imaging of Biological Tissues and Single Cells Using Shear Wave Propagation," *Frontiers in Physics.* vol. 9, p. 350, 2021.

3. **Ladan Yazdani**, Manish Bhatt, Iman Rafati, An Tang, Guy Cloutier, "The Revisited Frequency-Shift Method for Shear Wave Attenuation Computation and Imaging," *IEEE transactions on ultrasonics, ferroelectrics, and frequency control.* vol. 69, no.6, p. 2061-2074, 2022.

4. Iman Rafati, François Destrempes, **Ladan Yazdani**, Marc Gesnik, An Tang, Guy Cloutier, "Regularized Ultrasound Phantom-Free Local Attenuation Coefficient Slope (ACS) Imaging in Homogeneous and Heterogeneous Tissues," *IEEE transactions on ultrasonics, ferroelectrics, and frequency control.* vol. 69, no. 12, p. 3338-3352, 2022.

5. **Ladan Yazdani**, Iman Rafati, Marc Gesnik, Frank Nicolet, Boris Chayer, Guillaume Gilbert, Anton Volniansky, Damien Olivié, Jeanne-Marie Giard, Giada Sebastiani, Bich N. Nguyen, An Tang, and Guy Cloutier, "Ultrasound shear wave attenuation imaging for grading liver steatosis in volunteers and patients with nonalcoholic fatty liver disease: a pilot study," *Ultrasound in medicine and biology*, in press, June 2023.

6. **Ladan Yazdani**, Sathiyamoorthy Selladurai, Iman Rafati, Manish Bhatt, Damien Olivié, Jeanne-Marie Giard, Giada Sebastiani, Bich N. Nguyen, Guy Cloutier, and An Tang, "Between-visit reproducibility of shear wave viscoelastography in volunteers and patients with nonalcoholic fatty liver disease," *In preparation.*

7. Guillaume Bosio, François Destrempes, **Ladan Yazdani**, Marie-Helene Roy Cardinal, Guy Cloutier, “Resonance and attenuation of shear wave propagation in blood clot *in vitro* models,” *Submitted*.

List of peer reviewed conference proceeding

1. **Ladan Yazdani**, Manish Bhatt, Guillaume Bosio, Guy Cloutier, “Improved frequency-shift method for shear wave attenuation computation,” IEEE International Ultrasonics Symposium (IUS), 2020.

List of presentations

1. **Ladan Yazdani**, Manish Bhatt, Iman Rafati, An Tang, Guy Cloutier, "Shear wave *in vivo* attenuation measurement with an improved frequency shift method: duck liver experiements,” IEEE IUS, Venice, Italy, 2022.
2. Sathiyamoorthy Selladurai, **Ladan Yazdani**, et al., "Multiparametric *in vivo* shear wave viscoelastography for liver cancer assessment: Preliminary Results," IEEE IUS, Venice, Italy, 2022.
3. Sathiyamoorthy Selladurai, **Ladan Yazdani**, et al., "Between-visit reproducibility of shear wave viscoelastography for diffuse liver disease," IEEE IUS, Venice, Italy, 2022.
4. Iman Rafati, François Destrempes, **Ladan Yazdani**, Tang A, Cloutier G, "Quantitative ultrasound imaging using regularized phantom-free reconstruction of local attenuation coefficient slopes in hetereogenous tissues: *in vitro* validation and *in vivo* feasibility in human fatty lover and liver cancer,” IEEE IUS, Venice, Italy, 2022.
5. **Ladan Yazdani**, Iman Rafati, Marc Gesnik, Frank Nicolet, Boris Chayer, Guillaume Gilbert, Anton Volniansky, Damien Olivié, Jeanne-Marie Giard, Giada Sebastiani, Bich N. Nguyen, An Tang, and Guy Cloutier, "Ultrasound shear wave attenuation measurement in nonalcoholic fatty liver disease: a pilot study,” University Day of the Department of Radiology, Radiation Oncology and Nuclear Medicine, University of Montreal (JU Radiol-UdeM), 2023.
6. Iman Rafati, François Destrempes, **Ladan Yazdani**, Marc Gesnik, An Tang, Guy Cloutier, "Quantitative ultrasound imaging using regularized phantom-free construction of local attenuation coefficient slope maps," JU Radiol-UdeM, 2023.

7. **Ladan Yazdani**, Iman Rafati, Marc Gesnik, Frank Nicolet, Boris Chayer, Guillaume Gilbert, Anton Volniansky, Damien Olivié, Jeanne-Marie Giard, Giada Sebastiani, Bich N. Nguyen, An Tang, and Guy Cloutier, "Ultrasound Shear Wave Attenuation Measurement in Nonalcoholic Fatty Liver Disease: a Pilot Study," SQLNM-CMDO scientific meeting, Magog, Canada, 2023.
8. **Ladan Yazdani**, et al., "Liver fat evaluation in force-fed ducks using shear wave attenuation coefficient," JU Radiol-UdeM, 2022.
9. Iman Rafati, François Destrempes, **Ladan Yazdani**, Tang A, Cloutier G, "Noninvasive diagnosis of lesions in homogenous media using a regularized phantom-free construction of local attenuation coefficient slope maps," JU Radiol-UdeM, 2022.
10. Sathiyamoorthy Selladurai, Manish Bhatt, **Ladan Yazdani**, et al., "Multiparametric in vivo quantitative ultrasound shear wave viscoelastography for liver cancer assessments: Preliminary results" JU Radiol-UdeM, 2022.
11. Manish Bhatt, **Ladan Yazdani**, François Destrempes, Louise Allard, Bich Nguyen, An Tang, Guy Cloutier, "Shear wave viscoelastography on fatty mulard duck livers in vivo" IEEE IUS, Las Vegas, United States, 2020.